



Review

Advances in catalytic/photocatalytic bacterial inactivation by nano Ag and Cu coated surfaces and medical devices

Sami Rtimi^{a,*}, Dionysios D. Dionysiou^b, Suresh C. Pillai^{c,d}, John Kiwi^a^a Ecole Polytechnique Fédérale de Lausanne, EPFL-SB-ISIC-GPAO, Station 6, CH-1015, Lausanne, Switzerland^b Environmental Engineering and Science Program, Department of Chemical and Environmental Engineering (DChEE), 705 Engineering Research Center, University of Cincinnati, Cincinnati, OH 45221-0012, USA^c Nanotechnology and Bio-Engineering Research Division, Department of Environmental Science, School of Science, Institute of Technology Sligo, Ash Lane, Sligo, Ireland^d Centre for Precision Engineering, Materials, and Manufacturing Research (PEM), Institute of Technology Sligo, Sligo, Ireland

ARTICLE INFO

Keywords:

Catalytic/Photocatalytic surfaces
Metal oxides
Antibacterial surfaces
Medical devices
Silver and copper
Titanium dioxide (TiO₂)

ABSTRACT

The design, synthesis, fundamentals and evaluation of 2D/3D antimicrobial surfaces are addressed in detail in the current review. Recent advances in the antimicrobial mechanism, kinetics and properties of Ag, Cu and Ag-Cu surfaces in the dark and under light irradiation are described and discussed. The structure-reactivity relations in the catalyst/photocatalyst layers were described by way of the surface characterization and the observed antibacterial kinetics. *Escherichia coli* (*E. coli*) and *Methicillin resistant Staphylococcus aureus* *MRSA* bacteria are selected as model pathogens to evaluate the antimicrobial inactivation kinetics. The separate antimicrobial properties of ions and the antimicrobial surface-contact effects are presented in a detailed way. The interfacial charge transfer (IFCT) mechanism and the identification of the most relevant reactive oxygen species (ROS) leading to bacterial disinfection are considered. The recently developed monitoring of the changes of the film surface potential (Eigenvalues) during bacterial inactivation and the redox reactions associated with catalyst/photocatalyst surfaces are also presented. The potential for practical applications of these innovative 2D films and 3D sputtered medical devices in health-care facilities are accounted for in the present review.

Part 1: Ag based materials as antibacterial agents

1. Introduction

1.1. Ag as antimicrobial particles

Since decades, nano-silver has been used as an antibacterial material. Ag-nanoparticles cannot be compared to conventional chemicals or bulk materials when trying to elucidate its bactericide action. Products containing nano-silver particles have been commercially available for over 100 years and have been used in different applications [1]. The medical uses of Ag-suspensions, Ag-healing pads and Ag-ions have been reported for the last few decades. Lately, there has been a renewed interest in silver coatings for antimicrobial purposes due to the increased resistance of bacteria to antibiotics [2]. The bacterial inactivation by Ag proceeds by the release of silver-ions penetrating the bacteria cytoplasm through the bacterial porins and by the silver nanoparticles in contact with the bacterial outer-wall [2]. Also, silver nanoparticles (Ag-NPs) have been reported to inactivate bacteria and

other pathogens through the oligodynamic effect involving the diffusion of 10⁻⁶-10⁻⁹ mol/l (ppm-ppb) amounts in contact with the bacterial outer cell envelope [2–6]. Ag-NPs disinfection proceeds in suspension or deposited on films through the destruction of cell wall by reactive oxygen species (ROS) [1–9]. The Ag-toxicity towards bacteria, viruses and fungi is significantly higher compared to the toxicity reported for mammalian cells [4,5].

Silver ions have an affinity towards sulphhydryl groups located at the cell wall, interfering with the electron transport chain through the cell wall porins diffusing to the interior of the bacteria. Ag-ions have also been reported to block the respiratory chain of microorganisms without inducing resistance to silver ions with a few exceptions [7]. The concentrations required for bactericidal activity are in the ppb range (10⁻⁹ mol/l). Metallic silver particles react with moisture, releasing highly oxidative Ag-ions. These Ag-ions complex with DNA and RNA, which inhibit the microorganism replication [8]. Recent reviews report that the size, shape and concentration of Ag-NPs control their antimicrobial kinetics and efficiency [9]. Treatment of thermal burns by Ag-NPs to preclude infections during the healing process has been known for over

* Corresponding author.

E-mail address: sami.rtimi@epfl.ch (S. Rtimi).

100 years [10].

The ability of Ag-NPs and Cu-NPs associated ions to destroy biofilms is based on their ability to penetrate the biofilm due to their small size. The hindrance to the biofilm formation due to the fast bacterial inactivation kinetics of metal Ag-NPs is an important focus of current research. In contrast to traditional antibiotics, M-NPs have small dimensions < 100 nm and present a larger surface area-to-mass ratio [1]. Toxic biofilms spread highly toxic pathogens in healthcare facilities and public places. Biofilms provide protection to bacterial strains by embedding them in a polymeric network structure. This hinders the penetration of most antibiotics. Bacteria biofilms produce extracellular polymeric substances (ESP) when sticking to surfaces that subsequently protect the biofilm. This allows the film matrix to remain stable for a long-time [11]. The hydrophilic-hydrophobic balance between the surface of polymer films and the bacteria envelope has a great influence on the release of Ag-NPs-ions deposited on a polymer network [12].

The current review presents: a) basic principles on the action of Ag and Cu-nanoparticles and b) the *modus operandi* of Ag and Cu-nanoparticles fixed on a substrate. Subsequently, we also address the bacterial inactivation by Ag-Cu films including the film preparation, kinetics evaluation and surface properties in the dark or under light irradiation. Only few bacterial inactivation mechanisms under light have been reported until now and this review presents in detail the recent developments in this area.

1.2. Surface Ag-NPs characteristics

The kinetics and bacterial inactivation mechanism is strongly related to the Ag-size [13], shape [14] and surface charge [15] of the Ag-NPs. This consideration is also valid in the case of Cu-NPs [16]. Factors determining the kinetics/performance of Ag-NPs during bacterial inactivation involve the specific surface area, the surface energy, the nature of the ligands and Ag-NPs aggregation size. The release of Ag-ions in contact with *E. coli* leads to bacterial inactivation and is a function of the of Ag-NPs concentration, pH and surface potential [17]. Ag-NPs have been reported to generate ROS [18,19]. When Ag-NPs contact *E. coli*, the cell wall disruption occurs not only due to effect of the Ag-ions but also due to the Ag-NPs in contact with the bacterial cell wall envelope (surface-contact effect) [20–23]. The speciation of Ag-NPs plays an important role in the bacterial inactivation and is a function of the temperature, media pH, concentration, particle size, surface potential/charge and ionic strength [24]. In Gram-negative bacteria, the cytoplasm protein acts as an Ag-ion reducing agent [25]. Metal-species interfere with the nutrient assimilation and induce in some cases genotoxicity. This is the case for example of Cr(VI) and As (III)-ions [26]. The effects of the Ag-particle size, shape, roughness, zeta-potential and surface potential on the bacterial inactivation are briefly described in Section 1.2.1.

1.2.1. Effect of Ag-NPs size on the kinetics of bacterial inactivation

The size of metal Ag-NPs prepared by sol-gel methods affects their adhesion and antibacterial activity. The production of Ag-NPs is expensive, involves hazardous chemicals and leads to many cases to non-reproducible Ag-NPs formulations. Particles between the range of 1–10 nm were reported to attach easily to the *E. coli* cell wall compared to micron sized Ag-NPs [13]. Furthermore, the mechanism of Ag-NPs leading to bacterial inactivation with sizes ca. 25 nm was recently reported by Sondi and Sondi [27]. Many reports show that electrostatic attraction between the negatively charged bacterial cell wall and the positively charged nanoparticles is crucial for the bactericidal activity of nanoparticles. However, Sondi and Sondi used TEM images to show that negatively charged silver particles interact with the *E. coli* cell wall leading to cell death [27]. The bacterial membrane showed a significant increase in cell wall permeability for ionic and related low size-species leading to an increased/uncontrolled transport through the cell wall, release of LPS molecules leading to cell death. The Ag-NPs preparation

Table 1
Sizes of sol-gel prepared Ag-NPs used to inactivate *E. coli*.

References	Size	Material
Choi and Zu [28]	5–21 nm	AgNO ₃ reduction by NaBH ₄
Xiu, Thang et al. [23]	3–10 nm	AgNO ₃ dilution
Lu and Chou [29]	22–24 nm	Ag ₂ CO ₃ hydrolysis
Kim, Kuk et al. [30]	8–16 nm	AgNO ₃ reduction by NaBH ₄
M. Raffi et al. [31]	~16 nm	Gas condensation
Smetana et al. [32]	100–150 nm	Solvated meta-atom dispersion
Kvitek et al. [33]	50 nm -1 micron	Tollens Process
Raffi et al. [34]	5 nm	Ag-surfactants
Navarro, et al. [35]	11–200 nm	Ag/carbonate hydrolysis
Panacek et al. [36]	25–450 nm	[Ag(NH ₃) ₂] ⁺ complex
Morones et al. [13]	5 ± 2	Ag-surfactants
Wei et al. [37]	20–40 nm	EDTA reduction of Ag-ions
S. Pal et al. [14]	10 nm	AgNO ₃ dilution
Prabhu et al. [9]	8–10 nm	Ag-PVP
Sondi et al. [27]	1–10 nm	AgNO ₃

by sol-gel from different laboratories is presented below in Table 1. This Table also shows the diverse routes for the preparation of these Ag-NPs. The bacterial inactivation kinetics cannot be directly correlated with the particle size of Ag-NPs as shown in Table 1. The experimental conditions during the Ag-NPs preparation, reaction media, pH and concentration varied considerably from one laboratory to another and this makes it difficult to compare the bacterial inactivation kinetics as a function of the Ag-NPs size in Table 1. Table 1 summarizes results on *E. coli* inactivation by Ag-NPs presenting different sizes and prepared by different synthetic routes using various precursors. Most of the previous studies did not report any bacterial inactivation times a seen in Table 1. These reports address the shape, size, ionic concentration of the media, the leaching of the Ag-ions minimum inhibitory concentration (MIN), the diffusion of the Ag-NPs in solution and other physical characteristics of the Ag-NPs. No time frame for the bacterial reduction is reported in many cases since this depends on the initial *E. coli* concentration, the initial Ag-NPs concentration and other suspension/solution parameters. Consequently, the references selected in Table 1 address particle preparation, transformation of the Ag-NPs during the disinfection process, isoelectric point (IEP) and other material aspects, and not the bacterial inactivation kinetics under conditions that would allow a comparison between samples prepared by different methods/laboratories. Therefore, there is a need to work out standard guidelines to compare the bacterial inactivation kinetics and efficiency of Ag-NPs/Ag-films leading to bacterial inactivation.

Biological methods have been developed to synthesize Ag-NPs using suitable reducing and stabilizing agents and solvents [9]. The advantages of using plant extracts are related to their availability, safety, non-toxicity and easy reduction by common reducing agents leading to Ag-ions. Flavones, organic acids and quinones are water-soluble phytochemicals that readily reduce Ag-ions. Some of the silver synthesizing plants and the resulting particle sizes of Ag-NPs are shown below in Table 2. A recent review on synthesized Ag-NPs “green” method and their antimicrobial properties has been reported [43].

1.2.2. Effect of the Ag-NPs shape on bacterial inactivation

The shape of Ag-NPs is an important factor controlling/regulating

Table 2
Silver-synthesizing plants and Ag-particle sizes.

Serial number	Organism	Ag-particle size (nm)	Ref.
1	<i>Medicago sativa</i>	2 to 20	[38]
2	<i>Azadirachta indica</i>	50	[39]
3	<i>Cinnamomum camphora</i> leaf	55 to 80	[40]
4	<i>Cinnamomum zeylanicum</i> bark	50 to 100	[41]
5	<i>Jatropha curcas</i>	10 to 20	[42]

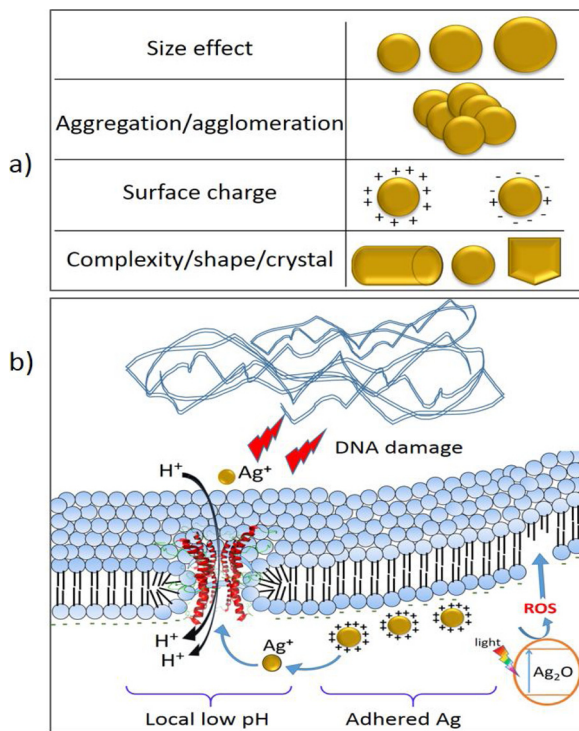


Fig. 1. a) Factors affecting bacterial inactivation by Ag-NPs: size, particle agglomeration, charge and shape, crystal. b) Scheme of bacterial inactivation by Ag-films.

their antimicrobial activity. Ag-NPs with different shapes induce a very different degree of bacterial damage when interacting with the cell wall envelope [44]. Triangular shape particles have been reported to induce a higher antibacterial activity compared to spherical particles due to the exposure of Ag-NPs presenting an increased atomic density [13]. The more effective shapes of the Ag-NPs leading to bacterial inactivation require a lower solvation energy [45], and at the same time present a large surface area for the AgOH/Ag₂O/Ag layers [46]. Cube-shaped Ag-NPs exhibit stronger antibacterial activity than sphere-shaped and wire-shaped Ag-NPs with similar diameters. It was suggested that the shape effect on antibacterial activity was related to the particle specific surface area and facet reactivity [47–49]. Ag-NPs with a rod-like shape were more effective than Ag-NPs with a spherical shape (Fig. 1) [13,44–50]. Layers made up by Ag-NPs were seen to have particle boundaries containing impurities, imperfections and dangling-bonds. These imperfections are partly responsible for the distinct electron polarizability on Ag-NPs presenting different shapes.

1.2.3. Effect of the Ag-NPs roughness on bacterial inactivation

Ag antibacterial surface present peaks and valleys. These are the attachment sites of the bacteria to the surfaces. The roughness of these surfaces is the distances between the peaks and the valleys and this value is determined by atomic force microscopy (AFM). A higher peak density allows for a larger interaction between the M-NPs (metal = M) and bacteria leading to faster bacterial inactivation kinetics. Few studies have addressed the correlation of surface roughness and bacterial inactivation kinetics.

1.2.4. Effect of zeta-potential on bacterial inactivation

Recent studies have demonstrated that the zeta potential of M-NPs has a strong influence on bacterial adhesion. Due to electrostatic attraction between the positively charged Ag-NPs and the negatively charged *E. coli* cell membrane, the Ag-NPs interact electrostatically with the negatively charged bacterial cell wall.

1.2.5. Surface potential and pH changes on bacterial inactivation

The interface potential of the Ag films in contact with bacteria shifts during the bacterial inactivation time in the dark and under light [51,52]. This is the evidence for the change in the permeability of the *E. coli* cell wall in contact with Ag films. The surface potential decrease is associated with an increase in cell permeability [51–54]. Rtimi et al., reported recently changes in surface potential for a variety of films in contact with bacteria [51,52] leading to the loss of the cell barrier control. Therefore, no more cell wall related constraints regulate the ion species diffusing in and out of the bacteria cytoplasm. Carboxylic acid intermediates are produced during bacterial degradation leading to changes in the pH surrounding the bacteria. This drives the Ag-film interfacial values to a more acidic pH, which subsequently leads to bacterial loss of viability. After the carboxylic acids decompose to CO₂ as noted below in Eq. (1), the pH recovers to its original level in the dark (Kolbe reaction) or under light (Photo-Kolbe reaction) [54,55].



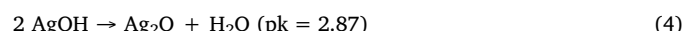
1.3. Ag-NPs leading to bacterial inactivation in the dark

1.3.1. Suggested mechanism of bacterial inactivation by Ag-NPs in the dark

Silver in its metallic state reacts with air (O₂) leading to Ag₂O. This Ag₂O generates of Ag⁺-ions as shown by Eqs. (2)–(3). These are 4 electron processes:



Henglein et al. [56] reported that Ag⁰ dissolution in the presence of air (O₂) leads to Ag release. The released Ag chemisorbs on the Ag-NPs cell wall inducing antibacterial effects and this effect can also take place in anaerobic conditions. Ag-NPs with smaller sizes increased the antibacterial effect due to the higher amount of Ag⁺-ions present per unit weight of Ag. Ag₂O was observed on the surface of Ag-NPs due to the spontaneous decomposition of AgOH as noted in Eq. (4) [57]. The core of the Ag-NPs was reported to be made up by Ag, while the AgOH is present in the 1–3 atomic surface layers (< 0.6 nm) [58].



Ag-NPs in anaerobic atmosphere penetrate the cell membrane porins and interact with the cell wall LPS mercapto(-SH), amino(-NH), and carboxyl(-COOH) functionalities. Fig. 2 shows schematically the interaction of the ROS or Ag-ions leading to the protein bacterial dysfunction in the cysteine Fe-binding sites. Evidence is available to support this mechanism [5,8,9,19,26,59]. The bacterial inactivation by Ag-NPs has been generally attributed to the following reactions: a) the binding and translocation of Ag-ions into the cell cytoplasm and b) the damage of DNA/RNA and other cytoplasm cell components [60]. Bacterial inactivation in aerobic conditions in the dark leads to: a) Ag-oxygenated species, and b) Ag-DNA/RNA interactions [61,62]. Park et al., showed the bacterial inactivation by ROS accounted for about 50% of the total damage by Ag-ions in aerobic and anaerobic media [63].

1.3.2. General considerations for the Ag-NP mediated disinfection on 2D/3D surfaces

The loading of colloidal particles or precast Ag-NPs powders on heat resistant substrates such as quartz, glass, metal plates, and ceramics involves calcination carried out at temperatures between 300 °C and higher to anneal Ag on the substrate. Colloidal suspensions of Ag are stabilized by two different mechanisms as described by the DLVO theory (Derjaguin, Landau, Verwey, and Overbeek) [64]. The first route is based on electrostatic repulsion of the Ag-positive suspensions by the addition of citrate-ions or other negative anion to preclude the Ag-aggregation by attractive forces and van der Waals forces. The second

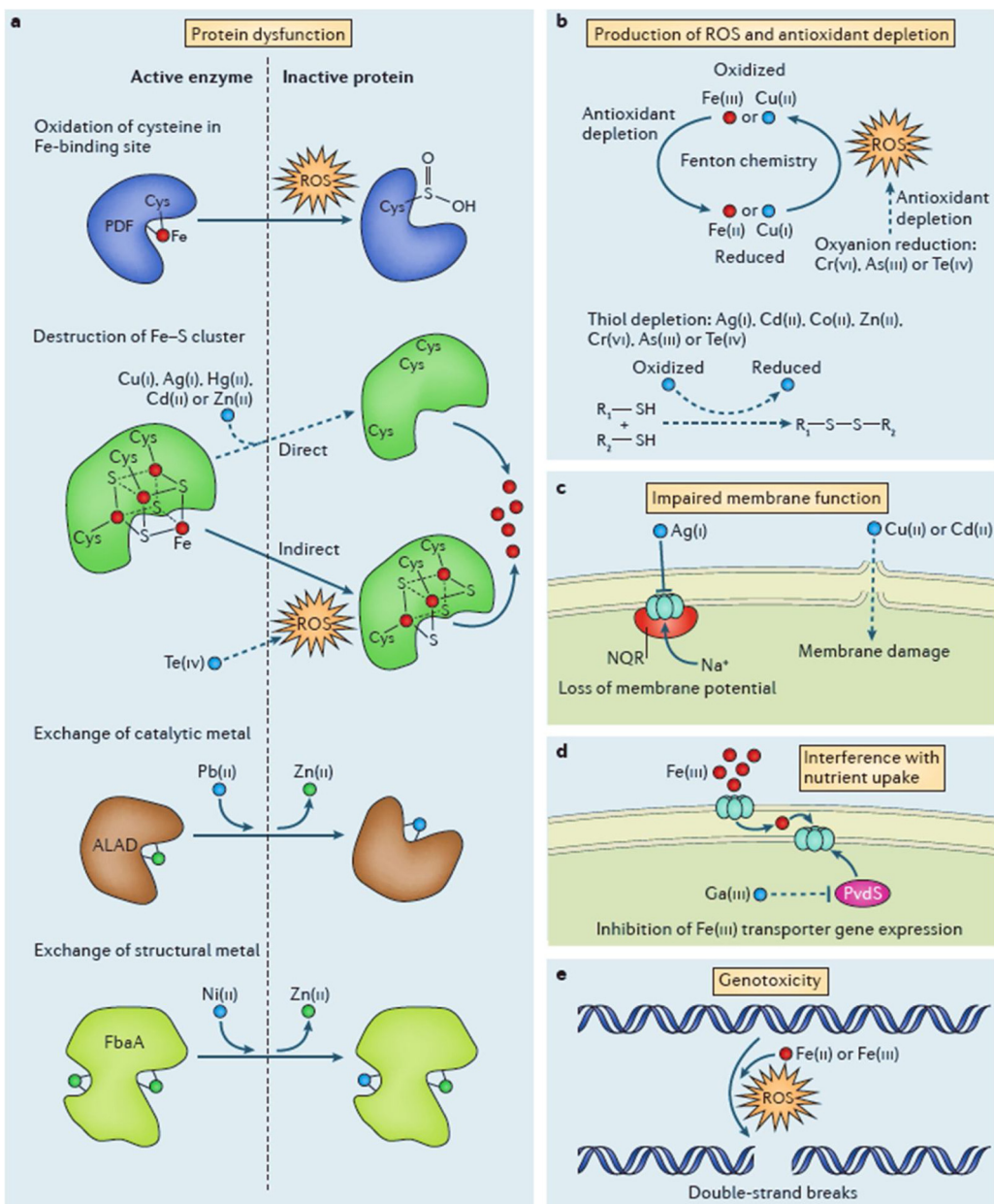


Fig. 2. Antibacterial mechanisms of metal toxicity: a) Metals leading to protein dysfunction, b) production of reactive oxygen species (ROS), c) impairing the membrane function, d) interference with nutrient assimilation, e) genotoxicity. Solid arrows represent elucidated pathways and dashed arrows represent routes where the biochemistry is unclear. ALAD, δ-aminolevulinic acid dehydratase; FbaA, fructose-1,6-bisphosphate aldolase; NQR, NADH:quinone oxidoreductase; PDF, peptide deformylase; PvdS, a σ-factor (σ24) from *Pseudomonas aeruginosa*. Reproduced from Reference [161] under the license N° 4218261057944.

route is based on the addition of steric blockers such as long-chain polymers like PVA or PVP. The stable and adhesive loading of Ag-NPs colloids on polymers/textiles with high adhesion is not possible since these materials are not heat-resistant. For this purpose, organometallic silver (I)-complexes on polyamide and polypropylene (PP) [12] and chitosan-Ag surfaces have been employed [65]. In polyurethane (PU) the Ag-submicron particles were deposited by sol-gel methods at relatively low temperatures [66]. Polyurethane is hygroscopic and the interaction with electrolyte solutions releases silver-ions at a slow rate [67]. The change in pH surrounding the bacterial outer cell wall (LPS) is an additional factor leading to bacterial loss of viability. Ag coating increases the hydrophilicity of catheters since the latter are made up from PU or silicon, both highly hydrophobic materials. Ag-coated catheters by sol-gel are effective for short times [68] and loose Ag as confirmed by analytical means. Due to this Ag-detachment, the Ag-deposition is carried out by chemical vapor deposition (CVD) or

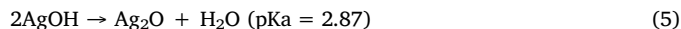
sputtering techniques [69]. Most of the loadings of Ag-colloids on textiles/polymer films presenting a low heat resistance have led to Ag-films not being robust, uniform, reproducible or adhesive [70]. Therefore, CVD and diverse forms of sputtering are used to coat different substrates and devices. In the CVD chamber, Ag composites/complexes are heated, decompose and subsequently condense on the substrate positioned in a different zone of the reactor at a lower temperature. The disadvantages of the CVD deposition are the high investment costs, the high temperatures needed precluding film deposition on polymers such as PES, PE, PU and PET and the amount of heat requiring costly cooling systems. Ag-films (6 to 50 nm) deposited by CVD led to bacterial inactivation under UV/Vis light irradiation as reported by Page et al. [71,72], Foster et al. [73], Dunlop et al. [74], Yates et al. [75] and Kelly et al. [76,77]. Adhesive, robust and reproducible films were obtained by this approach. Magnetron sputtering was also used to prepare uniform and adhesive Ag/Ag-oxide ultrathin films. The sputtered films

released Ag-aggregates/Ag-nuclei//Ag-ions. The amounts released were a function of the added Ag and the speciation of Ag.

1.4. Ag-NPs surfaces leading to bacterial inactivation

1.4.1. Mechanism of Ag-NPs charge generation under band-gap irradiation leading to antibacterial surfaces with potential application in healthcare facilities

Various bacterial inactivation mechanisms involving Ag-ions/Ag-NPs have been suggested in recent reviews [1–16,18–37]. In this Section, we focus on the bacterial inactivation mediated by light induced Ag-NPs under band-gap irradiation. This area has attracted little attention in the last decade in the field of Ag-mediated disinfection. In the presence of air (O_2) and humidity, Ag-films are covered by AgOH layers (seen 1.3.1, Eq. (4)). This layer decomposes spontaneously to Ag_2O :



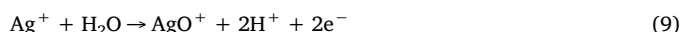
This Ag_2O is thermodynamically stable in the region of pH 6–8. The same pH stability domain is required for the survival of *E. coli* and for a wide range of bacterial species. Visible/actinic light irradiation activates Ag_2O with $1.46 < \text{bg} < 2.25 \text{ eV}$ [5–9,20] as noted next in Eq. (6):



In the presence of a semiconductor such as TiO_2 , ZnO , Fe_2O_3 the photo-generated electrons (e^-) by the semiconductor under band gap irradiation react as shown in Eq. (7):



While the photo-generated holes (h^+) in Eq. (6) react with H_2O as suggested in Eq. (8). This reaction runs parallel with Eq. (9) generating $\cdot OH$ radicals:



The irradiation of Ag-NPs induces an accelerated bacterial inactivation compared to runs in the dark [78–81]. This is possible due to

the fact that the photo-activated species generated at the surface of the Ag-NPs release Ag-ions as suggested in Fig. 3. Recent studies reported that light activated bacterial inactivation due to Ag-NPs involves *redox* reactions as detected by X-ray photoelectron spectroscopy (XPS) [82–88]. A larger application in health care facilities of the Ag-NPs should be possible by Ag-films grafted on surfaces/devices through the following ways:

- Heating of Ag-NPs on the substrate within the limits of the substrate thermal stability to adhere the Ag-particles on the substrate.
- Radio-frequency plasma (RF-plasma) pre-treatment of the polymer substrates to increase the number of negatively charged carboxylic sites able to attach the positive Ag-ions.
- Chemical vapor deposition (CVD) by way of thermal decomposition of an Ag- precursor.
- Ag-NPs direct current magnetron sputtering (DCMS) or high-power impulse magnetron sputtering (HIPIMS) of Ag-NPs [89–92]. Inactivation of Gram-negative and Gam-positive bacteria resistant to antibiotics have been addressed during the last few years by M-NPs [94]. The Ag_2O is a p-type semiconducting oxide with the same crystallographic structure as Cu_2O (cubic-cuprite) presenting a band-gap of $1.3 \pm 0.3 \text{ eV}$ [95,96].

1.4.2. Importance of the $\cdot OH$ -radicals generated by Ag-NPs under light irradiation

The AgOH noted above in Eq. (10) generates a larger amount of $\cdot OH$ radicals under light compared to runs in the dark due the reaction noted in Eq. (14) below



The optical absorption of Ag coated Ag^0/Ag_2O surfaces presents an absorption edge up to $\sim 1000 \text{ nm}$ [97]. For Fe-based disinfection processes, light activation leads to $\cdot OH$ -radicals as reported by Bauer et al. [98] due to the light absorption of the $Fe(OH)^{2+}$ bands in aqueous solution in Eq. (15).



Bolton et al., reported Fe-hydrated/soluble organic complexes with a spectral range up to 440 nm. The visible absorption of these compounds is important in Fenton type processes [99]. The generation of $\cdot OH$ -radicals as noted in Eqs. (12),(14) by Ag-NPs is important leading to the radical $\cdot OH$, that undergoes the reaction $\cdot OH/OH^-$ at a potential of $+1.90 \text{ V}$. This potential is significantly higher compared to the $HO_2^-/$

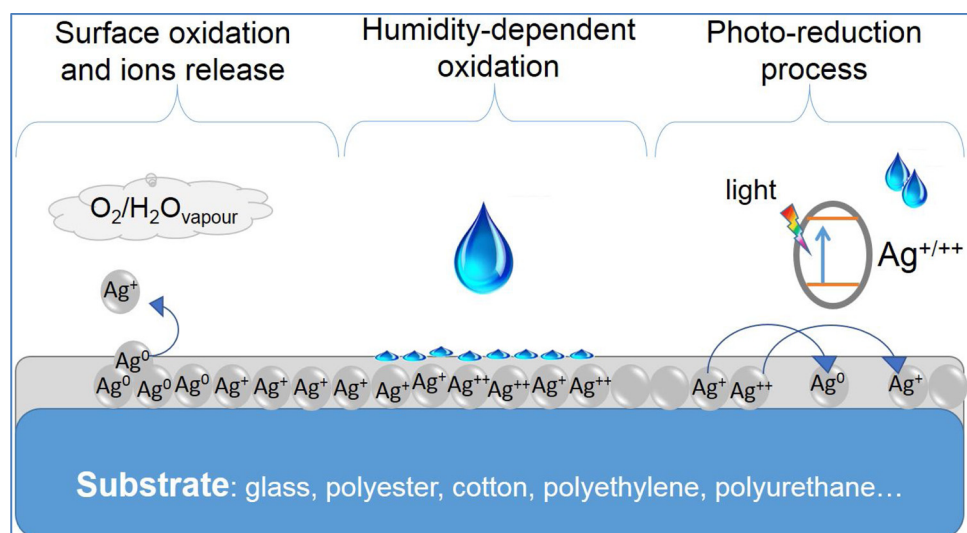


Fig. 3. Ag-NPs mediated bacterial inactivation in the dark.

HO_2^- potential of +0.75 V vs NHE [100]. The two potentials were estimated from theoretical considerations by Stanbury, since the electrochemical determination of radical species soluble in aqueous media is not possible [100]. The $\cdot\text{OH}$ radical is reported as the most effective oxidant among the ROS [101,102]. The lifetime of this radical in solution is a function of the pollutant or bacteria concentration in contact with the Ag-NPs and can be determined by fast kinetic spectroscopy [103]. The estimation of the associated solvation energies for Ag-NPs have been reported and discussed by Gerischer [104].

1.4.3. Ag-NPs coated textiles and polymer films inducing bacterial inactivation

Preparation of more advanced and effective antimicrobial films is a topic of increasing attention. These films are designed to reduce/eliminate infectious bacteria biofilms leading to hospital-acquired infections (HAI) [105]. 2D-Textile surfaces and 3D-surfaces (such as catheters or medical tools) related research is increasing at the present time to combat pathogenic bacteria becoming more resistant to synthetic antibiotics [106]. Work on antibacterial films by DCMS/DCPMS sputtering of metals, oxides and semiconductors attaining effective, stable and uniform bactericide films have been reported [107,108]. The high-power impulse magnetron sputtering (HIPIMS) allows the preparation of films showing a higher compactness and resistance against oxidation/corrosion.

Ag-based hospital textiles have shown to be able to reduce the contamination by *E. coli* and MRSA in hospital facilities. The level found for these bacteria in many UK hospitals is higher than the level allowed in hospital rooms. For example, the contamination of 10^5 CFU/cm² was observed in a diabetic wound dressing [71,51]. However, in the vicinity of the patient, a microbial density of about 10^2 CFU/cm² was found [72,51]. The use of Ag-textiles should be sufficient to decrease the bacterial concentration, since the initial concentrations are not high [109–111]. The Ag-modified textiles prepared by traditional methods show a significant release of Ag-cations in the washing process and this is a serious drawback for their use [112]. The release of Ag into water bodies through furtive emissions is a recurrent problem when used in different industrial processes. The fate of the environmental transformation of Ag-NPs released in to the environment and their associated toxicity is not fully known [113].

Sputtering of Ag reduces considerably the leaching observed of Ag-deposited on textile wound-pads by sol-gel methods [114,115]. The DCMS and the more recent direct current pulsed magnetron sputtering (DCPMS) have been carried out in the unit shown in Fig. 4. Leaching of Ag occurs from cotton and other hydrophilic textiles used in medical facilities. These textiles are able to uptake a considerable amount of water providing an effective brewing media for bacterial colonization [21]. The leaching of Ag-TiN-polyester textiles (polyester = PES) leaching up to the 8th cycle is shown in Fig. 5. The leaching proceeds at a lower level compared to the Ag-leaching from textiles where Ag was sputtered alone (in the absence of TiN) [116]. Fig. 5 presents the release of ions from PES sputtered by Ag, TiN-Ag and TiN. For Ag-sputtered samples up to the 8th cycle, the level of Ag-release is seen to be 6 and 8 ppb/cm². In the case of TiN-Ag samples, the Ag-release was observed to decrease with the number of recycling down to 5 ppb/cm². A release of Ag-ions > 0.1 ppm had a significant antimicrobial effect. Higher Ag-ions concentrations > 0.35 ppm can be toxic to human cells [116]. The TiN polyester samples lead to a release of ~14 ppb/cm² of Ti-ions as shown in Fig. 5. The excellent biocompatibility of TiN is certainly an advantage for antibacterial applications and has been documented in biomedical applications [117]. Acceptable bactericidal kinetics coupled with low cytotoxicity are the two essential requirements for effective bactericide surfaces. With some Ag-compounds, the bacterial inactivation was observed to proceed through an oligodynamic effect in the dark [118,119]. The leaching of Ag in the ppb concentration range inducing an oligodynamic effect was observed to be a few orders of magnitude below the values reported for colloidal grafted Ag-textiles.

1.5. Microstructure of nanoparticles on surfaces sputtered by DCMS, DCPMS and HIPIMS: Critical issues

Sputtered films on surfaces are formed involving nucleation and growth. Atoms coalesce into small clusters and later form anisotropic or isotropic agglomerates leading to films with thicknesses that are a function of the sputtering time. Two main interactions determine the sputtered film microstructure: 1) the interaction of the clusters with each other and the interaction of the sputtered particles with the substrate leading to the film epitaxial growth, and 2) the Ag and Cu-condensation on the surface binding to each other rather than to the substrate. This leads in some cases to near-spherical compact clusters not presenting a crystallographic network [120–123]. Low-energy sputtering either by DCMS or DCPMS increases the mobility of the ad-atoms diffusing/coalescing on the substrate surface [121]. The temperature of the sputtered film is determined by the sputtering time and the energy of the impinging atoms/metal/ions [124].

The distribution of the sputtered metal/metal oxide films on the substrate depends on the nanoparticle polarization, electrostatic inter-particle effects, diffusion of the surface species, adhesion to the surface and cohesive forces binding the M-NPs to the substrate. Generally, the adhesive forces - an important parameter in Ag-NPs - are a function of the physical interaction with the substrate, the chemical bonding or chemisorption to the substrate and the mechanical interlocking with the substrate [120–125].

Intimate bonding between antibacterial metals like Ag, Cu, Ag-Cu and the substrate is not attained if the substrate presents an irregular surface morphology/roughness. A. P. Ehiasarian has reported nitrides sputtered surfaces showing highly aligned coalescent layers. This leads to smooth/flat films without formation of grain boundaries [125]. During the last few years, sputtering of Ag on sputtered nitride under-layers was reported. An intimate bonding to the substrate by the M-nitride layers was obtained and the bacterial inactivation kinetics and film properties investigated. The Ag-nitride films presented a uniform microstructure, adhesion and uniformity [116,117,126–128]. In some cases, the sputtered nitrides closely duplicated the substrate structure. Epitaxial growth by the nanoparticles on top of the film led to a strong adhesion of the sputtered layers to the substrate [129].

Similar beneficial effects for the adhesion of metals on a selected substrate have been obtained by sputtering TiO_2 under-layers to prepare adhesive films active in pollutant and bacteria degradation [102,130]. The TiO_2 adhesive properties lead to a higher adhesion of the top-most sputtered metal/ metal oxides on the TiO_2 under layers. This induced a synergistic interaction between the metal/oxide and the TiO_2 favorable in bacterial inactivation and pollutant degradation processes [131–133]. Ag-antibacterial coated polymers leading to bacterial inactivation have shown some stability problems during their use as reported by K. Vasilev [134,135].

Low-energy sputtering either DCMS or DCPMS on substrates increases the mobility of the surface ad-atoms coalescing on the substrate surface [120,121]. These simultaneous processes are described graphically in Fig. 6. The low rate of DCMS-deposition is proportional to the applied power to the target. To overcome this disadvantage, electromagnets are placed behind the target(s) and this process is referred to as direct current magnetron sputtering (DCMS). The orientation of the electric and magnetic fields forces the electrons to follow a hopping trajectory close to the target leading to more collisions with the gas atoms. As consequence, a higher flow of ions is produced in the direction of the target. This increased ion flow increases the deposition rate.

To prevent arc formation during the deposition, pulsed discharges can be introduced by neutralizing the surface charges. This process is called direct current pulsed magnetron sputtering (DCPMS). Positive charges accumulate near the target hindering the deposition. Periodic interruption of the negative DC-voltage eliminates the accumulated positive charges on the target. This process is attractive because it offers

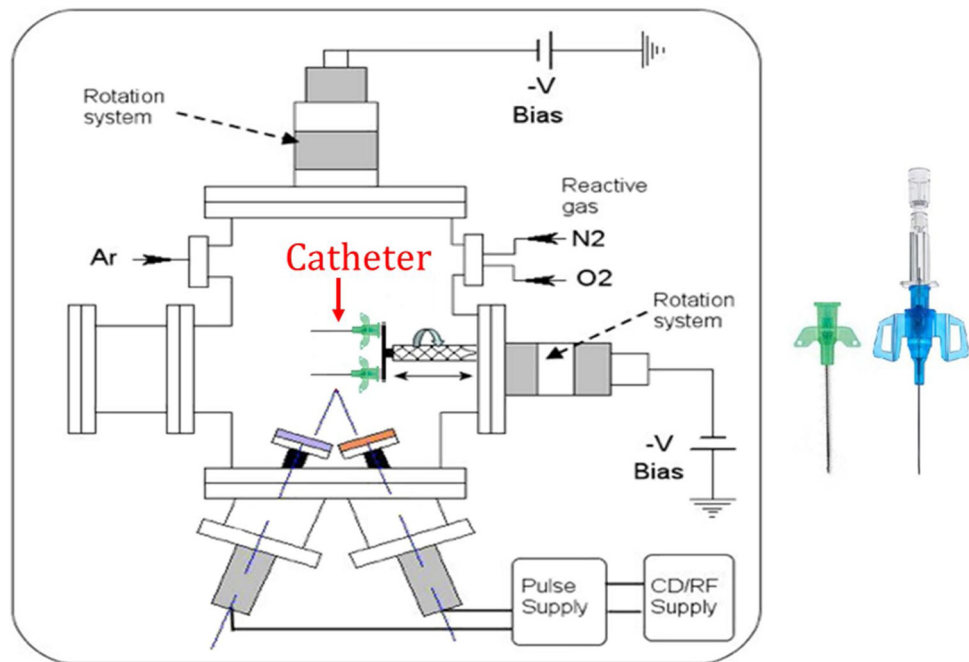


Fig. 4. Scheme of the direct current magnetron sputtering (DCMS) unit used to sputter 2D and 3D surfaces (catheters).

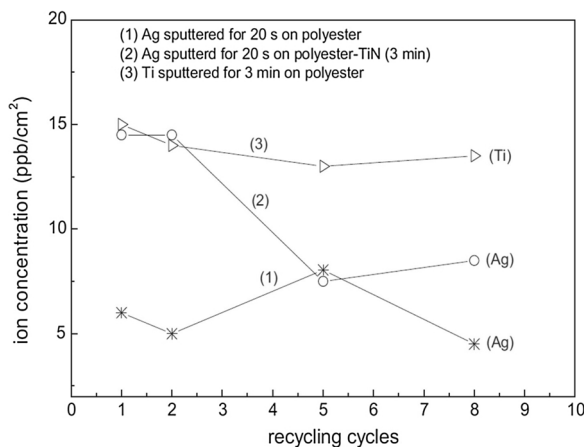


Fig. 5. Ion-coupled plasma spectrometry (ICPS) determination of Ag-ions and Ti-ions released during the recycling of (a) sample sputtered with Ag for 30 s (trace 1), (b) TiN-Ag (3 min–20 s) sputtered sample and (c) TiN sample sputtered sample for 3 min (trace 3). Reprinted with permission of S. Rtimi et al., (2012). Other details are given in the respective reference [116].

stable arc free deposition of films on architectural and automotive glass, or antireflective/antistatic substrates. The applied power in DCPMS mode is limited by the heat resistance of the target used.

High power impulse magnetron sputtering (HIPIMS) is a recent development designed to prepare denser coatings. HIPIMS uses very short pulses with power densities exceeding the DC power density by about two orders of magnitude. The sputtered material creates metal-based plasma in contrast with gas plasma for conventional DCMS. By the application of HIPIMS to coat surfaces in the car and plane industries, the anticorrosive Fe-Cr HIPIMS coatings lead to high-density coatings due to the increased ionization of the sputtered species. In addition, HIPIMS improves the direction of the flow of the metal-ions in the sputtering chamber. Furthermore, the plasma density of the conventional magnetron discharges increases with the applied power to the cathode. To avoid the heating limitation, the duration of the high-power pulses can be shortened. A dead recovery period is introduced in a repetitive way that is sufficiently long so that the heat accumulated on

the surface of the target dissipates. It should be noted here that the HIPIMS sputtering requires time-consuming calibrations before it can be applied.

1.6. Nitride selection when using antimicrobial metal nitrides under light irradiation: TEM-microstructure of Ag-nitride films

The significant role of the metal in the Ag-nitride bacterial inactivation kinetics is readily seen next in Fig. 7. This Figure shows the accelerated bacterial inactivation kinetics induced by Ag-TaN compared to Ag-ZrN and Ag-TiN [128]. The 20 min bacterial reduction time induced by Ag-TaN represents a drastic decrease compared with Ag-TiN inactivating bacteria within 100 min and Ag-ZrN inactivating bacteria within 90 min under low intensity indoor light (4 mW/cm², Lumilux/Osram LW18 W/827). The initial induction period in Fig. 7 was observed to last for around 100 min for Ag and 60 min for Ag-TiN and Ag-ZrN. However, it was only 15 min for Ag-TaN. This induction period is a low kinetics bacterial inactivation phase followed by faster kinetics in a later stage.

To find an explanation for the shorter bacterial inactivation kinetics induced by Ag-TaN, (Ta⁵⁺ 0.73 Å) compared to Ag-TiN (Ti⁴⁺ 0.64 Å) and Ag-ZrN (Zr⁴⁺ 0.87 Å) is challenging. The sizes of the cations do not provide a plausible explanation. Due to the similarity in ionic *radii*, it is possible to discard nitride cation size to rationalize the observed kinetics. However, there is a significant difference in the potentials of TaN undergoing Ta⁵⁺/Ta⁶⁺ redox reactions compared to TiN and ZrN undergoing M³⁺/M⁴⁺ reactions [36]. The redox potential values for the Ta, Ti and Zr-nitrides depend heavily on the nature of the composite compound. The redox potentials in these composites are not known and this is why they are not cited here. The indicative potentials reported for the reduction of the metals in solution are not valid. The exact value of the reduction potentials in the Ag-nitrides presented in Fig. 7 is not known. The chemical species and the oxidation state of the Ta, Ti and Zr in the composite nitrides cannot be determined. One possible explanation for the bacterial inactivation kinetics induced by the different M-nitrides is the higher electrostatic charge of Ta⁶⁺ compared to Ti⁴⁺ and Zr⁴⁺. This point has never been addressed and needs further investigation.

The overall reaction for the bacterial inactivation shown in Fig. 7

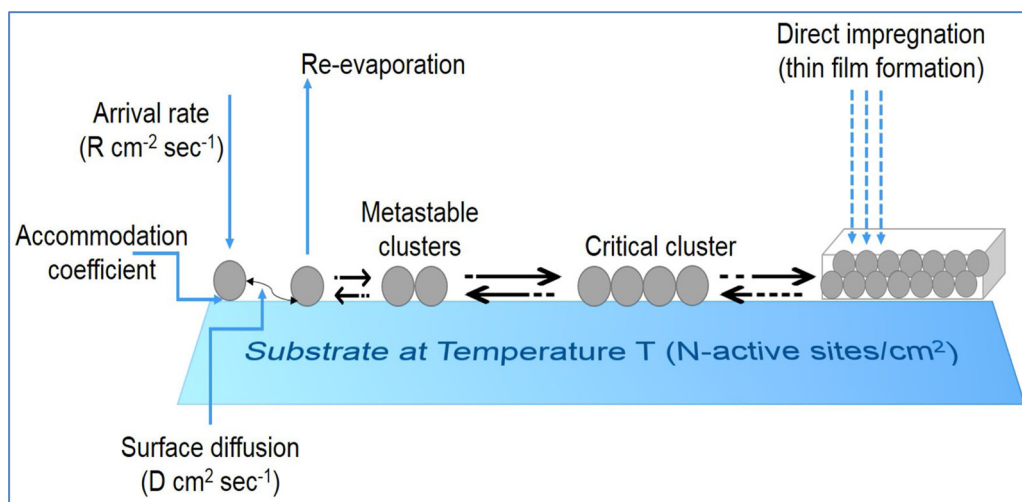


Fig. 6. Dynamics of the nucleation and growth of crystals and aggregates sputtered on a surface. For other details see text.

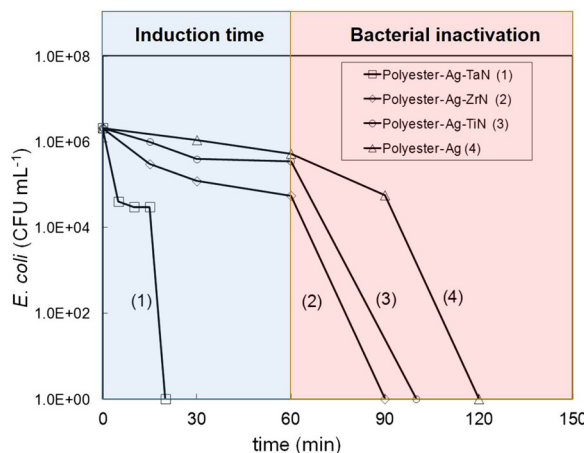
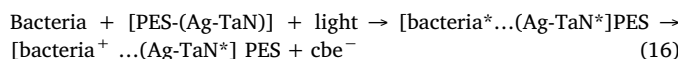


Fig. 7. Comparative bacterial inactivation kinetics of *E. coli* on the following supports: 1) Ag-TaN-PES, 2) Ag-ZrN-PES, 3) Ag-TiN-PES and 4) Ag-PES under indoor actinic light. Reprinted with permission of O. Baghrache, et al., (2015). Other details are given in the respective reference [128].

induced by the Ag-TaN PES can be written up in a simplified form as:



The term cbe^- refers to the conduction band electron of Ag_2O ($\text{cb}^- - 1.3 \text{ eV NHE}$) that transfer to Ta_2O_5 under low intensity solar /actinic light.

Reactions mediated by $\text{Ag}/\text{Ag}_2\text{O}$ generating ROS leading to bacterial inactivation have been described above by Eqs. (2)–(15). During the bacterial inactivation processes reported in Fig. 7, a pH decrease of 0.2 units was observed. This is the equivalent to the doubling in the concentration of long-lived cations or to the H^+ present in the system. In some cases, the shift to more acidic pH-values suggests the minor role of the OH/OH^- (1.90 eV) in the reaction sequence [136]. This is indicative of the presence of the $\text{HO}_2/\text{H}^+ + \text{O}_2^{\cdot-}$ (0.75 eV) participating in the reaction mechanism [136]. This later radical couple with a lower potential is frequently present at the physiological pH 6–8 at which the bacteria exist [102,137–139].

Fig. 8a presents the microstructure of Ag-TiON determined by TEM Bright Field (BF) [140]. Conventional TEM (not shown) revealed a dark continuous coating 100 nm thick for TiON-Ag samples. These samples were sputtered for 4 min from a Ti-target in reactive O_2 atmosphere to deposit TiON followed by Ag-sputtering for 30 s on the PES substrate.

The $\text{Ag}-\text{Ag}_2\text{O}$ particles presented sizes between 20 nm and up to 40 nm in the ~70 nm thick topmost layer of TiON-Ag. These $\text{Ag}-\text{Ag}_2\text{O}$ nanoparticles will not penetrate/translocate through the bacterial cell wall porins with a diameter of 1.1–1.5 nm [141,142]. This suggests that the Ag-induced bacterial inactivation proceeds only partially by way of Ag-ions with sizes < 1.1–1.5 nm. Therefore, a surface-contact mechanism involving Ag-NPs intervene in bacterial inactivation. Fig. 8b presents the TEM of co-sputtered ZrON-Ag (90 s) samples on PES. In the left-hand side the Zr and Ag are shown to be immiscible when co-sputtered on PES since two well-defined bands for ZrON (90 s) and Ag (20 s) were formed. The right-hand side of Fig. 8b shows the Zr and Ag-nanoparticles contrasted by high angular annular dark field (HAADF). The sizes of the ZrO_2 and Ag nanoparticles in co-sputtered ZrNO-Ag (90 s) film were 8–13 nm and 8–15 nm, respectively. The co-sputtering of Zr and Ag stabilizes the ZrON-Ag composite and slows down the release of Ag.

1.7. Evidence for the interfacial charge transfer (IFCT) mechanism in semiconductors under light leading to bacterial inactivation

The mechanism of bacterial inactivation mediated by TiON-Ag is suggested in the scheme shown in Fig. 9. Visible light reaches TiON-Ag and leads to the formation of Ag_2O . This can be due to: a) the partial oxidation of Ti/TiON and Ag in the presence of the residual H_2O vapor in the sputtering chamber at a pressure of $\text{Pr} = 10^{-4} \text{ Pa}$. This pressure corresponds to about $10^{15} \text{ molecules/cm}^2$ of H_2O . This is equivalent to a water monolayer and is sufficient to generate the oxidative-radicals required for the partial or total oxidation of the TiON-Ag composite film forming Ag_2O and TiO_2 , b) the TiON-Ag films can also oxidize after being taken out of the sputtering chamber and c) when exposed to humidity during the sterilization process when autoclaved at 121 °C.

The Ag film when exposed to air (O_2) and humidity (H_2O_v) leads to Ag_2O as mentioned previously in Eqs. (5)–(10) (see Section 1.3.1 and 1.3.2). Ag_2O is stable at pH 6–7, the pH-region where the bacterial inactivation of *E. coli* is investigated. Light irradiation in the UV/visible range activates Ag_2O presenting a band gap (bg) of $1.3 \pm 0.3 \text{ eV}$ [95–97] and TiO_2 with bg 3.2 eV [102]. The charge transfer in $\text{Ag}_2\text{O}/\text{TiO}_2$ is related to the size of the nanoparticles [143] and is facilitated by the position of the electronic energy bands of Ag_2O and TiO_2 . Under visible light irradiation, the transfer of charge from Ag_2O to TiO_2 is thermodynamically favorable. The position of the Ag_2O cb at 1.3 eV NHE at pH 0 and the vb of $\text{Ag}_2\text{O} + 0.2 \text{ eV NHE}$ at pH 0 lie above the $\text{TiO}_2\text{cb} - 0.4 \text{ V vs NHE}$ and of the TiO_2vb at +3.2 V NHE respectively. The Ag_2O cb electron injection into the TiO_2cb hinders partially the electron-hole recombination in Ag_2O . The transfer of Ag_2O electrons to

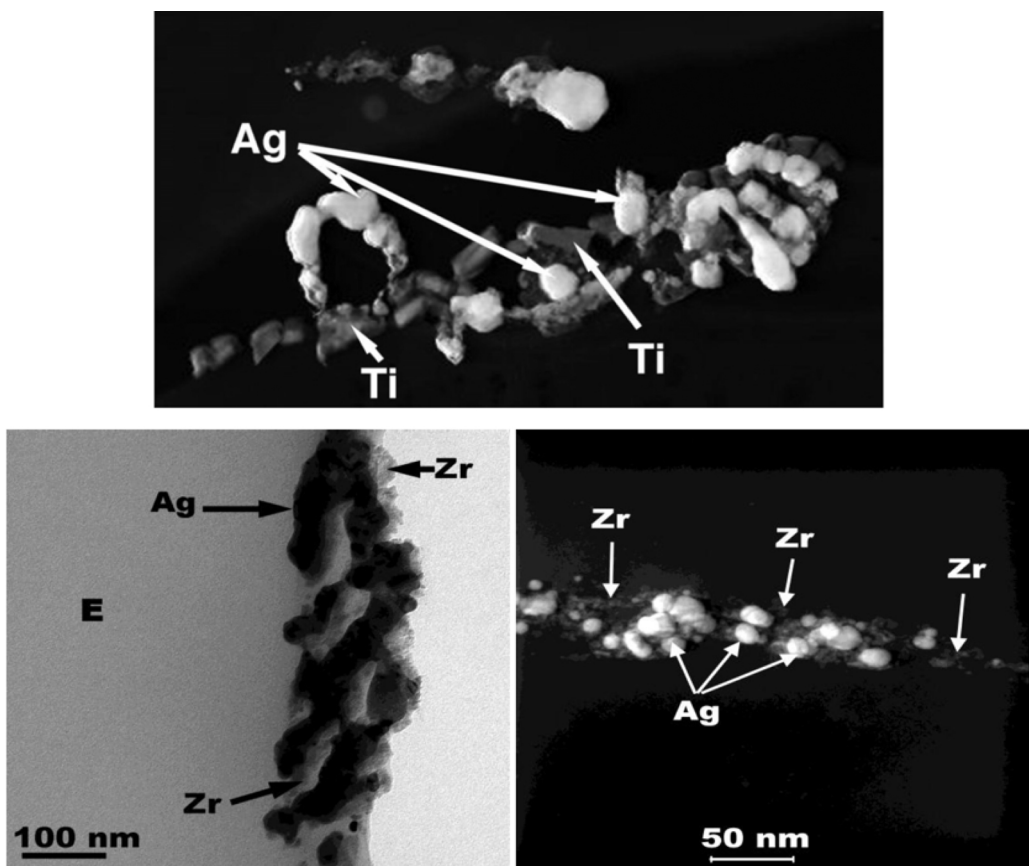


Fig. 8. Transmission electron microscopy (TEM) of Ag-TiON and b) Ag-ZrON sputtered on PES. For other details, see text. Reprinted with permission of S. Rtimi et al. (2012). Reprinted with permission of S. Rtimi, et al., (2012). Other details are given in the respective reference [116].

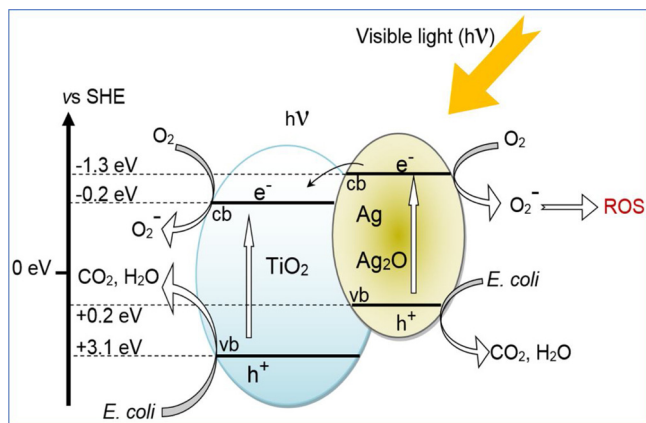


Fig. 9. Suggested reaction mechanism for the visible light photo-induced electron injection by Ag_2O into TiO_2 . Reprinted with permission of S. Rtimi, et al., (2016). Other details are given in the respective references [144,145].

O_2 also decreases the charge recombination enhancing the photocatalytic activity leading to bacterial inactivation. The right-hand side in Fig. 9 shows the generation of the ROS intermediates leading to bacterial inactivation. The values for the position of the electronic potential energies of the cb and vb in Ag_2O and TiO_2 are only indicative, since in quantum size nanoparticles, the position of the electronic band potentials shifts to more energetic values [144]. The potential of the cb in Ag_2O nanoparticles would be at a more negative value compared to the standard -1.3 eV found in the electrochemical tables. This would provide a higher driving energy (potential) for the electron injection into TiO_2 leading to a faster rate of reaction. Coupled semiconductors in

close contact present increased surface defects and this may or may not accelerate the charge transfer under light [145,146].

1.8. Dependence of the Ag-nitride mediated bacterial inactivation kinetics on the applied light dose

Fig. 10 presents the bacterial inactivation kinetics mediated by the photocatalyst Ag-TaN as a function of the applied light dose. The bacterial inactivation kinetics is seen to be dependent on the applied light dose [128]. This is a proof for the semiconductor character of the Ag-TaN. In the presence of oxygen, the Ag-TaN becomes $\text{Ag}_2\text{O}/\text{Ta}_2\text{O}_5$.

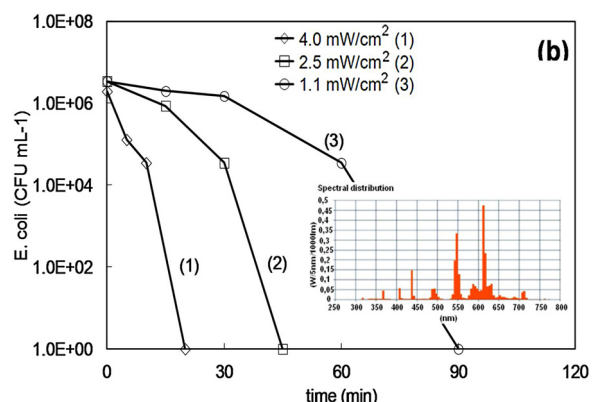


Fig. 10. E. coli bacterial reduction kinetics on Ag-TaN PES co-sputtered for 20 s on PES as a function of the applied light dose. Irradiation source L18 W/827 Lumilux/Osram (4 mW/cm^2). Reprinted with permission of O. Baghriche, et al., (2015). Other details are given in the respective reference [128].

Semiconductors like Ag_2O , TiO_2 and Ta_2O_5 photo-generate charges as function of the applied light intensity. TaN shows a faster bacterial inactivation kinetics compared to Ti and Zr -nitrides [128]. In a similar way, Ag-TiON is transformed to $\text{Ag}_2\text{O}/\text{TiO}_2$ due to the residual H_2O_v , which decomposes to O_2 in the magnetron chamber. Moreover, the nitride exposure to air before use leads to surface oxidation.

1.9. Effect of the sputtering energies on the film microstructure and the bacterial inactivation kinetics

Magnetron sputtering has been applied with high energies to enhance the film quality, adhesion and compactness [146]. High impulse magnetron sputtering (HIPIMS) induces a higher plasma density and ionization. The increased arrival energy of the metal-ions on the substrate leads to higher alignments of the metal-ions. This in turn induces a different growth of the sputtered crystallites leading to a more compact surface coverage and adhesion of the metal (or metal oxide) films [147]. The average energy of the ions in the HIPIMS chamber is 3 times higher compared to the ones induced by conventional DCMS/DCPMS. HIPIMS generators providing higher energies to the target surface (with different target dimensions) have been developed during the last few years [148]. The first HIPIMS was reported in the seminal article by Petrov et al. who demonstrated an improvement in the adhesion, wear, smoothness, oxidation resistance and structure of sputtered layers on a variety of surfaces [125,149]. Enhanced film adhesion is of much interest in antibacterial coatings and is related to the promotion of epitaxial growth on the selected substrate [150]. The elimination of growth defects in the crystals sputtered by HIPIMS was observed in some cases [151]. In a recent study, the inactivation time of *E. coli* by DCMS and HIPIMS has been reported on sputtered Ag-polyester (PES) [152]. Fig. 11 shows the inactivation time of *E. coli* as a function of the thickness of the prepared films/coatings by DCMS, DCPMS or HIPIMS. Fig. 11 shows a significant reduction of the Ag-layer thickness sputtered by HIPIMS compared to Ag-layers sputtered by DCMS. This means that a lower amount of Ag is needed to inactivate bacteria. Transmission electron microscopy (TEM) showed a larger coverage of the PES fibers by HIPIMS sputtered Ag nanoparticles reaching > 70% coverage compared to the case when the sputtering was carried out using DCMS. The HIPIMS was applied at a current density of 260 mA/cm^2 vs a current density of 15 mA/cm^2 in the case of DCMS-sputtered samples. The ionization observed for the Ag-ions exceeded several times the 1–3% level by DCMS-sputtering. The higher density of the residual Ag-ions left on the HIPIMS Ag-PES surface is possibly the cause for the better

performance of the HIPIMS sputtered films accelerating bacterial inactivation compared to the DCMS/DCPMS samples. Several recent studies have reported on the HIPIMS coating of different substrates such as cotton, polyester, and polyethylene [153–155].

Part 2: Cu-based antibacterial materials

2. Introduction

2.1. Cu as antimicrobial particles (Cu-NPs) and Cu-films: Critical issues

The use of copper in bacterial inactivation is addressed in this section. The interest in Cu-NPs has grown in the last decade since extremely low amounts of Cu induce bacterial inactivation in the dark. The reason for this is the high cytotoxicity of Cu per unit weight compared to Ag. In addition, illuminated Cu shows accelerated bacterial/fungi inactivation kinetics concomitant to the low cytotoxicity toward mammalian cells.

Copper is number 29 of the periodic table of elements. The Cu atomic structure consists of negatively charged electrons in completely filled orbitals close to the positively charged atomic nucleus. The electrons of the unfilled orbitals $4s^1 3d^{10}$ require a small input of energy to activate chemical reactions. Cu(I) ($4s^0 3d^{10}$) and Cu(II) ($4s^0 3d^9$) oxidation states require a much lower one electron *redox* potential compared to Fe(II)/Fe(III) electron transfer needing higher potentials. Many gram-negative bacteria include Cu in the periplasm and are able to handle the toxicity of copper cations up to a certain level in metabolic reactions. Excess cytoplasmic/periplasmic copper cations are removed by efflux of glutathione or Cu^+ or oxidized to the less toxic Cu^{2+} . Inactivating bacteria on metallic copper surfaces is associated with the release of copper-ions and to the surface-contact of the bacteria with Cu-nanoparticles. Copper is essential for a variety of biochemical reactions involving O_2 such as terminal oxidases or Cu/Zn superoxide dismutase. Unbound copper cations participate in Fenton-like reaction leading to rapid oxidative cellular damage involving ROS.

Some years ago, Karlin and Salomon [156] published a series of articles on the role of Cu-enzymes as terminal electron acceptors in the respiration cycle. Cu in the enzymes alternates during their reactions between Cu(I) and Cu(II) [157]. Cu is of crucial importance in the electron transfer in biological structures being present at ppb concentrations. Its cytotoxicity in the human body leads to the excessive generation of oxidative radicals. Above certain concentrations when the rate of Cu-uptake exceeds the rate of Cu-ions release, the amount of Cu-present hinders the functioning of the cell-enzymes regulating the cell respiration/replication/metabolism/viability. The use of Cu-nanoparticles to treat skin infections and skin wounds is being intensively explored at the present time. The chronic treatment of wounds is today a major problem in the healthcare sector at a worldwide scale. Cu can be used safely under the condition that the Cu-particles should present a size $> 100 \text{ nm}$. This is the average size of the skin pores and Cu-particles above this size will not diffuse through the skin into the blood stream. If the Cu diffuses in to the blood, Cu-ions catalyze the production of ROS and induce DNA and protein damages especially on histidine and proline leading to their cleavage [158]. Cu-particles are also known for their antimicrobial activity, although they have been investigated to a lesser degree compared to silver. There are no clear proofs suggesting the antimicrobial resistance to Cu. This involves a mechanism not completely understood at the present time. Cu-presents: a) a higher cytotoxicity by unit weight compared to Ag, b) a lower cost compared to Ag and c) higher availability in nature. Cu/CuO in the ppb range induces cytotoxicity to pathogens in amounts below the sanitary limits stipulated by regulations for their use in human cells. On this basis, the Cu uses in the medical field are today highly investigated mainly for external applications.

The antibacterial effect of Cu has been mainly assigned to: a) surface-contact killing, b) Cu-ions, and c) ROS generated by Cu in the

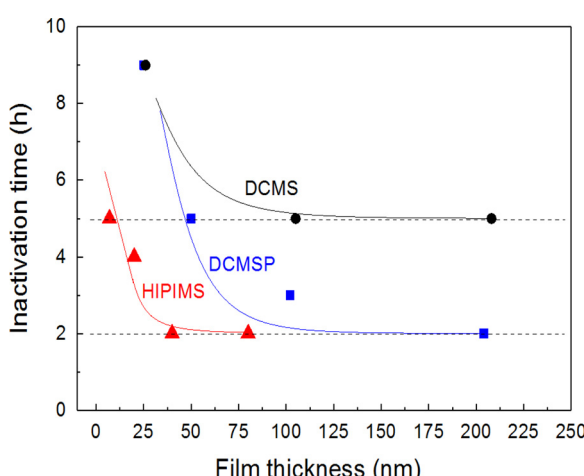


Fig. 11. Bacterial inactivation time of *E. coli* as a function of nominal thickness of the Ag coated PES sputtered by: DCMS, DCPMS or HIPIMS. Reprinted with permission of O. Baghriche, et al., (2012). Other details are given in the respective reference [152].

presence of O_2 . Bacterial inactivation induced by Cu has been recently reported to take place under aerobic and anaerobic conditions [159]. Antibacterial agents are very important in the textile industry, water disinfection, medicine, and food packaging and involve Cu-related materials [160,161]. Antibiotics have some disadvantages, including toxicity to the gastrointestinal microbiota in human body. The interest in inorganic antimicrobial agents such as metal oxide nanoparticles (Cu-NPs) is in their potential use in HAIs prevention [162,163]. This section of the review focuses on the properties and applications of Cu-textiles and polymers. In addition, it presents features of the Cu-mediated bacterial inactivation under light accelerating the bacterial inactivation kinetics [164–166]. Polymer surfaces containing different amounts of Cu nanoparticles have been prepared by the melt mix method. With only 1% Cu by weight, these surfaces were able to inactivate > 99.9% of the bacteria after 4 h contact [167]. What makes Cu-formulations important is that they inactivate *E. coli* and *Methicillin-resistant Staphylococcus Aureus* (MRSA) in the dark within acceptable times [167–170]. Some bacterial strains are resistant to the effect of antibiotics and survive high concentrations of antiseptic/antibiotics. However, these bacteria do not generally survive the Cu-induced cytotoxicity. This is the case for bacterial strains of the *S. aureus* variety [5,171,172].

2.2. Cu-surfaces and catheter devices obtained by sol-gel methods

The bactericide properties of Cu colloids and Cu-NPs in the dark and under light have been known for a long time as reported by Borkow et al., [164–166] and Espirito-Santo/Grass et al. [173–176]. These research groups reported that Cu-NPs on dry metallic surfaces were able to inactivate bacteria not needing the presence of ROS-radicals in solution. Hashimoto et al. [177,178], reported seminal work on Cu-NPs leading to bacterial inactivation under light irradiation and also under dark conditions. Inactivation in the dark is important since this is a continuous process not needing an outside energy source implying additional costs. Elguindi et al. [178], reported the kinetics of *Pseudomonas aeruginosa* inactivation by Cu, and Keevil et al., [179–181] reported the inactivation of several bacterial germs on Cu-surfaces. Gedanken et al., has lately reported innovative sonochemical methods to load Cu-NPs on antibacterial textile surfaces [182,183]. It is beyond the scope of this review to cite in a comprehensive way all the references related to the Cu biomaterials and Cu-NPs preparations, nonetheless relevant references were reviewed. Recently, Cu-NPs have been reviewed by Cioffi et al. [184]. Chloride salt-based synthesis of Cu-NPs with a high antibacterial activity was reported [185,186]. Several other Cu antibacterial preparations have been reported [187–191]. Controlled Cu-release from silica and glass biomaterials mediating disinfection have been reported by Aina et al. [192], and Cu self-disinfecting surfaces in orthopedic implants have been addressed by Fritsche et al. [187–191,193]. The incipient research of Cu-nanoparticles for anti-fungal paint formulations has been recently reported [194].

2.3. Sputtered films leading to bacterial inactivation in the dark and under light

The Cu-coating of antibacterial surfaces on non-heat resistant substrates (textiles and polymers) is an active field of research. DCMS has been used for the deposition of metals, metal oxides and doped metal-semiconductors on polymers and textiles. Furthermore, sputtering on glass and iron plates were reported by Kelly et al. [195], Sarakinos et al. [196], Lin et al. [197] Bandorf et al. [198] and Rtimi et al. [199]. In a recent study, Cu-sputtered cotton by DCMS was shown to induce fast *E. coli* inactivation in the dark and under light irradiation [200,201]. Fig. 12 shows the set-up used to irradiate the sputtered Cu-cotton samples leading to the observed bacterial inactivation [201].

XPS was carried out during the bacterial inactivation time to identify changes in the surface content, the generation of new species and

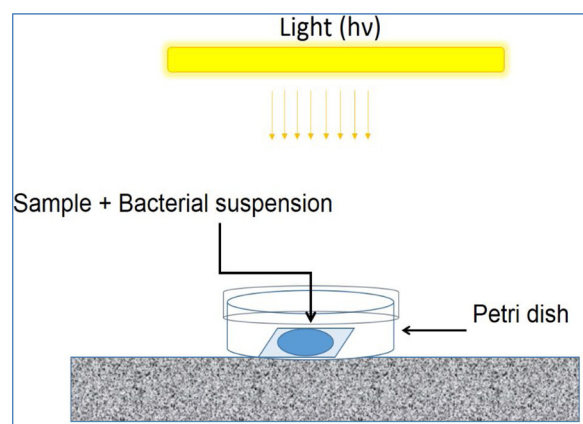


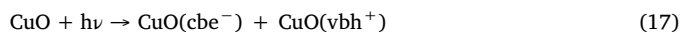
Fig. 12. Scheme of the experimental set-up to monitor the bacterial inactivation under low intensity solar simulated light.

the redox changes in the surface composites. The observed changes in the peak intensity and shifts in the binding energies (BE) of Cu° , Cu^+ and Cu^{2+} provide the evidence for redox reactions taking place during the bacterial inactivation time [202]. The Cu^+/Cu° peaks found by XPS for Cu sputtered PES centered at 930.2 eV could not be unambiguously deconvoluted without introducing a large approximation when assigning the peaks for Cu° and Cu^+ (932.8 eV). The XPS of Cu-sputtered PES peaks in the samples a) before, and b) after bacterial inactivation were observed to shift in the XPS-spectrogram [203]. The Cu_2O content in the PES was reduced from 80% to 68% after 60 min. Concomitantly, the CuO (Cu^{2+}) peak at 934.32 eV increased from 13.67% to 31.76% after bacterial inactivation. The Cu° peak at time zero at 931.5 eV at 6.6% vanished after the bacterial inactivation. This is the evidence for Cu redox reactions occurring during the time of bacterial inactivation.

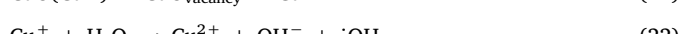
The Cu-ions produced in the Ar-plasma can lead to Cu-films by epitaxial growth through nucleation processes and agglomerates are necessary to attain the size of Cu-NPs showing metallic character [120]. The condensation of Cu nuclei leads to Cu-atoms binding to other Cu-atoms and giving raise to agglomerates [121]. Depending on the Cu-sputtering time and energy, Cu-clusters are formed but they are not necessarily crystalline. This last step depends on the affinity between the Cu-atoms and the substrate. Once on the substrate, the Cu-species interact with O_2 (air) leading to CuO or Cu_2O . CuO under light irradiation photo-generates charges as a function of the applied light dose [144]. Grafted Cu on diverse surfaces presenting antibacterial properties have been reported elsewhere [204–206].

2.4. Cu bacterial inactivation under light and in the dark: Scientific bases

CuO -films show a band-gap (bg) ~ 1.7 eV, with the conduction band (cb) at -0.3 V SCE and a valence band (vb) at $+1.4$ SCE. The photo-catalytic mechanism of CuO films under band-gap irradiation, is suggested next in Eqs. (17)–(21) [170].

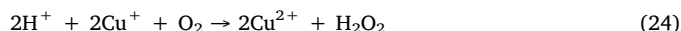


Under photon energies exceeding the CuO band-gap, the cb-electrons react directly with the O_2 forming O_2^- as noted in Eq. (18) or reduce the Cu^{2+} to Cu^+ as shown below in Eqs. (19)–(21)



Studies report bacteria being rapidly inactivated by Cu-ions/Cu-NPs, but the specific role of the Cu-species during the *redox* reactions is not clear. Cu-ions are highly oxidative radicals in Haber-Weiss/Fenton-like reaction mechanisms [175–180] leading to the generation of ROS and inducing DNA toxicity/mutations [207].

Cu(II) associate with the protein sulphhydryl (R–SH) groups as function of their affinity [160,161]. The reactions involving Cu-S lead to radicals as shown in Eqs. (23)–(24). Cu-ions have been reported to reduce R–SH (sulphhydryl) in cysteine (see Eq. (23)).



These radicals lead to DNA cellular toxicity/mutations. The Cu-S dehydratase exposed to excess Cu disintegrates. These Fe-S and Cu-S groups are essential for the cell metabolism [208]. The reactive ·OH-radical oxidizes the cell-envelope protein [161,175]. The H₂O₂ generated in Eq. (24) participates in reactions of the type shown in Eq. (22), but cells have enzymes to keep H₂O₂ at a very low level. Studies on antimicrobial Cu-surfaces involving mechanistic aspects have been compiled recently [209]. Fenton-like reactions in biological and microbial environments have been reported [210–215]. The lipid peroxidation linked to Cu-toxicity has been described recently by Lemire et al. [161]. A simplified representation of the Cu-induced cellular toxicity is suggested in Fig. 13.

Recently, a study by Miyauchi et al., reported Cu(II)-rutile undergoing hydrophobic-hydrophilic conversion under visible light up to 90% within a few hours. However, TiO₂-rutile by itself was only able to degrade 20% of the initial oleic acid under similar experimental conditions [216]. Fig. 14 shows the beneficial effect of the Cu-doping of TiO₂ enhancing the effects of the photo-generated charges in TiO₂ under light and accelerating the super-hydrophilic conversion. Rtimi et al., reported TiO₂ sputtered polyethylene (PE-TiO₂) undergoing hydrophobic to super-hydrophilic conversion under light within 60 min [217]. This time was similar to the one needed for the inactivation of *E. coli* under the same light dose. A recent publication [218] reported TiO₂ films sputtered on polymers/textiles leading to bacterial inactivation within the time needed to attain TiO₂ super-hydrophilicity or beyond this time. This gives rise to the possibility that some reaction(s) on the polymer surface lead to a delayed bacterial inactivation occurring after the time needed for the film hydrophobic to hydrophilic conversion [218]. The dye methylene blue (MB) [219,227] was degraded within 120 min on PE-films needing 60 min to attain super-hydrophilicity. The effect of Cu in ppm amounts decorating semiconductor films and leading to bacterial inactivation will be addressed next in Section 2.5.

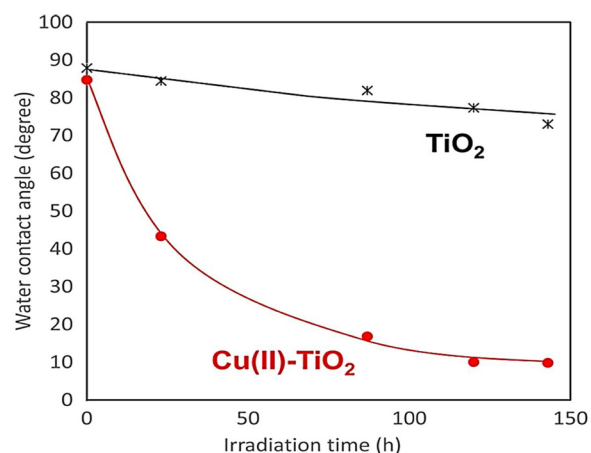


Fig. 14. Evolution in time of the super-hydrophilicity induced by visible light irradiation of a Cu(II)-TiO₂ grafted film where the TiO₂ was prepared by sol-gel. Reproduced from Reference [216].

2.5. Features of antimicrobial Cu-decorated surfaces under light and in the dark

2.5.1. Mechanism and kinetics in aerobic media

Decorating inorganic semiconductor-oxides such as TiO₂ with metals like Ag and Cu leads to a significant acceleration in the bacterial inactivation kinetics. Decoration means adding few amounts of any selected metal on the semiconductor surface. The decoration of the TiO₂-ZrO₂ binary semiconductor oxides by Cu in ppm amounts has recently been reported to enhance the bacterial inactivation [220]. This study reports the TiO₂-ZrO₂ sputtering on PES followed by the sputtering of Cu for 5 or 10 s introduced Cu in amounts < 0.01% that is at ppm levels. The bacterial inactivation proceeded within 120 min on the TiO₂-ZrO₂ films. This inactivation time was reduced by a factor of two by the addition of ppm amounts of Cu. The band-gap of the samples was determined from the diffuse reflectance spectroscopy (DRS) by Tauc's method [221] plotting the optical absorption in Kubelka-Munk units *vs* the spectral energy (eV). The band-gap found for TiO₂-ZrO₂ was determined by the tangential straight-line extrapolations in the Kubelka-Munk plots. The TiO₂-ZrO₂ band-gap was narrower compared to the values reported for the TiO₂ and ZrO₂ of 3.2 eV and 4.5 eV, respectively [222]. Optical spectra are commonly analyzed by the Tauc's method. Semiconductors present both direct and indirect inter-band transitions. The direct band gap is common on thin films, whereas indirect band-

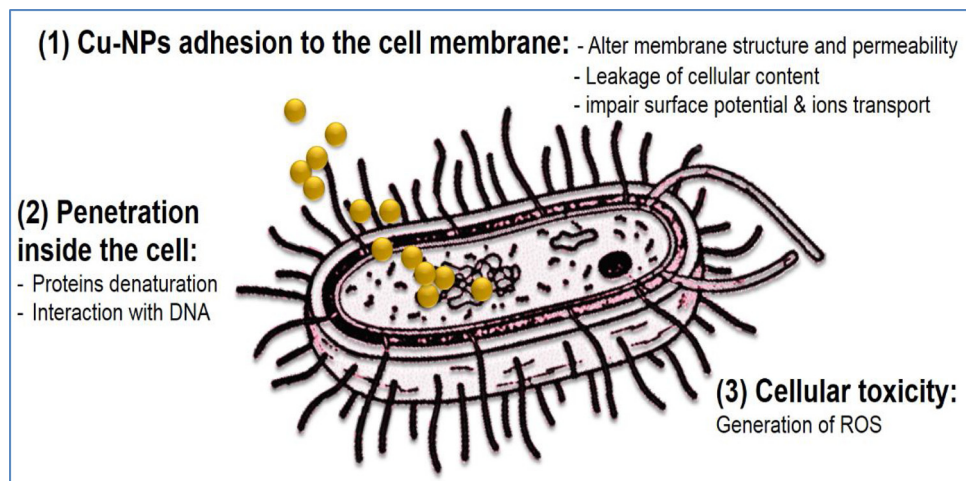


Fig. 13. Scheme showing the mechanism of Cu-induced bacterial cytotoxicity processes. Schematic illustration made use of some motifolio templates (www.motifolio.com).

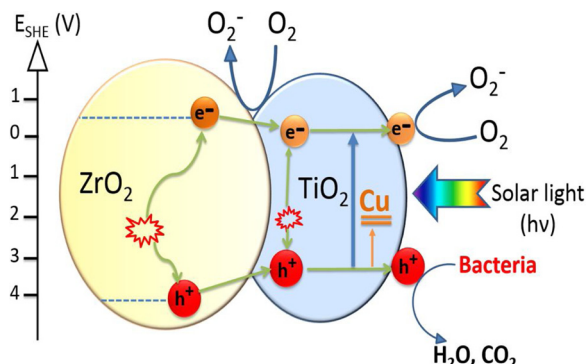


Fig. 15. Interfacial charge transfer on $\text{TiO}_2\text{-ZrO}_2$ PES sample co-sputtered for 8 min and $\text{TiO}_2\text{-ZrO}_2\text{/Cu}$ PES co-sputtered for 8 min/10 s under low intensity solar light (50 mW/cm^2).

gap transitions are generally found for relatively thick films. For indirect transitions, the Tauc's relations can be written as:

$$\alpha = \frac{B}{h\nu} (h\nu - E_g)^2$$

Where: B is the Tauc constant, $h\nu$ is related to the photon energy, E_g is the optical band-gap of the material, α is the absorption coefficient extracted from the transmittance (T) and reflectance (R) measurements for the sample using the equation:

$$\alpha = \frac{1}{d} \ln \frac{T_0(1 - R_s)}{T_s}$$

Where: d is the thickness of the film; Q and S refer to quartz or the sample, respectively. Tauc's treatment of the data holds for $\alpha > 10^4 \text{ cm}^{-1}$.

The indirect transition is obtained by plotting $(\alpha \times h\nu)^{1/2}$ versus $h\nu$, E_g corresponds to the intercept of the linear fit with the abscissa. The direct transition is obtained by plotting $(\alpha \times h\nu)^2$ versus $h\nu$.

Fig. 15 shows the interfacial charge transfer (IFCT) mechanism for $\text{TiO}_2\text{-ZrO}_2$ and Cu- decorated $\text{TiO}_2\text{-ZrO}_2$. It can be suggested that the $\text{TiO}_2\text{-ZrO}_2\text{/Cu}$ presents more O_2 reduction sites compared to $\text{TiO}_2\text{-ZrO}_2$. The Cu intra-gap level in the TiO_2 in Fig. 15 has been estimated from theoretical analysis [223,224]. The transfer of charge mechanism in Fig. 15 follows the band model (band positions) of the conduction and valence bands. The Cu acts as an intra-gap site precluding charge recombination. The $\text{Cu}^{1+/2+}$ sites can also intervene as electron acceptors enhancing the bacterial inactivation kinetics. The one electron oxygen reduction is shown in Fig. 15 and involves the following reactions:



and is followed by the generation of the primary $\text{HO}_2\cdot$ radical



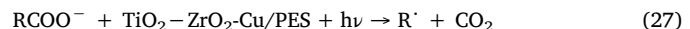
The Cu^{+} -ion reduces O_2 consuming electrons or is oxidized to Cu^{2+} by the TiO_2 holes [180].

2.5.2. Mechanism of bacterial inactivation/mineralization in aerobic/anaerobic media

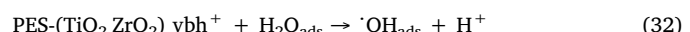
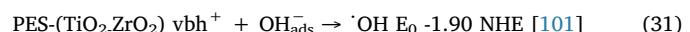
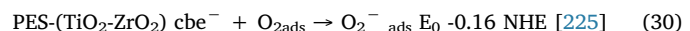
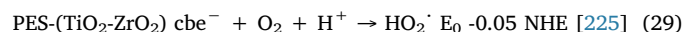
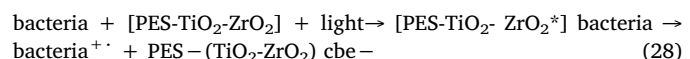
Recently, anaerobic reactions leading to cell damages have been reported to be comparable to the inactivation occurring under aerobic conditions [160,161,226]. Binary oxides such as $\text{TiO}_2\text{-ZrO}_2$ and $\text{TiO}_2\text{-ZrO}_2\text{/Cu}$ sputtered on polyester (PES) were irradiated under low intensity solar light and led to bacterial inactivation in aerobic media and at a lower rate in anaerobic media [159]. However, bacterial mineralization was only observed by $\text{TiO}_2\text{-ZrO}_2\text{/Cu}$ in aerobic media. The hole generated on the $\text{TiO}_2\text{-ZrO}_2$ films was the main species leading to bacterial inactivation and was identified by scavenging with EDTA-2Na, an effective hole-scavenger. Repetitive bacterial inactivation was

obtained by $\text{TiO}_2\text{-ZrO}_2\text{/Cu}$ showing the stability of these films.

Local pH and interfacial potential changes during bacterial inactivation were carried out in the dark and under light. Changes in the surface potential during the bacterial inactivation process increased the cell wall-permeability due to the loss of the cell envelope integrity. The $\text{TiO}_2\text{-ZrO}_2\text{/Cu}$ /PES interfacial potential and pH changes observed in the dark were less marked compared to the changes observed under light. The pH changes were due to the generation of short chain carboxylic acids (branched or not) with pK_a values around ~ 3 during the time of bacterial inactivation. In the later stages of the reaction, the pH recovered up to the initial pH ~ 6 due to the mineralization of the intermediate acids to CO_2 [228]. The CO_2 generation under light in aerobic media, is a typical photo-Kolbe CO_2 elimination reaction [228]:



Changes of pH concomitant to the interfacial potential changes shifted the pH surrounding the bacteria away of the natural physiological range 6–8 contributes and thus contributing to the bacterial inactivation. The bacterial inactivation was due to the damages in the cell wall envelope regulating the ions exchange in and out of the cell [229]. This increases bacterial cell wall permeability damage leading to cell death. The $\text{TiO}_2\text{-ZrO}_2$ under band-gap irradiation gives rise to an unstable short-lived bacterial cationic species as shown in Eq. (28) below followed by the reactions in Eqs. (29)–(33) leading to ROS generation and bacterial inactivation:



In a separate study $\text{TiO}_2\text{/Cu}$ was sputtered on PES and the intermediate radicals leading to bacterial inactivation identified in aerobic/anaerobic media [230]. By the use of appropriate scavengers, oxidative radicals like $\cdot\text{OH}$ / $\text{HO}_2\cdot$ and holes were identified in solution in aerobic media. However, no oxidative radicals were found under anaerobic conditions as shown in Fig. 16.

2.6. Effects of the Cu/TiO_2 films microstructure on bacterial inactivation kinetics

2.6.1. Targeted design of the photocatalyst microstructures

There is a need to find innovative more advanced films presenting

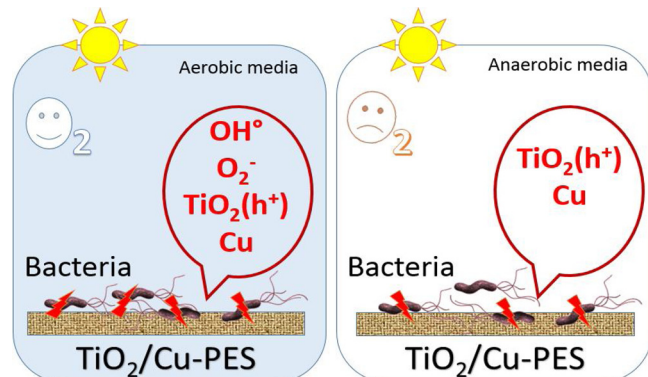
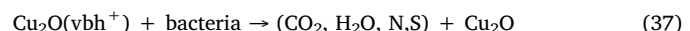
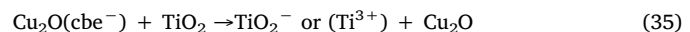
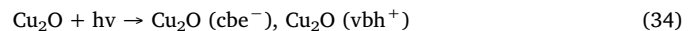


Fig. 16. Intermediate species and radicals generated on $\text{TiO}_2\text{/Cu-PES}$ films leading to bacterial inactivation in anaerobic and aerobic media [230].

accelerated (quasi-instantaneous) bacterial inactivation kinetics and at the same time being stable and adhesive to the substrate. Simultaneous deposition from two targets (co-sputtering) each being made up by a different metal has been used to deposit composite metal/oxide coatings for diverse applications. This is followed by the optimization of the sputtering parameters in the magnetron chamber to attain composites leading to the fastest antibacterial kinetics [231]. Two different microstructures of Cu-sputtered Ti-oxides on polyethylene (PE transparent 0.1 mm thick) with a similar atomic composition were observed to induce different bacterial inactivation kinetics [231]. Co-sputtered CuO_x/TiO₂-PET films were obtained by sputtering simultaneously Cu and Ti in an Ar/O₂ atmosphere. This leads to the formation of films with mainly CuO in the upper layers of about 10 nm as determined by XPS. The co-sputtered films led to bacterial inactivation within 20 min under low intensity actinic light (0.5 mW/cm²). The sequential sputtered CuO_x/TiO₂-PET samples were obtained by sputtering of Ti followed by Cu. These films presented mainly Cu₂O in the top-most upper layers leading to bacterial inactivation within 90 min. Fluorescence microscopy was carried out to monitor the bacterial inactivation on the co-sputtered CuO_x/TiO₂-PET. Fig. 17 shows the fluorescence microscopy of the *E. coli* where the green color stains correspond to living *E. coli* cells. Fig. 17 shows the red color fluoro-chrome stained dead cells developed when the *E. coli* biofilm was contacted with the CuO_x/TiO₂-PET sample. The density of the red dots increased progressively after 10 and 20 min contact with the sample. By atomic force microscopy (AFM), the roughness (Rg) of the co-sputtered (CuO) and sequentially sputtered samples (Cu₂O) were found to be respectively 1.63 nm and 22.92 nm [231,199]. Roughness is a measure of the vertical deviations of the valleys and peaks from an ideal flat surface. The CuO_x/TiO₂-PET with an Rg value of 22.92 nm reflects a high frequency of peaks positioned at short distances between each other allowing multiple contact points with the bacteria. These contact points allow the charge transfer between the *E. coli* bacteria ellipsoid in shape (1 μm) and the CuO_x/TiO₂-PET surface. The sequentially sputtered CuO_x/TiO₂-PET films with (Rg) 1.63 nm present contact points further apart from each other. Due to this, less sites/bridges are available for the redox exchange between the sputtered film surface and the bacterial cell envelope. This is one of the factors leading to slower bacterial inactivation kinetics. The increase in roughness favors the attachment of bacteria to a surface. This phenomenon cannot be extrapolated to surfaces leading to the oxidation of pollutants [132,218].

2.6.2. IFCT mechanism on samples with a similar composition but with a different microstructure

The bacterial inactivation on co-sputtered CuO_x/TiO₂-PET and sequentially sputtered CuO_x/TiO₂-PET samples is shown in Fig. 18a and b. CuO was found mainly in the upper layers of the co-sputtered samples. The sequentially CuO_x/TiO₂-PET catalyst presented mainly Cu₂O in the upper layers. The photocatalytic mechanism of TiO₂ leading to bacterial inactivation has been widely reviewed and will not be addressed here in detail [102,137]. The mechanism for the sequential sputtered films is suggested below in Eqs. (34)–(37) and involved mainly Cu₂O. The attack by Cu₂Ovh⁺ leads to the oxidation of bacteria as noted in Eq. (34) and the thermodynamically favorable electron transfer from Cu₂Ocb to the TiO₂cb in Fig. 18b is noted in Eq. (35):



2.7. Protection of the Cu-ion release in sputtered films increases the sample stability

The Cu use as antimicrobial agent is based on the high Cu-cytotoxicity per unit weight presenting concomitantly an acceptable biocompatibility with mammalian cells. Excessive Cu leaching during the bacterial inactivation has been a source of concern for applications in health-care facilities since they are strongly detrimental to metabolic processes in the human body. Fig. 19 presents the data for the Cu-leaching out of TiO₂/Cu sequentially sputtered films up to the 8th cycle [232]. Fig. 19 (trace 4) shows that the 10 min TiO₂ sputtered samples deposit a TiO₂ coating protecting Cu-release. The amounts of Cu released in Fig. 19 are within the limits permitted by sanitary regulations [233,234]. The concomitant Ti-release during bacterial inactivation in Fig. 19 varied between 4–8 ppb. This is a very low level and consistent with the high chemical stability of TiO₂. The observed level for the TiO₂ released was seen to be much lower than 1.3 mg/l set by the US Environmental Protection Agency [235–237].

2.8. Inactivation of Gram-positive methicillin resistant *staphylococcus aureus* (MRSA) and other pathogens on Cu-surfaces

Many metals are toxic to almost all type of bacteria at

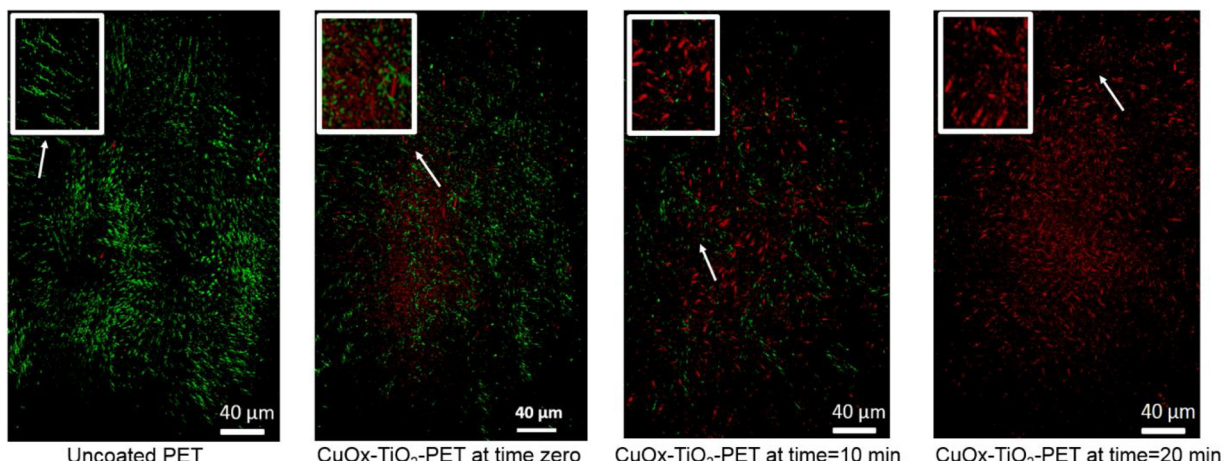


Fig. 17. Fluorescence stereomicroscopy of *E. coli* under low intensity actinic light showing the biofilm on: PET (time zero) CuO_x/TiO₂-PET time zero (dark reaction), and for CuO_x/TiO₂-PET co-sputtered samples after 10 and after 20 min irradiated under 0.5 mW/cm² actinic light. Green-dots refer to living cells and red-dots refer to dead cells. Reprinted with permission of S. Rtimi, et al., (2017). Other details are given in the respective reference [231] (For interpretation of the references to colour in this figure legend, the reader is referred to the web version of this article).

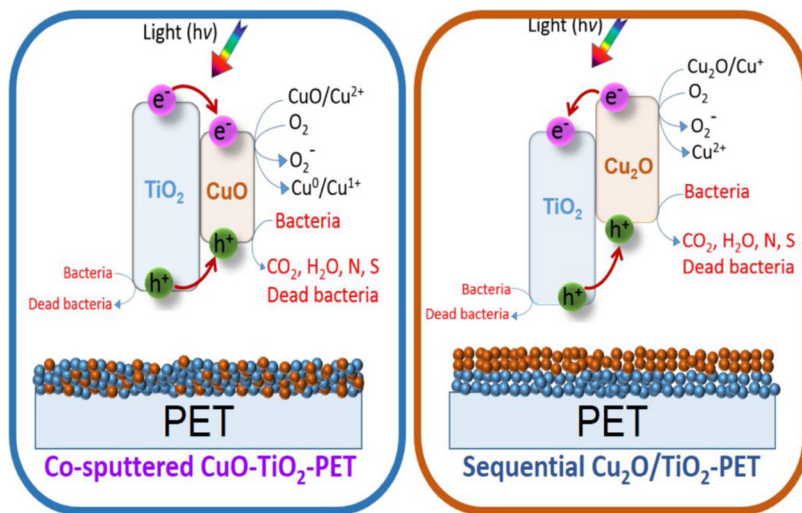


Fig. 18. a) Mechanism suggested for the antibacterial activity of co-sputtered CuO-TiO₂-PET on *E. coli*, and b) Mechanism suggested for antibacterial activity of sequentially sputtered Cu₂O/TiO₂-PET. Reprinted with permission of S. Rtimi, et al., (2017). Other details are given in the respective reference [231].

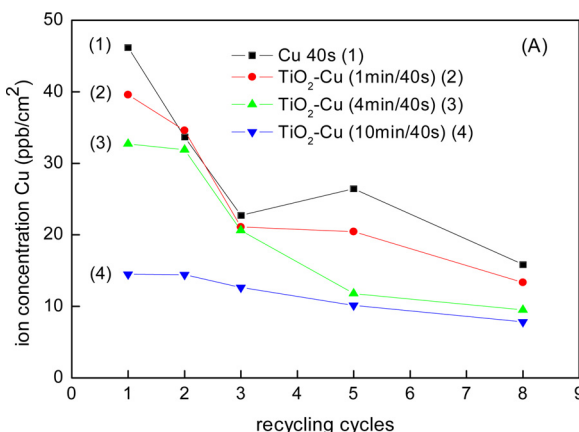


Fig. 19. Cu-ions release from diverse Cu- and TiO₂/Cu sequentially sputtered samples as a function of catalyst re-cycling up to the 8th cycle. Reprinted with permission of O. Baghriche, et al., (2012). Other details are given in the respective reference [232].

concentrations above the ppb range [199]. Because bacterial and eukaryotic cells have a variety of metal/ions transport systems, these cells can selectively discriminate in their reactions with specific ions/metals/oxides [160,161]. The *Staphylococcus*-type of pathogens in addition to *Pseudomonas aeruginosa* account for more than half of the deaths by hospital acquired infections (HAIs) killing 5–10% of hospital treated patients [18–21]. During the last decade studies have been directed on the use of Cu to reduce infections due to *Staphylococci* as described in the studies reported by Weaver et al. [238], Liu et al. [239], Nakano et al. [240], Kuhn et al. [241], von Kriegen et al. [242], and Pham et al. [243]. Gram-positive bacteria present walls with thicknesses 20–80 nm. The gram-positive bacteria present generally a thick peptidoglycan barrier compared to gram-negative bacteria. The peptidoglycan component makes up 50% of the thickness containing lipid/protein up to 4%. The Gram-negative cell envelope present thicknesses of about 10 nm and are made up by 10–20% peptidoglycan, 60% lipid/lipoprotein and 10–15% lipopolysaccharide. During the bacterial disinfection processes proceed once this barrier is damaged and made permeable by Cu-NPs/Cu-ions, the controlling effect on the ions entering and leaving the cytoplasm barrier disappears. In some cases, the Gram-

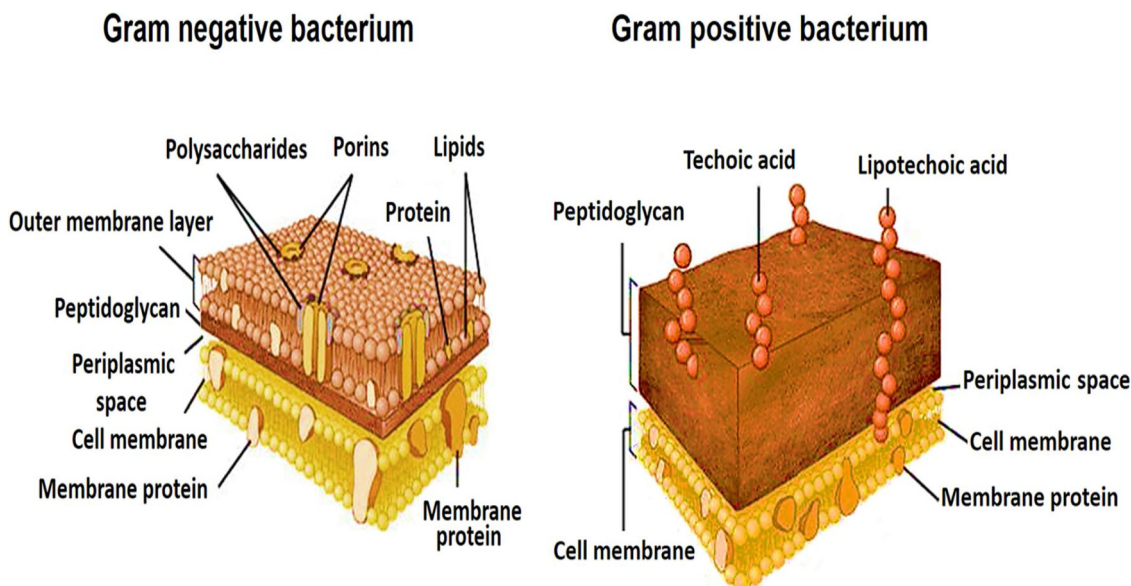


Fig. 20. Ultrastructure of the bacterial cell wall: a) Gram-negative bacteria and b) Gram-positive bacteria. (www.microbiologyinfo.com).

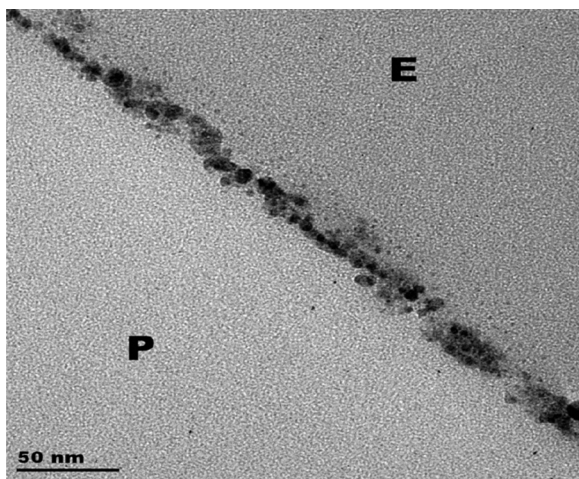


Fig. 21. Transmission electron microscopy (TEM) of Cu-sputtered polyester showing Cu-nanoparticle of 8–15 nm. Reprinted with permission of S. Rtimi, et al., (2015). Other details are given in the respective reference [24].

negative bacteria cell wall envelope was found to be more resistant to antibacterial agents due to the synergism and interlocking of the three layers making up the cell wall. Both type of bacterial structures are presented in Fig. 20a and b.

DCMS Cu-deposition for 160 s led to the formation of Cu-particles 8–15 nm in size forming a continuous layer on the polyester (PES) substrate [244]. This is shown by electron microscopy (TEM) in Fig. 21. These fabrics were inoculated with 10^6 CFU of MRSA and incubated for 1 h, 2 h and 3 h. The viability of MRSA was monitored by the direct-transfer-on-plate method. A $4\log_{10}$ reduction of the initial inoculum within 1 h was attained on the sputtered fabrics under light irradiation (experimental data not shown). A recent study described the accelerated inactivation of MRSA on Cu-CuO/TiO₂-PES in the dark. The samples of MRSA were prepared with an initial concentration 10^5 – 10^6 CFU/mL [245]. Unexpectedly, the MRSA inactivation on Cu-CuO/TiO₂-PES was not accelerated under indoor light irradiation (4.65 mW/cm^2) when compared with the bacterial inactivation time observed under dark conditions. This suggests that the Cu-ions/radicals in the dark produced by the CuO lead to MRSA inactivation without a meaningful intervention of the radicals generated under light. Recent studies have shown an effective antimicrobial and antifungal activity mediated by Cu-fabrics and catheters under indoor light or in dark conditions [244–249]. Cu-PES fabrics were recently shown to inactivate *C. albicans* and *C. glabrata*. This inactivation was accelerated under low intensity indoor/visible light ($> 400 \text{ nm}$) compared to dark experiment [248]. The surface-contact between the Cu-PES and the cell membrane has been shown to be the major mechanism for this fungicidal activity of the Cu-PES catalyst. Before contact between the Cu-PES and the fungi, the majority of Cu exists as Cu₂O. After contact with the microorganisms, a significant oxidation of Cu₂O to CuO was detected by XPS [248].

2.9. Cu-sputtered surfaces: Implications of the applied deposition energy

2.9.1. High power impulse magnetron sputtering (HIPIMS) of 2D-surfaces and 3D-medical catheters

The HIPIMS deposited films present a progress compared to the films sputtered by more traditional approaches and at lower energies such as DCMS and DCPMS. HIPIMS employs higher energies and generates a bigger amount of electrons/cubic meter ($\text{e-}/\text{m}^3$) in the magnetron chamber compared to DCMS and DCPMS. The HIPIMS higher energies induce a higher degree of ionization percentage of Ag and Cu in the magnetron chamber. The ionization potential of Cu⁺ is 7.7 eV. HIPIMS has been shown in some cases to lead to a smaller number of film defects, voids and a higher degree of densification of the sputtered

film [89–93,125]. During the last decade, some developments have been implemented in the magnetron sputtering deposition in response to the growing demand for high quality anticorrosive films in aircraft parts, in the car industry and in other industrial tools. Future developments need to focus on the increase of the wear resistance, tool lifetime and resistance to oxidation in surgery instruments and pacemakers by HIPIMS coatings. For Cu-surfaces, DCMS-sputtering attains a Cu ionization < 5% and an electronic density of $\sim 10^{14} \text{ e-}/\text{m}^3$ in the magnetron chamber. DCPMS-sputtering can attain an electronic density of $\sim 10^{16} \text{ e-}/\text{m}^3$ and a Cu-ionization 10%. In the case of HIPIMS, pulses from one microsecond up to milliseconds generate current densities of $\sim 10^{18} \text{ e-}/\text{m}^3$ and attain a Cu-ionization of 70% [250]. Recently, Bandorf et al. [155] measured the percentage of ionization of Cu-ions in the gas/plasma phase generated during the DCMS deposition. Values of: 87% Ar⁺, 5% Ar²⁺ and 8% Cu⁺ were found. The amount of Cu⁺-ions produced by HIPIMS at 6 Amps was 97% along 3% Ar²⁺. At 60 Amps, the HIPIMS generated 17% Ar⁺, 3% Ar²⁺, 75% Cu⁺ and 5% Cu²⁺. In the magnetron sputtering chamber, the primary ionization of the Argon gas: $\text{Ar} \leftrightarrow \text{Ar}^+ + \text{e}^-$ leads subsequently to the reaction: $\text{e}^- + \text{Cu}^0 \leftrightarrow \text{Cu}^+ + 2\text{e}^-$. In the case of HIPIMS, the higher amounts of Cu-ions interact more readily with the polyester substrate set at a higher bias-potential compared to the case of DCMS sputtering leading to more compact coatings (Fig. 22).

2.9.2. DCPMS and HIPIMS sputtering of Cu-polyester samples

Fig. 22 presents the *E. coli* loss of viability time vs thickness for DCMS/DCPMS and HIPIMS sputtered TiO₂/Cu films [196]. HIPIMS coated samples required a thinner TiO₂/Cu layer thickness for bacterial inactivation compared to DSMS/DCPMS. The HIPIMS film with a thickness of 38 nm inactivated bacteria within ~ 10 min while DCMS/DCPMS films 600 nm thick induced bacterial inactivation within similar times.

Fig. 23 presents in the left-hand side the DCMS sputtering inducing Cu-ionization < 5% [250]. The DCPMS in the middle section shows schematically ionization of Cu-ions ion the order of 10% [89,251]. Fig. 23, right-hand side shows the denser HIPIMS induced sputtering Cu-ionization of ca. 70% ($\sim 10^{18-19} \text{ e-}/\text{m}^3$). Higher energetic Cu-ions allow an increased alignment and density of the Cu-ions on the polyester sometimes concomitant with the reduction of the surface-roughness. The polyester 2D-surface roughness could not be quantified by atomic force microscopy (AFM) since it was beyond the AFM range of measurements of 10 microns.

Table 3 presents the data for the inactivation time of bacteria and fungi, the type of Cu, Cu/TiO₂ NPs and surfaces and the NPs sizes reported recently in the open literature. The data in Table 3 do not allow for a quantitative comparison for the work carried out in different laboratories since these studies were carried under different experimental conditions. However, the data are useful for a qualitative comparison of

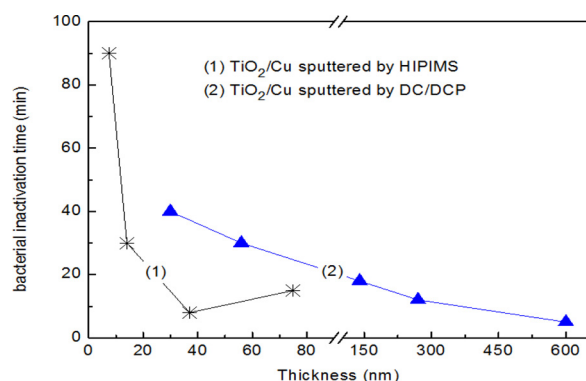


Fig. 22. Bacterial inactivation time vs nominal thicknesses for HIPIMS sputtered TiO₂/Cu films and by DCMS/DCPMS sputtered layers under solar simulated irradiation. Reprinted with permission of S. Rtimi, et al., (2013). Other details are given in the respective reference [196].

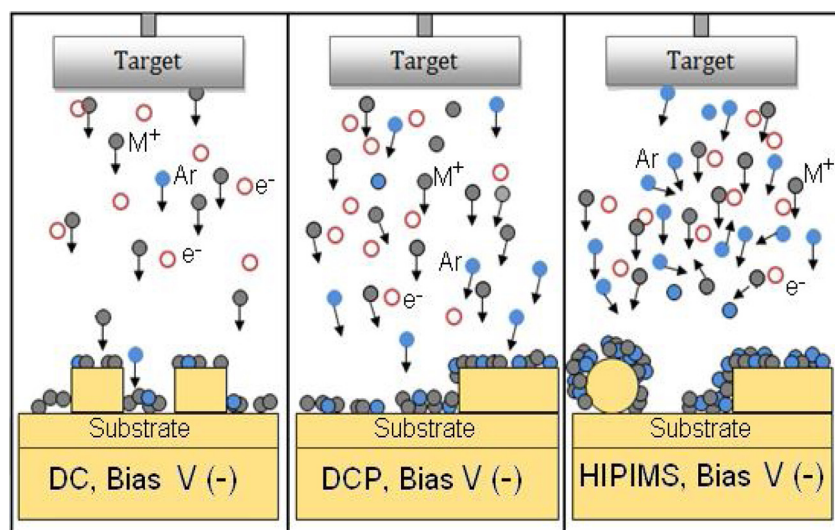


Fig. 23. Scheme for the magnetron chamber induced M^+ ionization by a) DCMS b) DCPMS and c) HIPIMS sputtering of metal-ions (M^+) on 3-D substrates showing the higher density ionization induced by HIPIMS. For other details, see text.

the bacterial/fungi inactivation kinetics mediated by diverse Cu-catalysts/photocatalysts.

Part 3: Cu-Ag Bimetal materials for bacterial inactivation

3. Introduction

3.1. Ag-Cu as antibacterial bimetal materials

3.1.1. Preliminary considerations on Ag-Cu suitable antimicrobial films

Metal oxides with antibacterial properties such as Ag, Cu, Zn, Ti and

Mn base their antibacterial activity on : a) the metal-ion diffusion and cell internalization through the porin channels into the bacterial cytoplasm, b) surface contact effects between the metal/metal-oxide and the bacteria envelope due to electrostatic attraction and magnetic interactions, c) the envelope modifications due to the shift in the physiological pH surrounding bacteria, d) changes in the interfacial potential during the bacterial inactivation time [145], and finally e) the destruction of the functional groups of the cell envelope as followed by infrared spectroscopy (ATR-IR) [252,253]. Cell contour modifications occur in *E. coli* leading to lysis/disaggregation during their interaction with TiO_2 -NPs, oxides, metals, double-oxides under light irradiation as recently

Table 3

Bacterial inactivation times of Gram-negative and Gram-positive bacteria on Cu, CuO_x and Cu/TiO_2 surfaces.

Authors	Microorganism	Catalyst/Photocatalyst	Inactivation time	Catalyst size / configuration	Ref.
S. Rtimi et al.,	<i>E. coli</i>	TiO_2-ZrO_2-Cu	30 min	Thin film	[159]
G. Borkow & J. Gabbay	<i>E. coli</i> , MRSA, <i>C. Albicans</i>	Cu-impregnated textile	60 min	0.1–0.2 microns	[164]
D. Quaranta et al.,	<i>C. Albicans</i>	Cu/CuO plate	30–60 min		[173]
Espirito-Santo et al.,	<i>E. coli</i>	Cu/CuO plate	150–180 min		[174]
Sunada et al.,	<i>E. coli</i>	Cu/TiO_2 films	4 h	Films	[177]
Qiu et al.,	<i>E. coli</i>	CuO_x/TiO_2	60 min		[178]
J. Elguindi et al.,	<i>P. aeruginosa</i>	Cu-surface	120 min	Surfaces	[179]
Noyce et al.,	MRSA, <i>C. Albicans</i>	Cu-surfaces	24–60 min	Surfaces	[180]
Noyce et al.,	<i>E. coli</i>	Copper-alloys	75 min	Alloys	[181]
N. Cady et al.,	<i>A. baumannii</i>	Cu-cotton	10 min	2–5 nm colloids	[185]
D. Sun et al.,	<i>S. aureus</i>	Stainless Steel-Cu	24 h	0.2–2 microns	[188]
O. Akhavan et al.,	<i>E. coli</i>	CuO_x/SiO_2	15–30 h	20 nm	[189]
S. Rtimi et al.,	<i>E. coli</i>	TiO_2-Cu HiPIMS	5–10 min	Thin films	[196]
		TiO_2-Cu DCMS			
S. Rtimi et al.,	<i>E. coli</i>	Cu-polyester:	20 min	Thin films	[198]
	MRSA	HIPIMS	120 min		
		DCMS			
Castro et al.,	<i>E. coli</i>	Cu-cotton DCMS	Under light: 30 min In the dark: 120 min	Thin films 50–200 nm	[200]
Osorio et al.,	<i>E. coli</i>	Cu-polyester DCPMS	30 min (under light)	Thin films 50–80 nm	[201]
E. Cubillo et al.,	<i>S. Aureus</i> , <i>E. coli</i>	Cu-sepiolite	24 h	15–30 nm	[204]
J. Musil	<i>E. coli</i>	Al-Cu-N	3 h		[206]
S. Rtimi et al.,	<i>E. coli</i>	TiO_2-ZrO_2-Cu	45 min under light	Thin films	[220]
S. Rtimi et al.,	<i>E. coli</i>	Cu/TiO_2	30 min	Thin film	[230]
S. Rtimi et al.,	<i>E. coli</i>	CuO_x-TiO_2 co-sputtered	20 min	Thin film	[231]
S. Rtimi et al.,	<i>E. coli</i>	CuO_x/TiO_2 sequentially sputtered	75 min	Thin film	[231]
L. Rio et al.,	MRSA	Cu-polyester	1 h	Thin film 10–15 nm	[244]
M. Ballo et al.,	MRSA	Cu-polyester	15–20 min	Thin films	[246]
	<i>S. epidermidis</i>				
	<i>P. aeruginosa</i>				
	<i>A. baumannii</i>				
M. Ballo et al.,	<i>C. glabrata</i>	Cu-polyester	30 min	Thin films	[248]

reported [254,199]. The advantages for Ag-Cu films over Ag- and Cu-films applied independently will be discussed in this section. The use of two highly oxidative metal/metal oxide nanoparticles such as Ag-Cu NPs amalgamated on the same film offers additional potential couples (or catalytic sites) compared to the *redox* couples of Ag and Cu by themselves. These additional potentials drive/catalyze/photocatalyze the surface microbial inactivation. A typical example is found in petroleum chemistry: the Ru/SiO₂ with the Ru presenting five different valences between +3 and +8. This provides the Ru/SiO₂ surface with several potentials. This is important in reactions for the catalytic cracking of fuels in the petroleum industry [255]. The *E. coli* negatively charged surface interaction with the positively charged metal-ions is due to the predominance of carboxylic groups over the positive Amide (I)/Amide (II) groups in the *E. coli* envelope. Photocatalytic processes leading to bacterial inactivation are favored by the increased light absorption of the Ag and Cu bands in the Ag-Cu films. This increases the molar absorption coefficient of the films in the visible range up to 700–800 nm [152,200]. In addition, CuO_x has been reported to be more effective in dark inactivation processes [256] compared to Ag₂O [21]. Dark processes have been reported to proceed through an oligodynamic effect. Synergistic effects when Ag and Cu are applied together in Ag-Cu antibacterial films involve the high Cu-cytotoxicity per unit weight and the biocidal activity of Ag-NPs as described in Sections 1 and 2 in this review.

3.1.2. Biofilm adhesion and film hydrophobic C-H hydrophilic properties

When microorganisms attach to a surface, they secrete extracellular biopolymers leading to the formation of biofilms. These biopolymers attach the bacterial colonies through polysaccharides and proteins [1–5]. Pathogenic biofilms act as a pump spreading bacteria/fungi/viruses into the environment and constitute the most dangerous type of infectious agents [7–9,199,116,245]. A special worrisome feature of the biofilms pumping bacteria and other pathogens into the environment is the long-span lifetime of these processes. During their lifetime, these biofilms take in nutrients from the surroundings and release byproducts after the biofilm formation ensuring their stability [134,160]. The adherence of bacteria to the surface is a feature controlling the transfer of charge between the surface and the bacteria. The surface adherence of the bacteria to the substrate is mainly a function of the hydrophobic-hydrophilic interaction between the surface and the bacterial envelope. Only a few negatively charged bacteria such as *E. coli* have been reported to adhere to negatively charged surfaces [161,214]. Both hydrophobic and hydrophilic bacteria can be found on any kind of surface in hospital facilities. Most of the polymers and artificial polyester (and combinations thereof) comprising 70% of the textiles reaching the market in Europe are hydrophobic in nature [257]. Bacteria with hydrophilic properties such as *S. aureus* have been reported to adhere to hydrophilic surfaces [258]. *S. epidermidis* adheres preferentially to hydrophobic surfaces [259]. The polyethylene (PE) thin polymer allows bacterial growth due to the relatively strong cell adhesion to the PE-surface and presents a real problem in commercially food wrapped PE-packages [260]. The adhesion of bacteria to PE is facilitated by the PE low surface energy [261].

Two approaches have been investigated to hinder the bacterial surface adhesion: a) addition of F- in the form of fluoropolymers to PE increasing the surface free energy [262] and b) increased adhesion of TiO₂/SiO₂ to the substrate compared to TiO₂ alone. [263,264]. TiO₂/SiO₂ surfaces have been reported to increase the surface area of TiO₂ layers. This favors the amount of photo-generated ROS reaching the bacteria.

This section addresses Ag-Cu films presenting almost instantaneous antibacterial kinetics intended to preclude the formation of toxic biofilms from the outset. The design, synthesis, inactivation kinetics and bacterial inactivation mechanism of Ag/Ag₂O-Cu/CuO_x films is addressed below. Polymer films and textiles loaded with highly oxidative

metal/metal ions have recently been found to be suitable candidates to reduce/preclude the formation of biofilms.

3.2. Colloidal loaded Ag-Cu NPs and films leading to bacterial inactivation

During the last years, colloids of Ag and Cu have been impregnated or ion-exchanged on many supports such as clays and zeolites. These colloids then diffuse into the support matrix. Sol-gel methods have been used during the last few decades to prepare bioactive Ag-Cu composite and sometimes coated on glasses. These gels are reacted thermally on non-heat resistant substrates at 50–90 °C or on glasses resisting higher temperatures. Reports on the preparation of Cu and Ag-nanoparticles and bimetal particles by sol-gel methods have recently increased. M-NPs deposition/adhesion on polymer/textiles is poor and the M-NPs films obtained are not mechanically stable, not reproducible and their distribution on the substrate is not uniform. It is not possible to heat the textile, polymer substrates to a few hundred °C to anneal the metal/oxides on non-heat resistant supports. To remedy these drawbacks M-NPs films are sputtered at temperatures in the range of 110–130 °C. Metal/bimetal and oxides sputtered on a wide variety of supports show: 1) uniform distribution, 2) good adhesion to the substrate, 3) large antibacterial spectrum, 4) only low amounts of metals are needed to inactivate bacteria, and 5) higher mechanical resistance than films prepared with other methods. These film properties lead to a stable and long operational lifetime for the sputtered films.

In some cases, the adhesion of Ag-Cu films needs to be improved to increase their mechanical resistance and stability when used in the disinfection of blood streams. This is possible by introducing an intermediate layer to increase the adherence of the topmost antibacterial film to the substrate. These under layers are made of: a) TiO₂ films [170], b) TiN and other nitrides presenting aligned flat surface microstructures [247,128], and c) hydroxylapatite (HA) porous films [266]. These layers, due to their porous network, increase the adhesion of the metal/oxide NPs to the substrate. The subsequent sputtering of CuO_x films enables the Cu-species to penetrate in the porous HA-network. The reduction in the leaching of the metal/oxide during the bacterial inactivation is essential for the: a) increase of the useful operational time of the sputtered films and b) stabilization of the film long-term cytotoxicity leading to bacterial inactivation.

The Ag-Cu film composition obtained by sol-gel showing antibacterial properties is listed below in Table 4. Table 4 reports the bacterial inactivation parameters by Ag-Cu materials. This is an important observation since the infection level in intensive care units by MRSA has recently reached > 50% [265–267]. Ag-Cu prepared by sol-gel methods have been deposited on diverse substrates. Mclean et al., reported MRSA inactivation on Ag-Cu /silicon rubber sputtered disks within 10–50 hours [268]. When only Ag was coated on the same disks, the bacterial inactivation required longer times. Slambarová et al., reported Ag-Cu-TiO₂ coatings from sol-gel suspensions able to reduce MRSA [269]. Antimicrobial suspensions of Ag-Cu have also been reported to inactivate bacteria in suspension [270]. Heffelfinger et al. [273] reports a partial destruction of Legionella by way of monochloramine in aqueous media in hospital bodies/effluents. This result motivated an interesting study by Stout et al. [274] reporting the inactivation of Legionella by Ag-Cu membranes leading to their disappearance up to 5 years. This study reported that the positively charged Ag and Cu-ions interact electrostatically with the negative cell wall of Legionella, leading to protein denaturation followed by lysis and cell death. Hsieh et al. [278] recently reported that co-sputtered TaN-Cu/Ag films inactivated bacteria much faster compared to either Ag-nitride or Cu-nitride films when applied separately. Description of recent work on Ag-Cu sputtered films leading to the inactivation of pathogens is described below.

Table 4

Size and inactivation times by Ag-Cu bimetallics (deposited or not) leading to the inactivation of diverse Gram-positive or Gram-negative bacteria.

Authors	Microorganism	Catalyst/Photocatalyst	Inactivation time	Catalyst size/configuration	Ref.
R. McLean et al., Slamborova et al., Ruparelia et al., G. Rao et al., A. Eremenko et al., J. Heffelfinger J. Stout and V. Lu H. Amir et al., M. Paszkiewicz Mironda-Rios et al., J. Hsieh	<i>S. aureus</i> MRSA MRSA <i>E. coli</i> <i>E. coli</i> Legionella Legionella <i>E. coli</i> <i>E. coli</i> / <i>C. Albicans</i> <i>E. coli</i> MRSA/ <i>E. coli</i>	Ag-Cu sputtered silicon rubber Methyl methacrylate Colloid Ag/Cu Cu-Ag-TiO ₂ membrane Cu-Ag impregnated cotton Nano-chloramine Cu-Ag salts Ag-Cu-PVA Ag, Cu NPs Ag ₂ O/Cu ₂ O TaN(Ag,Cu) on Si	10–50 h 100 nm 10 h 30 min 20–30 nm Days/partial reduction Days/full reduction 30 min 13 h	Thin film 1–2 microns 3–9 nm Membrane 20–30 nm Ag 48 nm/Cu 39 nm Ag 150 nm / Cu 250 nm	[268] [269] [270] [271] [272] [273] [274] [275] [276] [277] [278]

3.3. Ag-Cu films leading to bacterial inactivation with a quasi-instantaneous kinetics

The first evidence for Ag-Cu (50%/50%) sputtered films on polyurethane (PU) catheters leading to a quasi-instantaneous bacterial inactivation in the dark ≤ 5 min were recently reported [51,52]. Ag and Cu coated PU samples were also able to inactivate bacteria but within longer times up to ~ 30 min. Hydrophobic to hydrophilic transformation of the Cu-Ag PU-catheter surface under light was observed within the 30 min bacterial inactivation period. The release of Cu- and Ag-ions was followed by inductively coupled plasma mass-spectrometry (ICP-MS). The amounts of Cu and Ag-ions released were well below the cytotoxicity levels permitted by sanitary regulations. Fig. 24 show that the bacterial inactivation times became longer as the amount of Ag was increased in the Cu-Ag film.

Films made up of 50%/50% Ag-Cu were sputtered by DCMS for one minute in the magnetron chamber shown previously in Section 1, Fig. 4. Similar bacterial inactivation kinetics were observed under light irradiation or in the dark. Unexpectedly, this allows the conclusion that the cytotoxicity of the Ag₂O-CuO_x films and not the semiconductor nature of the Ag₂O-CuO_x film is the predominating effect leading to bacterial inactivation.

E. coli cells damage was monitored by stereomicroscopy on a 50%/50% Ag-Cu PU samples as indicated by red dots in Fig. 25. The fluorochrome dye stains the cell DNA of the damaged cells due to the abnormal high permeability of these damaged cells [279]. Fig. 25 shows that after 2 min, no living *E. coli* bacteria could be detected. The mechanism leading to the fast inactivation kinetics is due to the presence

of the Cu and Ag potential couples sputtered on the film mediating the bacterial inactivation will be discussed next in Section 3.4.

3.4. Mechanism suggested for the bacterial inactivation of Ag-Cu films

The acceleration of the bacterial inactivation kinetics induced by Ag-Cu-PU films is due to the film amalgamated Ag-Cu-PU layers. Due to the difference in their *redox* potentials, the Ag displaces Cu due to its position in the galvanic scale. The Ag-Cu films comprise the couples: Ag⁺/Ag⁺ -0.80 V SHE and Cu²⁺/Cu⁺ 0.15 V SHE. Therefore, the Ag-Cu galvanic cell reaction is driven by a potential of -0.65 V SHE [137]. In the Ag-Cu-PU film, Ag acts as the cathode and Cu as the anode. The contact between Ag and Cu increases the atomic disorder in the Ag-Cu amalgam [281,282]. The reaction between Ag and Cu leading to Cu- and Ag-ions release (corrosion) is noted in Eq. (38):



The determination of the amounts of Cu and Ag-ions was carried out by ICP-MS in a Finnigan™ ICPS unit equipped with a double focusing reverse geometry mass spectrometer. The washing solutions from the sputtered samples were digested with nitric acid 69% (1:1 HNO₃:H₂O) to remove the organics in solution and to guarantee that there were no remaining ions adhered to the flask wall. In this method, the sample droplets are introduced through a peristaltic pump to the nebulizer chamber at high temperatures. This allows the total sample components evaporation and ionization. The Cu and Ag-ions are soluble within the ppb range found for Ag and Cu during bacterial disinfection. The released ions lead to the bacterial inactivation observed in the dark. An oligodynamic effect was suggested for the intervention of the Ag-Cu nanoparticle films due to the ppb amounts released during the bacterial inactivation processes [51,168–170].

3.5. Surface potential and pH-changes during bacterial inactivation

The interfacial potential changes during bacterial inactivation of *E. coli* were monitored on Cu-Ag 50%/50% films in the dark. The values found are noted in the left-hand axis in Fig. 26a/b. The pH-shifts were also monitored as a function of time and are shown in right hand axis in Fig. 26a/b. The initial pH of 6.8 decreases to 6.4 within 5 min. This suggests the production of intermediate long-lived carboxylic acids with a pK_a \sim 3. After 200 s, the carboxylic acids decompose generating of CO₂ through a Kolbe type CO₂ elimination reaction [228]. Fig. 26b reporting the data for similar disinfection processes under light irradiation show a steeper decrease in the pH-values compared to the values in Fig. 26a. As shown in Fig. 26b, after the initial decrease, pH recovery within 15 min was observed up to the initial pH 7.0. This recovery is due to a photo-Kolbe type reaction shown in Eq. (39):



The decrease in the interfacial potential during bacterial

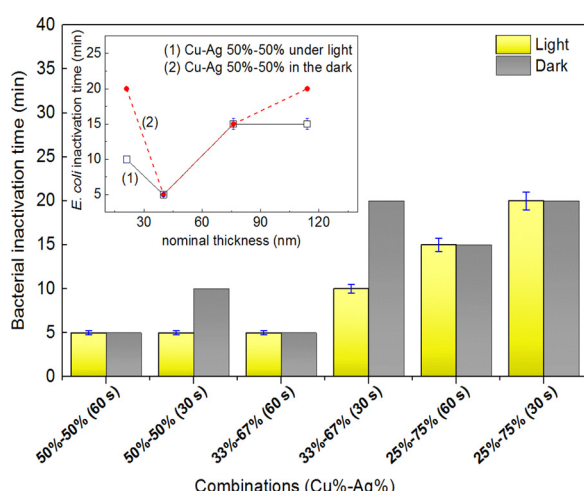


Fig. 24. *E. coli* inactivation on sputtered Cu-Ag PU the effect of the atomic ratio of Cu : Ag on the bacterial inactivation time under low intensity indoor actinic light (3 mW/cm²). Reprinted with permission of S. Rtimi, et al., (2016). Other details are given in the respective reference [51].

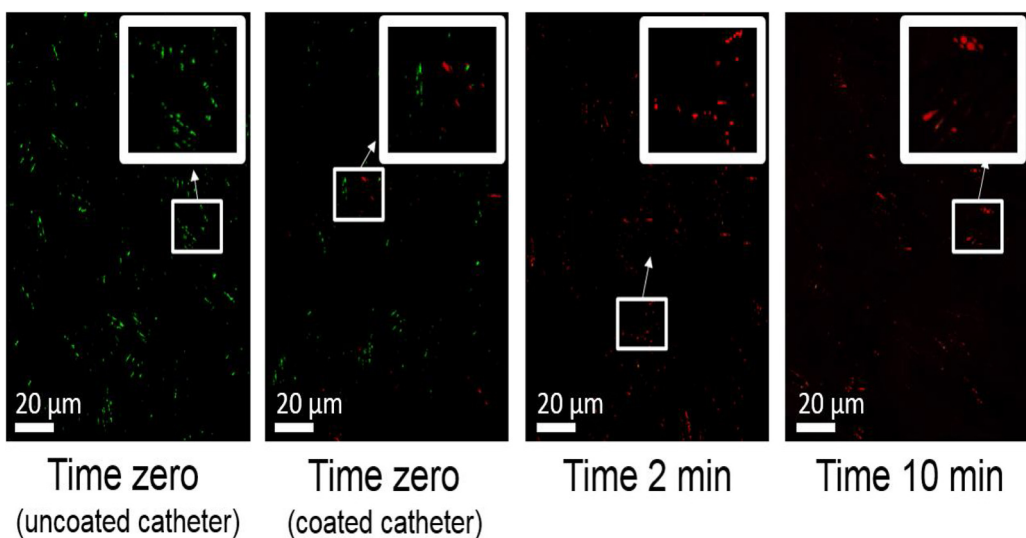


Fig. 25. Monitoring of the live/dead *E. coli* after 2 and 10 min in the dark on Cu-Ag (50%-50%). The images show uncoated catheters and sputtered catheters at times zero, 2 min and 10 min. Reprinted with permission of S. Rtimi, et al., (2016). Other details are given in the respective reference [196].

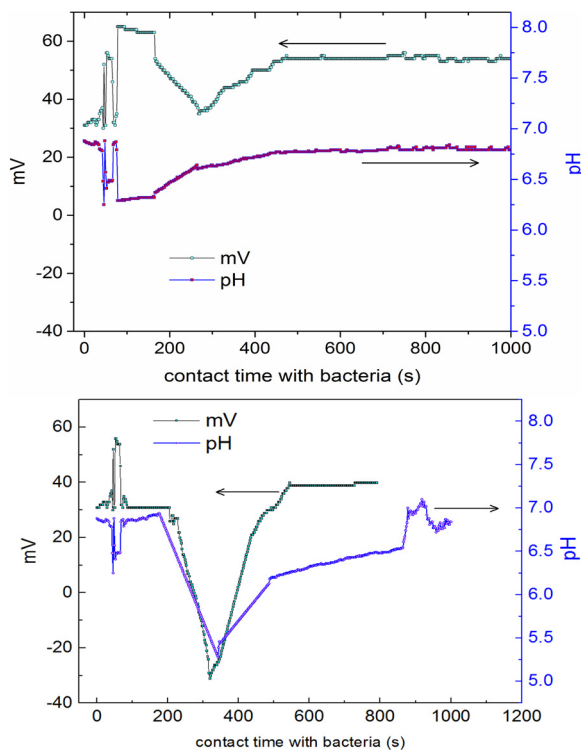


Fig. 26. a Interfacial potential and local pH shifts of the bacterial culture contacted with Cu-Ag 50%/50% on PU-catheter in the dark. b Interfacial potential and local pH of the bacterial culture contacted with Cu-Ag 50%/50% on PU-catheter under a 3 mW/cm² actinic light. Reprinted with permission of S. Rtimi, et al., (2016). Other details are given in the respective reference [51].

inactivation is attributed to the increase in the cell wall envelope permeability as the reaction times become longer. This implies for processes in the dark or under light irradiation. The interfacial potential flattens when the cell wall destruction is complete. An actinic light source was used in Fig. 26b. A decrease of $3\log_{10}$ for the *E. coli* CFU required a light dose of 1 mJ/cm^2 . In the case of MRSA a dose $2\text{--}4 \text{ mJ/cm}^2$ was necessary to achieve similar inactivation kinetics [279,280]. In Fig. 26a, the initial surface potential in the dark is seen at 65 mV. Fig. 26b shows an initial surface potential 18 mV for runs under light irradiation. The initial "Eigenvalues" refer to the intrinsic interfacial

potential characteristic of each film surface and reflect the surface make up, microstructure, surface tension, nanoparticle size and composition.

3.6. TEM imaging and XPS analysis of Ag-Cu films

Fig. 27 presents the Cu- and Ag-nanoparticle distribution on the PU-films by scanning transmission electron microscopy in (STEM) mode. The mapping of Cu and Ag in the Ag-Cu PU samples (with different Cu:Ag atomic ratios) was carried out to determine the atomic distribution in the sputtered films. The first row in Fig. 27 shows a uniform distribution of Cu nanoparticles with particle sizes of 2–4 nm. The second row shows the images for a Cu-Ag film made up by Cu 0.05% and Ag 0.03% by weight. The loadings of Cu and Ag have been determined by X-ray fluorescence (XRF). The third row shows the images for a Cu-Ag sample with a ratio 33%: 67%. Most of the Cu and Ag-metal clusters were < 5 nm in size. The small size of the nanoparticles favors the charge transfer due to large surface area per unit mass. The charge transfer between Cu and Ag in light activated reactions would be limited by the size of the grains in the thin layers without taking into account the variability of the inter-particle contact area. A size reduction in the space charge layer has been reported to decrease the electronic potential levels for metals [279–287]. The last row in the image shown in Fig. 27 shows that an increase in the percentage of Ag in the Cu-Ag films leads to the formation of bigger agglomerates. The second and third columns in Fig. 27 show the uniform distribution of the Cu and Ag nanoparticles proportional to the Ag-Cu present in the sputtered films. The nanoparticles are seen to be uniformly distributed on PU fabrics. The PU is an electronegative and hygroscopic material that rapidly attracts water. This is a beneficial feature in the release of Ag- and Cu-ions followed by the solubilization of these ions leading to bacterial disinfection.

Table 5 presents the Cu- and Ag-oxides on Ag-Cu films with different ratios of Cu: Ag. The content in Table 5 obtained by XPS shows: a) that metallic Cu exists as a metal only in the Cu-Ag (50%-50% sample) and plays an important role in the charge transfer from the film to the bacteria leading to fast bacterial inactivation, b) Ag₂O is absent in the Cu-Ag (50%-50%) sample. AgO was detected in these films being the most active Ag-oxide leading to *E. coli* inactivation. This confirms the results reported in a recent study [51,288], c) Ag⁰ metal is a necessary component in films with different Cu: Ag ratios and d) the Ag₂Cu₂O₄ composite is present in Cu-Ag (50%-50%) and Cu-Ag (33%-67%), the two most active samples. The Ag₂Cu₂O₄ would then play an important role in the charge transfer [289,290]. A scheme of the *E. coli*

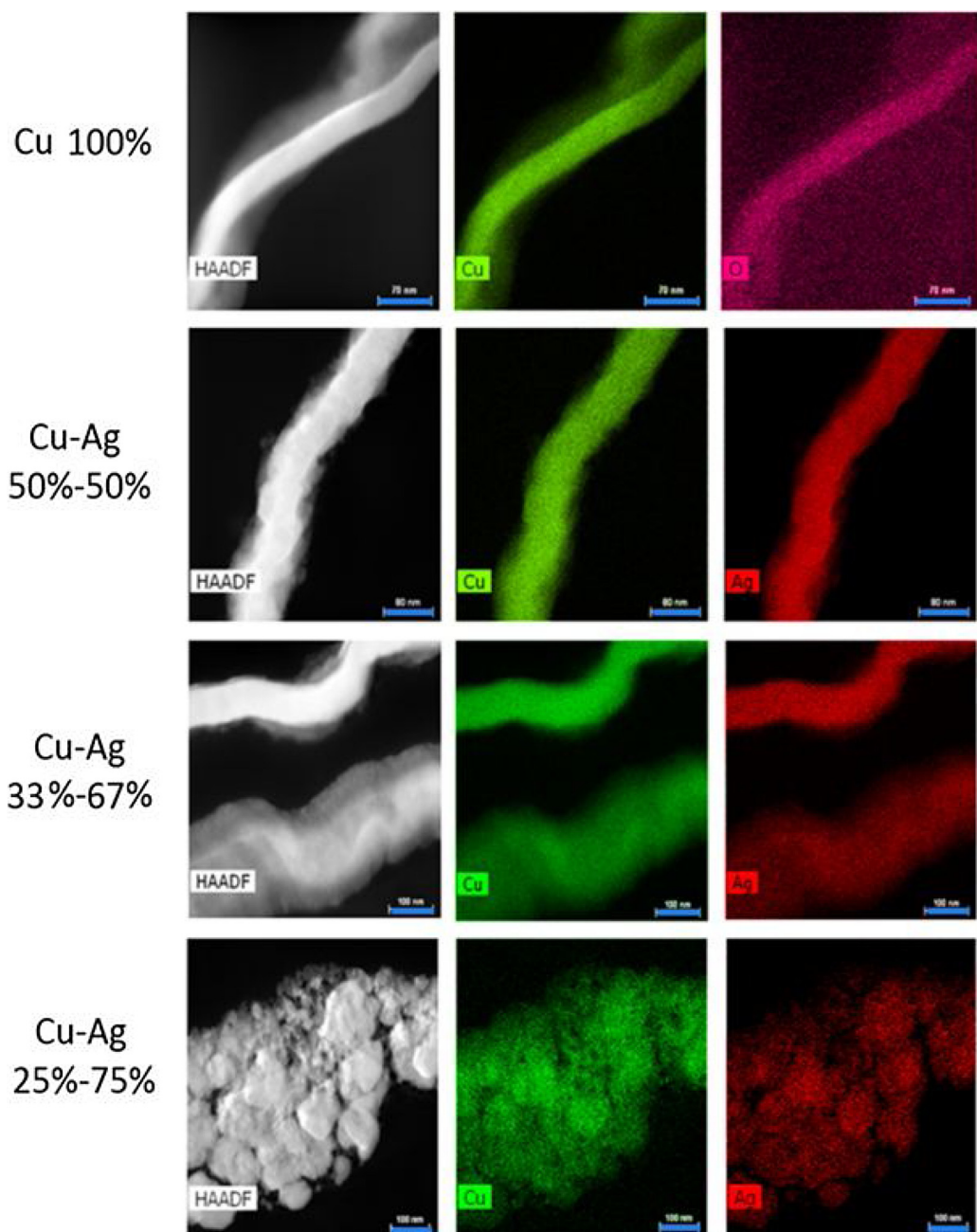


Fig. 27. EDX microanalysis/distribution of the Cu and Ag nanoparticles on the PU-films with different Cu: Ag atomic ratios. Reprinted with permission of S. Rtimi, et al., (2016). Other details are given in the respective reference [52].

Table 5
Cu and Ag species present of Cu-Ag films with different atomic ratios of Cu: Ag [292].

	Cu-Ag (50%-50%)	Cu-Ag (33%-67%)	Cu-Ag (25%-75%)
Cu species	CuO, Cu ₂ O, Cu	CuO, Cu ₂ O	CuO, Cu ₂ O
Ag species	AgO, Ag	AgO, Ag ₂ O, Ag	AgO, Ag ₂ O, Ag
Mixed phase	Ag ₂ Cu ₂ O ₄	Ag ₂ Cu ₂ O ₄	–

inactivation by the diverse Ag- and Cu-species reported in Table 5 is presented in Fig. 28 [291,292].

To estimate the band-gaps of the Cu, Ag and Cu-Ag, a Tauc's plot of $(F(R)\nu)^n$ against the x-axis (eV) was employed. The following values were found for the band-gaps: a) AgOx (1.52 eV); b) Cu: Ag 50%-50% (1.63 eV); c) Cu: Ag (33%-67%) (1.61 eV); d) Cu-Ag (25%-75%)

(1.76 eV) and finally e) CuO_x (1.83 eV). The Cu-Ag sample band-gaps get narrower in the presence of lower Ag-amounts in the Cu-Ag films. The values for the CuOx band-gap were in agreement with the values reported by Bard et al., by photo-electrochemical experiments [55].

3.7. *E. coli* and MRSA inactivation on Ag-Cu films: corrosion of the film during the bacteria/fungi inactivation

The corrosion releasing Cu-ions (Cu is the cathode) and Ag-ions is shown next in Table 6. Cu-ion levels reported in Table 6 with a content < 10 ppb do not induce cytotoxicity in the mammalian cells [169]. Runs in the dark led to bacterial inactivation at a slower rate compared to runs under actinic light [5,170,214].

Recently, Ag-Cu sputtered catheters were investigated for their efficacy in preventing methicillin-resistant *Staphylococcus aureus* (MRSA)

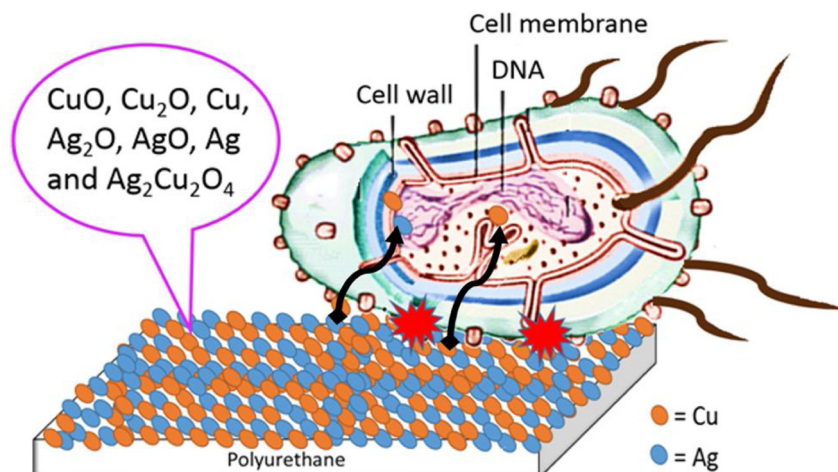


Fig. 28. Scheme indicating the active species leading to *E. coli* inactivation by a sputtered Ag-Cu (50%-50%) polyurethane surface. Other details are given in the respective reference [52].

Table 6

ICP-MS determination of Cu- and Ag-ions released in ppb units from Cu-Ag-PU sputtered films for 1 min.

Sample (4 cm ²)	Sample washed as prepared		Sample irradiated without bacteria		Sample irradiated with bacteria	
	Cu	Ag	Cu	Ag	Cu	Ag
Cu	28.5	–	14.2	–	10	–
Ag	–	12	–	9.4	–	4.2
Cu-Ag (25%-75%)	24.57	10.72	12.81	5.74	9	3.9
Cu-Ag (33%-67%)	15	8.8	10.4	5.7	10.8	4.4
Cu-Ag (50%-50%)	15.4	9.9	12.1	5.7	8.7	4.6

infection *in vitro* and *in vivo* [247]. *In vitro*, Ag-Cu-coated prevented MRSA infections from 79% to 57% compared with uncoated catheters and the incidence of bacteria was reduced from 68% to 31%. Scanning electron microscopy (SEM) of coated catheters suggests that the low activity of Ag-Cu catheters *in vivo* was due to a formation of a dense fibrin sheath over the film surface. The disinfection activity of Ag-Cu films was improved by limiting the plasma protein adsorption on the film surface. During these trials, animal samples were exposed to uncoated catheters and Ag-Cu-coated catheters and were inoculated with 10⁷ CFU of MRSA ATCC 43,300. Coatings of Ag on PU devices have been recently reported [288–292]. The antimicrobial properties of Ag sputtered or deposits from Ag colloids and moieties on polymer surfaces have been reported for some years [293,294].

3.8. Effect of the Ag, Cu and Ag-Cu films on normal and porinless *E. coli*. Differentiation of ionic and surface-contact effects

Fig. 29 presents the bactericidal inactivation times induced by sputtered samples of Cu, Ag and for Ag:Cu with different atomic ratios. Fig. 29a shows that Ag and Cu-films led bacteria inactivation within longer times compared with Ag-Cu composite films. Cu-samples required about 30 min and Ag about 60 min to induce complete bacterial inactivation. The Cu-Ag (33%-67%) and Ag-Cu (50%-50%) samples present the most suitable Cu- and Ag-loadings leading to the inactivation of the *E. coli* inoculum. No bacterial inactivation was observed when PU alone was irradiated under actinic light.

Fig. 29b presents the bacterial inactivation kinetics of genetically modified porinless *E. coli* and compared to normal *E. coli* strains provided with porins [291,292]. The porinless bacteria were prepared following procedures reported in the literature [293–296]. Quantitative determination of ionic effects induced by Ag-ions and Cu-ions diffusing through *E. coli* porins could in this way be compared to porinless *E. coli*.

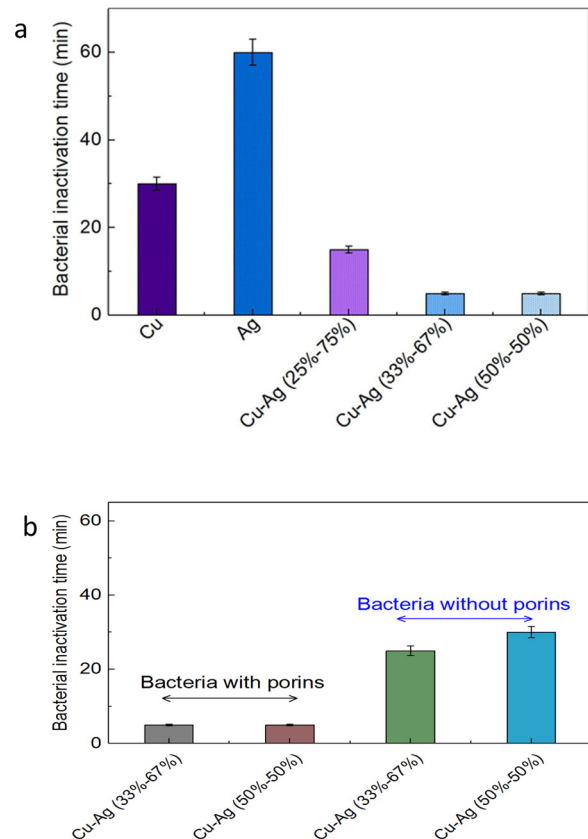


Fig. 29. a Bacterial inactivation of *E. coli* on sputtered PU-films (1 min) samples: Cu, Ag, and (25%: 75%) Cu: Ag (33%: 67%) Cu: Ag and (50%: 50%) Cu: Ag. Light source: Osram Luminlux 18 W/827 (360–700 nm range 3 mW/cm²). Other details are given in the respective reference [51]. b Bacterial inactivation on sputtered PU-films (1 min) by Cu: Ag (33%–67%) and Cu: Ag (50%: 50%). Cu-Ag-ions are seen to induce complete bacterial inactivation on normal *E. coli* when diffusing through the porins (d = 1.0–1.3 nm) within short times. Surface contact effects by Cu and Ag in porinless *E. coli* lead to bacterial inactivation within longer times. Initial *E. coli*: 1.4 × 10⁶ CFU/ml. Actinic light (3 mW/cm²). Reprinted with permission of S. Rtimi, et al., (2016). Other details are given in the respective reference [51].

Porinless bacteria do not allow the penetration of Ag and Cu-ions through the bacterial cell wall. Fig. 29b shows the inactivation of normal *E. coli* (with porins) within 4–8 min. This is six times longer the

time required for the inactivation of porinless bacteria. This is the evidence that Cu- and Ag-ions are not the only agents leading to bacterial inactivation but that surface-contact effects play an important role [292]. Sample irradiation was carried out under a low intensity actinic light emitting in the range 360–700 nm (3 mW/cm²).

The observed contact-surface leading to bacterial inactivation of porinless bacteria is due to: a) changes in the interfacial potential as shown in Fig. 26a/b, b) the shift of the pH surrounding bacteria away of pH 6–8 to values where the bacteria do not survive, c) destruction of the LPS layer functional groups as described below in Section 3.9 by ATR-FTIR spectroscopy and finally, d) the modification of the cell skeleton (*contour*) detected by electron microscopy, not shown hereby but observed for other systems [254]. Since the seminal paper on bacterial inactivation on TiO₂ by Matsunaga et al. [297] the mechanism of reaction has been worked out in many studies but is only partially known at the present time. No overall mechanism is available up to now. When seeking a faster bacterial inactivation kinetics, TiO₂-M and M–M or M–O systems are at present investigated and showing promising results [220,298]. The ionic effects of the Ag-Cu films leading to bacterial inactivation in Fig. 29b involve: a) Ag and Cu-ions diffusing through the *E. coli* 1.0–1.3 porins [141,142], b) bacterial inactivation by the sulfhydryl (-SH) groups in the cell envelope interacting with Ag and Cu-ions and c) metal bacteria interactions leading to bacterial damage and death [1–5,59,159–161,184,298].

3.9. Infrared spectroscopy of the functional groups abatement leading to bacterial lysis

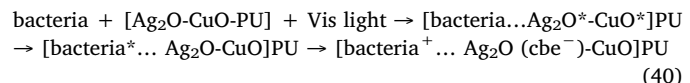
The progressive damage to the cell wall functional groups during bacterial abatement in the dark and under light irradiation was monitored by ATR-FTIR spectroscopy. The changes in the *E. coli* –CH₂-groups comprising > 70% of the C- in the *E. coli* were followed as a function of irradiation time. The ATR-FTIR spectra were normalized to compare the changes in the bands. The C–H band position in the FTIR spectra of the LPS layers allows to monitor the changes in the fatty-tail structure of the LPS in *E. coli* induced by the Ag-Cu films [299–301]. The *E. coli* cell wall consists of LPS units covalently linked containing -(CH₂) and -(CH₃) groups. These groups make up > 70% of the *E. coli* cell wall: LPS, peptidoglycan (PGN) and phosphatidyl-ethanolcholine. The peak positions of the -(CH₂) groups in the IR spectral region were found at 2800–3100 cm^{–1}. A blue shift of LPS 10–15 cm^{–1} during bacterial inactivation provides the evidence for the changes/disorder in the fatty tail structure preceding bacteria abatement. The increase in the LPS disorder leads to the enlargement of the intermolecular C–H bond distance leading to a higher LPS fluidity concomitant with the changes in conformation and packing [299]. The decrease in the initial *E. coli* concentration is a reflection of: a) the generation of peroxidation products during the bacterial inactivation and b) the modification of the LPS during the bacterial inactivation time. The concomitant reduction of Amide A was observed to occur faster than the *E. coli* inactivation.

3.10. Mechanism of the interfacial charge transfer (IFCT) during bacterial inactivation

A mechanism for the interfacial charge transfer (IFCT) between Ag₂O and CuO under light irradiation is suggested in Fig. 30. The mechanism of the charge generation by Ag₂O was addressed before in this review (see in Section 1.3.1 Eqs. (2)–(3) and in Section 1.4.1 Eqs. (5)–(13)). The mechanism of charge generation by CuO has been described in Eqs. (17)–(21) and Eqs. (28)–(33). Fig. 30 shows the heterojunction between Ag₂O and CuO. The CuO presents a (bg) ~ 1.7 eV, a conduction band (cb) at –0.3 V SCE and a valence band (vb) at +1.4 SCE [196]. During the IFCT, Ag₂O electrons would hinder the electron-hole recombination in the CuO. This enhances the interfacial charge transfer (IFCT) from Ag₂O to CuO. Nanoparticle of metal/oxides with quantum sizes < 10 nm or 10⁴ atoms transfer their charges at potentials

below the standard values reported in electrochemical tables. Quantum size nanoparticles like Ag₂O to CuO presents a decrease in the space available for charge separation [288]. The ROS shown in the right-hand side of Fig. 30 have been reported to participate in the bacterial inactivation under light irradiation [9–11,16,22,42]. It is likely that small M-NPs with a large surface to mass ratio enhance the e-transfer in the IFCT as reported by Snaith [283], O'Haloran [284] and Warren [285].

A shorthand notation for the visible light induced bacterial inactivation on Cu-Ag-PU films is suggested below by Eq. (40)



3.11. Conclusions

One of the recent developments in photocatalyst involves the interfacial charge transfer through two or three binary oxides. This implies electrostatic attraction, van der Waals forces, and hydrophobic-hydrophilic interactions. Ag- and Cu-NPs/ions have been shown to diffuse through the bacterial membrane through the cell wall porins damaging the cell. Metal/oxide surface-contact effects with the bacterial cell envelope are the other mechanism leading to bacterial inactivation. This proceeds through changes in the cell shape, surface potential, pH surrounding the bacteria, cell wall permeability and destruction of the bacterial cell wall functional groups. Cu- and Ag-NPs and recently more advanced Cu-Ag-NPs materials have been presented in this review. However, the full bactericidal inactivation mechanism is still not understood. The bacterial cell membrane is both a barrier and a channel for the inward and outward movement of chemical species with sizes below the porin diameters. In the gram-negative bacterial membrane structure, porins allow the passage of molecules < 600 Da, in and out of the bacteria. Standard methods of analysis are still needed allowing a quantitative comparison of the inactivation data obtained by different laboratories

Ag-Cu films present an improved bactericide performance compared to Ag or Cu films by themselves. Some articles have been published in the last few years using Ag compounds [302–306] and Cu compounds [307–309] to drive the inactivation of a variety of bacteria. The small size of the metal-ions allows the NPs to enter into the biofilm network compared to antibiotics. Metal/oxide films have advantages over antibiotics since they do not develop bacterial resistance over long treatment periods. This review described that Ag-Cu films disinfect bacteria releasing very small quantities of M-ions (ppb range) while keeping sufficient reserve to ensure a longtime operational lifetime.

The development of kinetically fast, robust antibacterial 2D-polymer films, textiles, and 3D-catheters are urgently needed at the present time. This is also important to hinder the development of infectious biofilms on implants resistant to both the immune system and antibiotics. Vancomycin and Gentamicin are used to combat infections caused by biofilms on tissues and implants but their operational time does not exceed a few days and proceeds by irregular releases of the active components before dying out completely. The administration of effective antibiotics associated with ppb amounts of Cu-Ag is not available nowadays. Such an approach could improve the present situation due to the small size of the Cu- or Ag-ions able to penetrate tissues not reached adequately by antibiotics. Nitrides use for a controlled release of Ag-Cu ions may be developed further and lead to stable and effective antibacterial surfaces. HCAI's are caused by multidrug resistant (MDR) pathogens.

The sputtering of uniform, resistant, adhesive and kinetically faster Cu-Ag films is an innovative way to avoid/preclude biofilm formation in hospitals and health-care facilities. But more advanced antimicrobial films are necessary at the present time on catheters and coatings of medical devices. Improved treatment is critical at the present time since

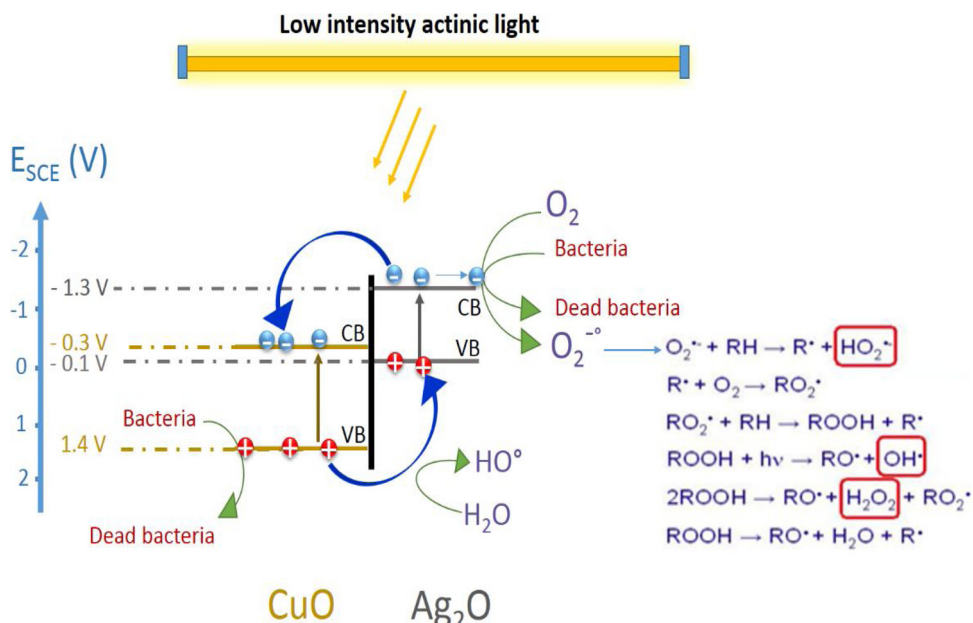


Fig. 30. Schematic for the light induced interfacial charge transfer (IFCT) between Ag_2O and CuO oxides leading to bacterial inactivation. Other details are given in the respective reference [51].

in many cases antibiotics are not available or ineffective. Ag-Cu films, as described in Section 3 of this review, exhibit promising antibacterial kinetics and can be considered as a potential new approach for the effective prevention of bacterial infections. This review describes in detail the potential of light activation to improve the kinetics/efficiency if 2D/3D devices leading to bacterial inactivation. The application in commercial applications of light induced antibacterial processes implies the search of more effective and innovative low-cost antibacterial composites.

3.12. Outlook

Healthcare-associated infections (HCAIs) represent a major public health problem worldwide and are increasing in the last decade. Hospitals go over the bacteria concentration allowed in operation/dressing/residence rooms and are a reservoir of pathogens leading to a higher incidence of HCAIs. Also, during the last few years, an increase in HCAIs has been noticed in hospitals caused by mutant pathogen strains, especially drug resistant strains.

Future work on the effect of heavy metals on pathogenic microorganisms is therefore important. No significant fundamental research has been carried out focusing on the electrostatic attraction, van der Waals forces and hydrophobic-hydrophilic interactions between the bacteria and composite 2D-films and 3D-devices. Care has to be taken to limit the leaching of metals/oxides into the environment since metal pollution has a devastating effect on natural soils. Metals can eliminate/destroy more than 99% of the microbial strains normally found in pristine soils. Therefore, the use of metals should be reduced to avoid unintended consequences to the ecosystem.

Future work is also needed for *in vivo* imaging of bacterial cells inactivation. *In vitro* models do not fully simulate the *in vivo* conditions to accurately reproduce the interaction between M-NPs and bacteria. Recent evidence for the antibacterial effectiveness of silver-alloy urinary catheters has been reported, but more research is needed in this direction. Given that 30–40% of hospitalized patients will be catheterized according to the UK National Health service (NHS) Quality Improvement Scotland report in 2004, the use of more effective Ag/Cu antibacterial catheters should lead to an improved patient treatment. Future research may be directed towards the preparation of M-NPs with increased selectivity and stability reducing considerably their

inherently towards toxicity to mammalian cells while maintaining antimicrobial activity. This may be possible by metal encapsulation. The cytotoxicity reduction in composites of Ag-NPs and Cu-NPs by addition of C- and nitrides is an objective to be addressed in future work. This is of interest for the preparation of antibacterial materials in food, storage containers, kitchenware, food-bags/wrapping, thin films, catheter devices and health-care textiles. Synthetic non-toxic antimicrobial 2D/3D polymers non-toxic to human health presents a potential for a wide range of applications in medicine, pharmacy, food and packing materials. The development of nanoparticles activated by solar/visible/ac-tinic light is in its infancy.

The deposition of thin, uniform and highly adhesive films able to reduce bacterial infections in the dark and under light within acceptable times by new composite materials is urgently needed. This involves more advanced preparation methods (synthesis), an improved antibacterial kinetics and detailed surface characterization of antibacterial films. Potential applications of innovative films on textiles, polymers and catheters/implants should be addressed. Long-term testing of the films performance should validate the application ion these new materials in hospital facilities.

Despite the recent progress made in this area during the last decade, improvements will be necessary in the coming years in order to synthesize high-quality functionalized coatings. NPs with a more complex chemical microstructure, improved morphology and tailor-designed surface are needed to achieve task-specific functions. The higher stability of antibacterial films and how to translate the laboratory findings into large-scale industrial synthesis should be an objective of the future work in this area.

Surface pretreatments have a high potential to improve coated implants such as the acceleration of osseointegration and the protection of antibacterial films from the blood flow in the human body. Future work in this area must also be focused on the toxicity induced by the bactericide films. More advanced sputtering techniques have the potential to open new industrial segments in the health sector. Further research needs include testing of antibacterial devices leading to quasi-instantaneous *in-vitro* and *in-vivo* bactericide action.

The future development of films and catheters need also to consider their mammalian-cell biocompatibility. In addition to the application of the metal/oxide sputtering of surgical/cutting tools, some industries recently started technologies to develop tools in the dental surgery and

in spine/orthopedic implants. The substrates used so far are mainly heat-resistant. In this case, the novel 2D or 3D coatings can be annealed on these substrates.

References

- [1] T.C. An, H.J. Zhao, P.K. Wong, *Advances in Photocatalysis Disinfection*, Springer, Berlin, Heidelberg, 2016.
- [2] P. Lejeune, *Trends Microbiol.* 11 (2003) 79–184.
- [3] I. Francolini, G. Donelli, *FEMS Immunol. Med. Microbiol.* 59 (2010) 227–238.
- [4] W. Wang, G. Li, D. Xia, T. An, H. Zhao, P.K. Wong, *Environ. Sci. Nano* 4 (2017) 782–799.
- [5] J.-A. Byrne, P.S.M. Dunlop, J.W.J. Hamilton, P. Fernandez-Ibanez, I. Polo-Lopez, P.K. Sharma, A.S.M. Vennard, *Molecules* 20 (2015) 5574–5612.
- [6] H. Foster, I. Ditta, S. Varghese, A. Steele, *Appl. Microbiol. Biotechnol.* 90 (2011) 1847–1868.
- [7] H. Shi, G. Li, H. Sun, T. An, P. Wong, *Appl. Catal. B* 158 (2014) 301–307.
- [8] N. Reidy, A. Haase, A. Luch, K. Dawson, I. Lynch, *Materials* 6 (2013) 2295–2950.
- [9] D. Xia, T. An, G. Li, W. Wang, H. Zhao, P.K. Wong, *Water Res.* 99 (2016) 149–161.
- [10] H.J. Klassen, *Burns* 26 (2000) 131–138.
- [11] F. Kang, P.J. Alvarez, D. Zhu, *Environ. Sci. Technol.* 48 (2013) 316–322.
- [12] A. Munoz-Bonilla, M. Fernández-García, *Prog. Polym. Sci.* 37 (2012) 281–239.
- [13] J.R. Morones, J. Elechiguerra, A. Camacho, K. Holt, J. Ramirez, J.M. Yacaman, *Nanotechnology* 16 (2005) 2346–2353.
- [14] S. Pal, Y. Tak, M. Song, *Appl. Environ. Microbiol.* 73 (2007) 1712–1720.
- [15] A.M. El-Badawy, R.G. Silva, B. Morris, K. Scheckel, M.T. Suidan, T.M. Tolaymal, *Environ. Sci. Technol.* 45 (2011) 283–287.
- [16] C. Gunawan, Y. Teoh, P. Marquis, R. Amal, *ACS Nano* 5 (2011) 7214–7225.
- [17] Hyung-Geun Park, Min-K. Yeong Yeo, *Mol. Cell. Toxic.* 3 (2017) 37–47.
- [18] K. Oh, S. Kim, M. Choi, C. Kim, S. Yeong, R. Cho, S. Hahn, J. Yang, *ACS Nano* 9 (2015) 5301–2313.
- [19] A.G. Sotiriou, E.S. Pratsinis, *Environ. Sci. Technol.* 44 (2010) 5649–5654.
- [20] K. Stoimenov, L. Klinger, L. Marchin, J. Klabunde, *Langmuir* 18 (2002) 6679–6686.
- [21] M.I. Mejia, G. Restrepo, J.M. Marín, R. Sanjines, C. Pulgarín, E. Mielczarski, J. Mielczarski, J. Kiwi, *ACS Appl. Mater. Interface* 2 (2010) 230–235.
- [22] C. Gunawan, Y. Teoh, I. Juniahani, C. Marquis, C.R. Amal, *Small* 5 (2009) 341–344.
- [23] M. Xiu, Zhang Z, Q. Puppala, H. Colvin, J. Alvarez, *Nano Lett.* 12 (2012) 4271–4275.
- [24] A.L. Finney, M. O'Halloran, *Science* 300 (2003) 931–936.
- [25] M.G. Gadd, *Microbiology* 156 (2010) 609–643.
- [26] P.V. Asharani, G.L. Kahn, M.P. Hande, S. Valiyaveetil, *ACS Nano* 3 (2009) 279–290.
- [27] I. Sondi, B. Salopek-Sondi, *J. Coll. Interface Sci.* 275 (2004) 177–182.
- [28] O. Choi, Z. Hu, *Environ. Sci. Technol.* 4 (2008) 4583–4588.
- [29] Y. Lu, K. Chou, *J. Chinese Inst. Chem. Eng.* 39 (2008) 673–678.
- [30] J.S. Kim, E. Kuk, K.N. Yu, J.H. Kim, S.J. Park, H.J. Lee, S.H. Kim, Y.K. Park, Y.H. Park, C.Y. Hwang, Y.K. Kim, Y.S. Lee, D.H. Jeong, M.H. Cho, J. Nanomed. Nanotechnol. 3 (2007) 95–101.
- [31] M. Raffi, F. Hussain, T.M. Bhatti, J.I. Akhter, A. Hameed, M.M. Hasan, *J. Mater. Sci. Technol.* 2 (2008) 192–196.
- [32] A.B. Smetana, K.J. Klabunde, G.R. Marchin, C.M. Sorenson, *Langmuir* 24 (2008) 7457–7464.
- [33] L. Kvitek, A. Panacek, J. Soukupova, M. Kolar, R. Vecerova, R. Prucek, M. Holecova, R. Zboril, *J. Phys. Chem. C* 112 (2008) 5825–5834.
- [34] M. Raffi, F. Hussain, T. Bhatti, J. Akhter, A. Hameed, M. Hasan, *J. Mater. Technol.* 21 (2008) 192–198.
- [35] E. Navarro, F. Piccapietra, B. Wagner, F. Marconi, R. Kaegi, N. Odzak, L. Sigg, R. Behra, *Environ. Sci. Technol.* 42 (2008) 8959–8964.
- [36] A. Panacek, L. Kvitek, R. Prucek, M. Kolar, R. Vecerova, N. Pizurova, V. Sharma, T. Nevecna, R. Zboril, *J. Phys. Chem. B* 110 (2006) 16248–16253.
- [37] D. Wei, W. Sun, W. Qiang, Y. Ye, X. Ma, *Carbohydr. Res.* 344 (2009) 2375–238.
- [38] J.L. Gardea-Torresdey, E. Gomez, J.R. Peralta-Videa, G. Parsons, H. Troiani, J.M. Yacaman, *Langmuir* 19 (2003) 1357–1361.
- [39] S. Shankar, R.Ahma.M. Sastry, *J. Colloid Interface Sci.* 275 (2004) 496–502.
- [40] J. Huang, Q. Li, D. Sun, Y. Lu, Y. Su, X. Yang, H. Wang, Y. Wang, W. Shao, N. He, *Nanotechnology* 18 (2007) 1–11.
- [41] M. Sathishkumar, K. Sneha, W. Won, W. Cho, S. Kim, S. Yun, *Colloids Surf. B Biointerfaces* 73 (2009) 332–338.
- [42] H. Bar, D. Bhui, P. Sahoo, S. Sarkar, A. De, Misra, *Colloids Surf. A Physicochem. Eng. Asp.* 339 (2009) 134–139.
- [43] V. Sharma, R. Yngard, Y. Lin, *Adv. Coll. Interface Sci.* 145 (2009) 83–96.
- [44] Y. Sun, Y. Xia, *Science* 298 (2002) 2176–2179.
- [45] M. Mitrano, E. Rimmelle, A. Wichser, R. Erni, M. Height, B. Nowak, *ACS Nano* 8 (2014) 7208–7213.
- [46] J. Schnadt, J. Knudsen, X.L. Hu, A. Michaelides, R.T. Vang, K. Reuter, Z. Li, E. Laegsgaard, M. Sheffer, F. Besenbacher, *Phys. Rev. B* 80 (2009) 075424.
- [47] A. Suresh, D. Pelletier, W. Wang, J. Morrell-Falvey, B. Gu, M. Doktycz, *Langmuir* 28 (2012) 2727–2736.
- [48] K. Lance Kelly, Eduardo Coronado, Lin Lin Zhao, George C. Schatz, *J. Phys. Chem. B* 107 (2003) 7343–7350.
- [49] Z. Pillai, P.V. Kamat, *J. Phys. Chem. B* 108 (2004) 945–951.
- [50] L. Slomberg, D. Broadnax, A. Hunter, W. Carpenter, H. Schoenfisch, *ACS Appl. Mater. Interfaces* 5 (2013) 9322–9329.
- [51] S. Rtimi, R. Sanjines, C. Pulgarin, J. Kiwi, *ACS Appl. Mater. Interface* 8 (2016) 47–55.
- [52] S. Rtimi, R. Sanjines, C. Pulgarin, J. Kiwi, *ACS Appl. Mater. Interface* 8 (2016) 56–64.
- [53] J. Liu, D. Sonshine, S. Shervant, J. Hurt, *ACS Nano* 4 (2010) 6903–6913.
- [54] Z. Lu, L. Zhou, Z. Zhang, W. Shi, Z. Xiong, Z. Xie, H. Xie, D. Pang, P. Shen, *Langmuir* 19 (2003) 8765–8768.
- [55] K. Hardee, A. Bard, *J. Electrochem. Soc.* 124 (1978) 215–224.
- [56] A. Henglein, M. Giersig, *J. Phys. Chem. B* 103 (1999) 9533–9539.
- [57] G. Biedermann, G.L. Sillén, *Acta Chem. Scand.* 14 (1960) 717–725.
- [58] G.A. Sotiriou, A. Meyer, J. Knijnenburg, S. Panke, S.E. Pratsinis, *Langmuir* 28 (2012) 15929–15936.
- [59] B. Le Ouay, F. Stellacci, *Nano Today* 10 (2015) 339–354.
- [60] M.E. Semberg, P.E. Orndorff, N.A. Monteiro-Riviere, *Nanotoxicology* 5 (2011) 244–253.
- [61] R.H. Jensen, N. Davidson, *Biopolymers* 4 (1966) 17–32.
- [62] S. Sohs, *Free Radical Biol. Med.* 18 (1995) 321–336.
- [63] H.J. Park, J.Y. Jim, J. Kim, J.H. Lee, J.S. Hahn, M.B. Gu, J. Yoon, *Water Res.* 43 (2009) 1027–1037.
- [64] M. Hermansson, *Colloids Surf. B Biointerfaces* 14 (1999) 105–119.
- [65] S. Goviddan, E.A.K. Nivetha, R. Saravanan, V. Narayanan, A. Stephen, *Appl. Nanosci.* 3 (2012) 209–303.
- [66] A. Ollofs, C. Grosse-Siestrup, S. Bisson, M. Rinck, R. Rudolph, U. Gross, *Biomaterials* 15 (1994) 753–758.
- [67] J. Guggenbichler, M. Böswald, S. Lugauer, T. Krall, *J. Antimicrob. Chemother.* 27 (Supl. 1) (1999) 16–23.
- [68] D. Roe, B. Karandikar, N. Bonn-Savage, B. Gibbins, J.B. Roulet, *J. Antimicrob. Chemother.* 61 (2008) 869–876.
- [69] K. Galiano, C. Pfeifer, K. Engelhart, G. Grossner, P. Lackner, C. Huck, C. Lass-Flori, A. Obwegesser, *Neurol. Res.* 30 (2008) 285–287.
- [70] L. Zhang, R. Dillert, D. Bahnemann, M. Vormoor, *Environ. Environ. Sci.* 5 (2012) 7491–7507.
- [71] K. Page, M. Wilson, M. Mordan, N. Chrzanowski, W. Knowles, P. Parkin, *J. Mater. Sci.* 46 (2010) 6355–6363.
- [72] K. Page, R. Palgrave, I.P. Parkin, M. Wilson, Sh. Savin, A. Chadwick, *J. Mater. Chem.* 25 (2007) 95–104.
- [73] H.A. Foster, P. Sheet, W.D. Sheet, P. Evans, S. Varghese, N. Rutschke, H.M. Yates, J. Photochem. Photobiol. A Chem. 216 (2010) 283–289.
- [74] P.S.M. Dunlop, P.C. Sheeran, J.-M. Byrne, A. McMahon, M. Boyle, G.K. McGuigan, *J. Photochem. Photobiol. A Chem.* 216 (2010) 3303–3010.
- [75] M.H. Yates, A.L. Brook, L.A. Ditta, H.A. Foster, D.W.A. Steele, A. J. Photochem. Photobiol. A. 197 (2008) 197–208.
- [76] P.J. Kelly, H. Li, P.S. Benson, K.A. Whitehead, J. Verran, R.D. Arnell, I. Iordanova, *Surf. Coat. Technol.* 205 (2010) 1606–1610.
- [77] L. Tosheva, S. Belkhair, M. Gackowski, S. Malic, N. Al-Shanti, J. Verran, *Colloids Surf. B Biointerfaces* 157 (2017) 254–260.
- [78] T. Yuranova, A.G. Rincon, C. Pulgarin, D. Laub, N. Xanthopoulos, H.-J. Mathieu, J. Kiwi, *J. Photochem. Photobiol. A Chem.* 181 (2006) 363–369.
- [79] T. Yuranova, A.G. Rincon, D. Laub, J. Kiwi, *Catal. Today* 122 (2007) 109–117.
- [80] J. Metch, Y. Ma, A. Pruden, P. Viskenland, *Environ. Sci. Water Res. Technol.* 1 (2015) 823–831.
- [81] S. Loo, W. Krantz, A. Fane, Y. Gao, T. Lim, X. Hu, *Environ. Sci. Technol.* 49 (2015) 2310–2318.
- [82] L. Zhang, J. Yu, H. Yip, Q. Li, K. Kwong, A. Xu, P. Wong, *Langmuir* 19 (2003) 10372–10380.
- [83] P. Wang, B. Huang, X. Qin, X. Zhang, Y. Dai, J. Wei, M. Whngbo, *Angew. Chem. Int. Ed.* 47 (2008) 7931–7933.
- [84] O. Akhavan, J. Colloid, *Interface Sci.* 336 (2009) 117–124.
- [85] G. Fuertes, O. Sanchez-Munoz, E. Pudrueza, K. Abderrafti, J. Salgado, E. Jimenez, *Langmuir* 27 (2011) 2826–2833.
- [86] M. Maclean, S. MacGregor, J. Anderson, G. Woolsey, *Appl. Environ. Microbiol.* 75 (2009) 1932–1938.
- [87] M. Pelaza, N.T. Nolan, S.C. Pillai, M.K. Seery, P. Falaras, A.G. Kontos, P.S.M. Dunlop, J.W.J. Hamilton, J.-A. Byrne, K. O'Shea, M.H. Entezari, D.D. Dionysiou, *Appl. Catal. B* 125 (2012) 331–349.
- [88] P. Christopher, H. Xin, S. Linic, *Nat. Chem. Biol.* 3 (2001) 467–472.
- [89] K. Sarakinos, J. Alami, S. Konstantinidis, *High power pulsed magnetron sputtering A review on scientific and engineering state of the art*, *Surf. Coat. Technol.* 201 (2010) 1661–1684.
- [90] P.J. Kelly, R.D. Arnell, *Vacuum* 56 (2000) 159–172.
- [91] A.P. Ehiasarian, *Pure Appl. Chem.* 82 (2010) 1247–1258.
- [92] J.E. Hopwood (Ed.), *Thin Films Plasma Physics*, 27 Academic Press, 2000, pp. 180–206.
- [93] Y. Chen, C. Hsu, J. He, *Surf. Coat. Technol.* 232 (2013) 868–875.
- [94] E. Cavaliere, S. De Cesari, G. Landini, E. Riccobono, L. Pallecchi, G.M. Rossolini, L. Gavioli, *Rev. Nanomed. Nanotechnol. Biol. Med.* 11 (2015) 1417–1423.
- [95] H. Tjeng, J. Meinders, V. Elp, J. Ghijssen, A. Sawatzky, *Phys. Rev. B* 41 (1990) 3190–3199.
- [96] Y. Ida, S. Watase, T. Shingawa, M. Watanabe, M. Chigane, M. Inaba, A. Tasaka, M. Izaki, *Chem. Mater.* 20 (2008) 1254–1256.
- [97] R. Memming, F. Möllers, G. Neumann, *J. Electrochem. Soc.* 117 (1970) 451–457.
- [98] R. Bauer, H. Fallmann, *J. Res. Chem. Int.* 23 (1997) 341–354.
- [99] A. Safarzadeh-Amiri, J.R. Bolton, S.R. Carter, *J. Adv. Oxid. Technol.* 1 (1996) 18–29.
- [100] D.M. Stanbury, *Adv. Inorg. Chem.* 33 (1989) 69–138.

[101] B. Sulzberger, S. Canonica, T. Egli, W. Giger, J. Klausen, U. von Gunten, *Chimia* 51 (1997) 900–907.

[102] A. Fujishima, X. Zhang, D. Tryk, *Appl. Surf. Sci.* 63 (2008) 515–582.

[103] V. Nadtchenko, J. Kiwi, *Environ. Sci. Technol.* 32 (1998) 3273–3281.

[104] H. Gerisher, J. Katz (Eds.), *Dahlem Conferences Held on 1978 on the Light-Induced Charge Separation*, Weinheim, Bergs, Germany, 1979, p. 299. Edited.

[105] R. Plowman, R. Graves, N. Griffin, L. Taylor, *Can. J. Infect. Control* 47 (2001) 198–204.

[106] A. Kramer, A.I. Schwabke, G. Kampf, *Diseases* 6 (2006) 137–146.

[107] S. Rossnagel, J. Hopwood, *Appl. Phys. Lett.* 63 (1993) 3285–3287.

[108] K. Sarakinos, J. Alami, D. Konstantinidis, *Surf. Coat. Technol.* 204 (2010) 1661–1684.

[109] S. Dancer, *J. Hosp. Infect.* 73 (2009) 378–386.

[110] D. Tal, *J. Hosp. Infect.* 43 (1999) 13–17.

[111] R.M. Klevens, J.R. Edwards, C.L. Richards, T.C. Horan, R.P. Gaynes, D.A. Pollock, D.M. Cardo, *Public Health Rep.* 122 (2007) 160–166.

[112] L. Geranio, M. Heiberger, B. Nowak, *Environ. Sci. Technol.* 43 (2009) 8113–8118.

[113] C. Lefard, E. Hotze, G. Lowry, G. Brown, *Environ. Sci. Technol.* 46 (2012) 6900–6914.

[114] T. Yuranova, A.G. Rincon, C. Pulgarin, D. Laub, N. Xanthopoulos, H.-J. Mathieu, J. Kiwi, *J. Photochem. Photobiol. A* 181 (2006) 363–369.

[115] T. Yuranova, A.G. Rincon, A. Bozzi, S. Parra, C. Pulgarin, P. Albers, J. Kiwi, *J. Photochem. Photobiol. A* 161 (2003) 27–34.

[116] S. Rtimi, O. Baghrache, R. Sanjines, C. Pulgarin, M. Ben-Simon, J.-C. Lavanchy, A. Houas, J. Kiwi, *Appl. Catal. B* 123–124 (2012) 306–315.

[117] S. Rtimi, O. Baghrache, C. Pulgarin, R. Sanjines, J. Kiwi, *RSC Adv.* 2 (2012) 8591–8595.

[118] A. Wisbey, J. Gregson, M. Tuke, *Biomaterials* 8 (1987) 9477–9480.

[119] J. Thiel, L. Pakstis, S. Buzby, M. Raffi, J. Ni, P.S. Shah, *Small* 3 (2007) 799–803.

[120] Epitaxial growth, part B, chapter 4 by J. A. Venables and G. L Price, in: J.W. Mathews (Ed.), *Nucleation of Thin Films*, Academic Press, New York, 1975, pp. 382–435.

[121] H. Sato, S. Shinozaki, *J. Appl. Phys.* 41 (1970) 3165–3169.

[122] H. Jing, N. Large, O. Zhang, H. Wang, *J. Phys. Chem. C* 118 (2014) 19948–19963.

[123] A.P. Ehiasarian, R. New, W.D. Munoz, L. Hultman, U. Helmersson, V. Kouznetsov, *Vacuum* 65 (2002) 147–154.

[124] J. Li, J. Moore, W. Sproul, B. Mishra, Z. Wu, J. Wang, *Surf. Coat. Technol.* 204 (2010) 2230–2239.

[125] A.P. Ehiasarian, *Pure Appl. Chem.* 82 (2010) 1247–1258.

[126] S. Rtimi, C. Pulgarin, A. Houas, R. Sanjines, J.-C. Lavanchy, J. Kiwi, *J. Hazard. Mat.* 260 (2013) 860–868.

[127] S. Rtimi, M. Pascu, R. Sanjines, C. Pulgarin, M. Bensimon, J.-C. Lavanchy, J. Kiwi, *Appl. Catal. B* 138 (2013) 113–121.

[128] O. Baghrache, S. Rtimi R, A. Zertal, C. Pulgarin, R. Sanjines, J. Kiwi, *Appl. Catal. B* 174 (2015) 376–382.

[129] G. Koster, M. Huijben, G. Rijnders (Eds.), *Epitaxial Growth of Complex Metal Oxides*, Woodhead Pub Co., Cambridge, UK, 2015.

[130] A. Fujishima, K. Hashimoto, T. Watanabe, *TiO₂ Photocatalysis, Fundamental and Applications*, BKC, Inc, Tokyo, 1999.

[131] J. Winkler, *Titanium Oxide*, Vincentz, Hannover, 2003.

[132] H.P. Boehm, Acidic and basic properties of hydroxylated metal oxide surfaces, *Discuss. Faraday Soc.* 52 (1971) 264–275.

[133] A. Fujishima, K. Honda, *Nature* 238 (1972) 3–38.

[134] K. Vasilev, J. Cook, H.J. Griesser, *Expert Rev. Med. Devices* 6 (2014) 553–567.

[135] K. Vasilev, V. Sah, K. Anselme, C. Ndi, M. Mateescu, B. Dollmann, P. Martinek, H. Ys, L. Ploux, H.J. Griesser, *Nano Lett.* 10 (2010) 202–207.

[136] M. Pourbaix, *Atlas of electrochemical equilibria in aqueous solutions*, Nat Assoc. Corros. Eng. Cebelcor. Sci. (1982).

[137] J. Schneider, M. Matsuoka, M. Takeuchi, J. Zhang, Yu Horiuchi, M. Anpo, D. Bahnemann, *Chem. Rev.* 4 (2014) 9919–9986.

[138] A. Kubacka, M.S. Diez, D. Rojo, R. Bargiela, C. Cordia, I. Zapico, J. Albar, C. Barbas, V. Martis dos Santos, M.F. Garcia, M. Ferrer, *Nat. Sci. Rep.* 4 (2014) 4134–4146.

[139] H. Foster, I. Ditta, S. Varghese, A. Steele, *Appl. Microbiol. Biotechnol.* 90 (2011) 1847–1868.

[140] S. Rtimi, O. Baghrache, R. Sanjines, C. Pulgarin, M. Bensimon, J. Kiwi, *J. Photochem. Photobiol. A* 256 (2013) 52–63.

[141] H. Nikaido, *J. Biol. Chem.* 269 (1994) 3905–3909.

[142] X. Li, H. Nikaido, K. Williams, *J. Bacteriol.* 179 (1997) 6127–6132.

[143] A. Nozik, *Photo-effects at the Semiconductor Electrolyte Interface*, ACS Symposium Series, American Chemical Society, Washington, 1990.

[144] R.A. Smith, *Semiconductors*, Cambridge Univ. Press, 1978.

[145] S. Rtimi, C. Pulgarin, M. Bensimon, J. Kiwi, *Colloid Surf. B*, *Bio-Interfaces* 144 (2016) 222–228.

[146] S. Rtimi, S. Giannakis, M. Bensimon, C. Pulgarin, R. Sanjines, J. Kiwi, *Appl. Catal. B* 191 (2016) 42–52.

[147] S. Rossnagel, J. Hopwood, *Appl. Phys. Lett.* 63 (1993) 3285–3290.

[148] U. Helmersson, M. Lattemann, J. Bohlmark, J.T. Gudmundsson, *Thin Solid Films* 513 (2006) 1–24.

[149] J. Joo, *J. Vac. Sci. Technol. A* 18 (2000) 23–33.

[150] D. Manova, J. Gerlach, S. Mandl, *Materials* 3 (2010) 4109–4141.

[151] A. Mishra, P.J. Kelly, J.W. Bradley, *J. Phys. D Appl. Phys.* 44 (2011) 425201.

[152] O. Baghrache, A.P. Ehiasarian, E. Kusiak-Nejman, A.W. Morawski, C. Pulgarin, R. Sanjines, J. Kiwi, *Thin Solid Films* 520 (2012) 3567–3573.

[153] O. Baghrache, A.P. Ehiasarian, E. Kusiak-Nejman, A.W. Morawski, C. Pulgarin, R. Sanjines, J. Kiwi, *J. Photochem. Photobiol. A* 227 (2012) 11–17.

[154] S. Rtimi, C. Pulgarin, R. Sanjines, J. Kiwi, *RSC Adv.* 3 (2013) 16345–16349.

[155] S. Rtimi, O. Baghrache, C. Pulgarin, A. Ehiasarian, R. Bandorf, J. Kiwi, *Surf. Coat. Technol.* 250 (2014) 14–20.

[156] R. Cao, C. Saracini, J.W. Gainsbach, M.T. Kieber-Emmons, M.A. Siegler, E.I. Solomon, S. Fukuzumi, K.D. Karlin, *J. Am. Chem. Soc.* 138 (2016) 7055–7066.

[157] E. Bargali, F. Lavorini, M. Pistolessi, E. Rosi, E. Rota, L. Voitolini, *J. Trace Elem. Med. Biol.* 42 (2017) 39–44.

[158] R.T. Dean, S.P. Wolff, M.A. McEligott, L. Eichorn, *Free Radical Res. Comm.* 7 (1989) 97–103.

[159] S. Rtimi, C. Pulgarin, M. Bensimon, J. Kiwi, *Colloids Surf. B* *Biointerfaces* 144 (2016) 222–228.

[160] M. Sportelli, R. Picca, N. Cioffi, D. Phienix, F. Harris, S. Dennison, *Novel Antimicrobial Agents and Strategies* (Editors), Wiley Verlag, Weinheim, 2015, pp. 181–218.

[161] J. Lemire, J. Harrison, R. Turner, *Nat. Rev. Microbiol.* 11 (2013) 371–384.

[162] S. Dancer, *J. Hosp. Infect.* 7 (2007) 78–89.

[163] N. Hoiby, Th. Bjarnsholt, M. Givskov, S. Molin, O. Ciofu, *J. Antimicrob. Agent* 35 (2010) 322–335.

[164] G. Borkow, J. Gabbay, *J. FASEB* 18 (2008) 1728–1730.

[165] G. Borkow, J. Gabbay, *Curr. Chem. Biol.* 37 (2009) 272–278.

[166] G. Borkow, J. Gabbay, R. Dardik, A. Eidelman, Y. Lavie, Y. Grunfeld, S. Iker, M. Huszar, R. Zatcoff, M. Marikovsky, *Wound Repair Regen.* 18 (2010) 266–275.

[167] A. Munoz-Bonilla, M. Fernandez Garcia, *Prog. Polymer. Sci.* 37 (2012) 281–339.

[168] O. Bondarenko, K. Juganson, A. Ivesk, K. Kasernets, M. Mortimer, A. Karhu, *Arch. Toxic.* 87 (2013) 1181–1200.

[169] E. Rentz, *J. Nutr. Environ. Med.* 13 (2003) 109–118.

[170] S. Rtimi, C. Pulgarin, J. Kiwi, *Coatings* 7 (2017) 20–49.

[171] C.A. Carrington, M. Hinton, G.C. Mead, I. Chopra, *Adv. Microbiol. Physiol.* 32 (1991) 87–108.

[172] J. Waldron, J. Robinson, *Nat. Rev. Microbiol.* 7 (2009) 25–35.

[173] D. Quaranta, T. Krans, C. Espirito Santo, C. Elowsky, D. Domaille, C. Chang, G. Grass, *Appl. Environ. Microbiol.* 77 (2011) 416–426.

[174] C. Espirito Santo, E. Lam, C. Elowsky, C. Quaranta, D. Domaille, C. Chang, G. Grass, *Appl. Environ. Microbiol.* 77 (2011) 794–802.

[175] G. Grass, C. Rensing, M. Solioz, *Appl. Environ. Microbiol.* 77 (2011) 1541–1547.

[176] C. Santo, P. Morais, G. Grass, *Appl. Environ. Microbiol.* 76 (2008) 1341–1348.

[177] K. Sunada, T. Watanabe, K. Hashimoto, *Environ. Sci. Technol.* 37 (2003) 4785–4789.

[178] X. Qiu, M. Miyauchi, K. Sunada, M. Minshima, Y. Min-Liu, D. Lu, Y. Li, Y. Shimodaira, Y. Hosogi, K. Kuroda, Hashimoto, *ACS Nano* 6 (2012) 1609–1618.

[179] J. Elguindi, J. Wagner, C. Rensing, *J. Appl. Microbiol.* 106 (2009) 1448–1455.

[180] J. Noyce, H. Michels, C. Keevil, et al., *J. Hosp. Infect.* 6 (2006) 289–297.

[181] J. Noyce, H. Michels, C. Keevil, *Appl. Environ. Microbiol.* 72 (2006) 4239–4244.

[182] I. Perelshteyn, N. Applerot, E. Perkas, E. Wehrshutz-Sigl, E. Hasman, G. Guebitz, A. Gedanken, *Surf. Coat. Technol.* 204 (2009) 54–57.

[183] M. Eshed, J. Lelloche, S. Matalon, A. Gedanken, M. Banin, *Langmuir* 28 (2012) 12288–12295.

[184] N. Cioffi, N. Ditaranto, L. Torsi, L. Pica, R. Sabatini, A. Valenti, A. Novello, G. Tantillo, T. Bleve-Zacheo, P. Zambonin, *Anal. Bioanal. Chem.* 381 (2005) 607–616.

[185] N. Cady, L. Behnke, D. Strickland, *Adv. Funct. Mater.* 21 (2011) 2506–2514.

[186] B. Jia, Y. Mei, L. Cheng, J. Zhou, L. Zhang, *ACS Appl. Mater. Interface* 4 (2012) 2897–2902.

[187] M. Usman, M. El-Zowalaty, K. Shameli, N. Zainuddin, M. Salama, N. Ibrahim, *Int. J. Nanomed.* 8 (2013) 4467–4479.

[188] D. Sun, D. Xu, C. Yang, M. Shahzad, Z. Sun, J. Xia, J. Zhao, T. Gu, K. Yang, G. Wang, *Sci. Rep.* 6 (2016) 29244–29249.

[189] O. Akhavan, E. Ghaderi, *Surf. Coat. Technol.* 205 (2010) 219–223.

[190] A. Mikolay, S. Huggett, L. Tikana, G. Gass, J. Braun, D. Nies, *Appl. Microbiol. Biotechnol.* 87 (2010) 1875–1879.

[191] A. Chatterjee, K. Sarker, P. Chatopadhyay, P. Aich, R. Chakraborty, T. Basu, *Nanotechnology* 23 (2012) 085103.

[192] V. Aina, G. Cerrato, G. Martra, G. Malvasi, G. Lusvardi, L. Menabue, *Appl. Surf. Sci.* 283 (2013) 240–248.

[193] A. Fritsche, M. Haenle, C. Zietz, W. Mittelmeier, G.-H. Neumann, F. Heidenau, B. Finke, R. Bader, *J. Mater. Sci.* 44 (2000) 5544–5551.

[194] M. Zielecka, E. Bujnowska, B. Kepska, M. Wenda, M. Piotrowska, *Prog. Org. Coat.* 72 (2011) 193–201.

[195] J.-P. Kelly, R.-D. Arnell, *Vacuum* 76 (2000) 159–172.

[196] S. Rtimi, O. Baghrache, C. Pulgarin, J. Kiwi, *Surf. Coat. Technol.* 32 (2013) 804–813.

[197] J. Lin, J. Moore, W. Sproul, B. Mishra, Z. Wu, J. Wang, *Surf. Coat. Technol.* 204 (2010) 2230–2239.

[198] S. Rtimi, O. Baghrache, C. Pulgarin, A. Ehiasarian, R. Bandorf, J. Kiwi, *Surf. Coat. Technol.* 250 (2014) 14–20.

[199] S. Rtimi, J. Kiwi, *Appl. Catal. B* 130–131 (2013) 62–73.

[200] C. Castro, R. Sanjines, C. Pulgarin, P. Osorio, S. Giraldo, J. Kiwi, *J. Photochem. Photobiol. A* 216 (2010) 295–302.

[201] P. Osorio, R. Sanjines, R. Ruales, C. Castro, C. Pulgarin, A.-J. Rengifo, J.-C. Lavanchy, J. Kiwi, *J. Photochem. Photobiol. A* 220 (2011) 70–76.

[202] C.D. Wagner, W.M. Riggs, L.E. Davies, G.E. Mullenberg (Eds.), *Handbook of X-Ray Photoelectron Spectroscopy*, Perkin-Elmer Corp, Phys. Electronics Division, Minn. 19790, USA, 2018.

[203] S. Rtimi, R. Sanjines, C. Pulgarin, J. Kiwi, *Biointerphases* 9 (2014) 029012.

[204] E. Cubillo, C. Pecharroman, E. Aguilar, J. Santaren, J. Moya, *J. Mater. Sci.* 4 (2006) 5208–5212.

[205] Q. Wei, L. Yu, N. Wu, S. Hong, *J. Ind. Textiles* 37 (2008) 275–283.

[206] J. Musil, J. Blazek, K. Fajfrlik, R. Cerstvy, *Surf. Sci. Technol.* 264 (2015) 114–120.

[207] L. Macomber, C. Rensing, J. A. Imlay, *J. Bacter.* 189 (2007) 8344–8349.

[208] L. Macomber, J.A. Imlay, *Proc. Nat. Acad. Sci. U. S. A.* 106 (2009) 8344–8349.

[209] <http://www.epa.gov/pesticides/factsheets/copper-alloy-products.htm>.

[210] T. Nguyen, H. Park, J. Kim, H. Kim, H. Lee, J. Yoon, C.H. Lee, *Environ. Sci. Technol.* 47 (2013) 13661–13667.

[211] S. Lebedev, A. Volodina, E. Deneiga, I. Fedorov, *Biofizika* 50 (2005) 107–113.

[212] R. Gunther, M. Hanna, P. Mason, S. Cohen, *Arch. Biochem. Biophys.* 31 (1995) 515–522.

[213] S. Mathews, R. Kumar, M. Solioz, *App. Environ. Microbiol.* 81 (2015) 6399–6403.

[214] M. Macia, E. Rojo-Moliner, A. Olivier, *Clin. Microbiol. Infect.* 20 (2014) 981–990.

[215] Y. Zhang, L. Ma, J. Lin, Y. Yu, *Environ. Sci. Technol.* 41 (2007) 6284–6269.

[216] M. Miyachi, H. Irie, Min Liu, S. Qiu, H. Yu, K. Sunada, K. Hashimoto, *J. Phys. Chem. Lett.* 7 (2016) 75–84.

[217] S. Rtimi, R. Sanjines, M. Andrzejczuk, C. Pulgarin, A. Kulik, J. Kiwi, *Surf. Coat. Technol.* 25 (2014) 333–343.

[218] S. Rtimi, J. Nesic, C. Pulgarin, R. Sanjines, M. Bensimon, J. Kiwi, *Interface Focus* (2015) 5/rfsf0046.

[219] S. Rtimi, C. Pulgarin, R. Sanjines, J. Kiwi, *Appl. Catal. B* 162 (2015) 236–244.

[220] S. Rtimi, C. Pulgarin, R. Sanjines, V. Nadtochenko, J.-C. Lavanchy, J. Kiwi, *ACS Appl. Mater. Interface* 7 (2015) 12832–12839.

[221] J. Tauc, *Mater. Res. Bull.* 3 (1968) 37–46.

[222] A. Emeline, G. Kataeva, A. Litke, A. Rudakova, V. Riabchuk, N. Serpone, *Langmuir* 14 (1988) 5011–5022.

[223] G. Kumar, D. Gomathi, *J. Phys. Chem. C* 115 (2011) 13211–13241.

[224] C. Akubuilo, E. Verykios, *J. Catal.* 103 (1987) 320–333.

[225] P. Wardman, *J. Phys. Chem. Ref. Data* 18 (1989) 1637–1755.

[226] M. Hajipour, K. Fromm, A. Askaharran, D. Aberasturi, I. Larramendini, T. Rojo, V. Serpooshan, W. Parak, M. Mahmoudi, *Trends Biotechnol.* 30 (2012) 499–511.

[227] A. Houas, H. Lachheb, M. Ksibi, E. Elaloui, C. Guillard, J.-M. Herrman, *Appl. Catal. B* 31 (2001) 145–147.

[228] A. Kraeutler, A. Bard, *J. Am. Chem. Soc.* 100 (1978) 2399–2444.

[229] Z. Lu, Z.L. Zhou, Z. Zhang, W. Shi, Z. Xie, D. Pang, P. Shen, *Langmuir* 19 (2003) 8765–8768.

[230] S. Rtimi, R. Sanjines, C. Pulgarin, M. Bensimon, J. Kiwi, *Appl. Catal. B* 182 (2016) 277–285.

[231] S. Rtimi, M. Robyr, A. Aybush, I. Shelaev, F. Gostev, V. Nadtochenko, J. Kiwi, *Appl. Catal. B* 20 (2017) 135–147.

[232] O. Baghriche, S. Rtimi, C. Pulgarin, R. Sanjines, *Appl. Mater. Interface* 4 (2012) 5234–5240.

[233] F. Heidenau, F. Mittelmeier, R. Detsch, M. Haenle, M. Gollwitzer, *J. Mater. Sci. Mater. Med.* 16 (2005) 883–888.

[234] C. Zietz, A. Fritsche, B. Finke, V. Stranak, M. Haenle, R. Hippler, W. Mittelmeier, R. Bader, *Bioorg. Chem. Appl.* (2012) 5 ID 850390.

[235] E. Cassaret, S. Doulls, *Toxicology, the Basic Science of Poisons*, 5th ed., McGraw Hill, New York, 2000.

[236] R. Kaegi, B. Ulrich, R. Sinnet, R. Vonbank, A. Wichser, S. Zuleeg, S. Simler, H. Brunner, H. Vonnmont, M. Burkhardt, *Environ. Pollut.* 156 (2008) 233–239.

[237] W. Zhang, Y. Zhang, J. Ji, Q. Yan, A. Huang, P. Chu, *J. Biomed. Mater. Res. Part B Appl. Biomater.* 83A (2007) 838–844.

[238] L. Weaver, J. Noyce, H. Michels, C. Keevil, *J. Appl. Microbiol.* 109 (2010) 2200–2205.

[239] R. Liu, K. Meemarzadeh, B. Chang, Y. Zhang, Z. Ma, R. Allaker, L. Ren, Ke Yang, *Nat. Sci. Rep.* 6 (2016) 29985–29985.

[240] R. Nakano, M. Hara, H. Ishiguro, Y. Yao, T. Ochiai, K. Nakata, T. Murakami, J. Kajioka, K. Sunada, K. Hashimoto, A. Fujishima, Y. Kubota, *Catalysts* 3 (2013) 310–323.

[241] K. Kuhn, I. Chaberny, K. Massholder, M. Strickler, V. Benz, H.G. Sonntag, L. Erdinger, *Chemosphere* 53 (2003) 71–77.

[242] R. van Grieken, J. Marugan, C. Pablos, L. Furones, A. Lopez, *Appl. Catal. B* 100 (2010) 212–220.

[243] T. Pham, B. Lee, *J. Photochem. Photobiol. A Chem.* 307–308 (2015) 16–22.

[244] L. rio, E. Kusija, J. Kiwi, C. Pulgarin, A. Trampuz, A. Bizzini, *Appl. Environ. Microbiol.* 78 (2014) 8176–8182.

[245] S. Rtimi, M. Ballo, C. Pulgarin, J. Entenza, A. Bizzini, J. Kiwi, *Appl. Catal. A Gen.* 498 (2015) 4185–4191.

[246] M. Ballo, S. Rtimi, S. Mancini, J. Kiwi, C. Pulgarin, J. Entenza, A. Bizzini, *Appl. Microbiol. Cell Pathol.* 100 (2016) 5945–5953.

[247] M. Ballo, S. Rtimi, C. Pulgarin, N. Hopf, A. Berthet, J. Kiwi, Ph. J. Moreillon, A. Entenza, Bizzini, *Antimicrob. Agents Chemother.* 60 (2016) 5349–5356.

[248] M. Ballo, S. Rtimi, J. Kiwi, C. Pulgarin, J.M. Entenza, A. Bizzini, *J. Photochem. Photobiol. B* 174 (2017) 229–234.

[249] V. Ondok, J. Musil, M. Meissner, R. Cerstvy, K. Fajfrlik, Two functional DC sputtered Cu-containing TiO_2 thin films, *J. Photochem. Photobiol. A Chem.* 209 (2010) 158–162.

[250] P. Petrov, A. Myers, J.E. Greene, J.R. Abelson, *J. Vac. Sci. Technol. A* 12 (1994) 2848–2851.

[251] A. Anders, *J. Appl. Phys.* 121 (2017) 171101.

[252] J. Kiwi, V. Nadtochenko, *J. Phys. Chem. B* 108 (2004) 17675–17684.

[253] J. Kiwi, V. Nadtochenko, *Langmuir* 21 (2005) 4631–4641.

[254] J. Nesic, S. Rtimi, D. Laub, G.M. Roglic, C. Pulgarin, J. Kiwi, *Colloids Surf. B Biointerfaces* 123 (2014) 593–599.

[255] P. Munnik, P. de Jongh, K. de Jong, *Chem. Rev.* 115 (2015) 6687–6718.

[256] S. Rtimi, *Catalysts* 7 (2017) 57.

[257] M. van Loosdrecht, J. Lyklema, W. Norde, G. Schraa, A. Zehnder, *Environ. Microbiol.* 53 (1987) 1893–1903.

[258] Y. An, R. Friedman, *J. Biomed. Mater. Res. Appl. Biomater.* 48 (1998) 338–348.

[259] A. Hogt, J. Dankert, J. Feijen, *J. General Microbiol.* 13 (1985) 2485–2489.

[260] A.J. Siddiqua, K. Chaudhury, B. Adhikari, *Res. Rev. J. Med. Org. Chem.* 1 (2015) 44–54.

[261] M. Fletcher, G.I. Loeb, *Appl. Environ. Microbiol.* 37 (1979) 67–72.

[262] J. Tsiboukis, M. Stone, A. Thorpe, P. Graham, V. Peters, R. Heerlien, J. Smith, K. Green, N. Nevel, *Biomaterials* 20 (1999) 1229–1235.

[263] E. Beril, B. Ufuk, K. Gurkan, *J. Photochem. Photobiol. A Chem.* 283 (2014) 29–37.

[264] T. Yuranova, R. Mosteo, J. Bandara, D. Laub, J. Kiwi, *J. Mol. Catal. A Chem.* 244 (2006) 160–167.

[265] M. Kamitakahara, S. Takahashi, T. Yokoi, V. Inoue, K. Ioku, *Mat. Sci. Eng. C* 61 (2016) 169–173.

[266] Y. Furuya, A. Dick, N. Perencevich, M. Pogorzelska, D. Goldmann, W. Stone, *PLoS One* (2011) 0015452.

[267] R. Batra, S. Cooper, C. Whiteley, K. Patel, D. Wyncoll, D. Edgeworth, *Clin. Infect. Dis.* 50 (2010) 210–217.

[268] E.A. Morell, D.M. Balikin, *J. Biol. Med.* 83 (2010) 223–233.

[269] R. McLean, A. Hussain, M. Sayer, P. Vincent, D. Hughes, T. Smith, *Can. J. Microbiol.* 39 (1993) 895–900.

[270] V. Slambarova, V. Zajicova, J. Karpiskova, P. Exnar, I. Stibor, *Mat. Sci. Eng. C* 33 (2013) 265–273.

[271] J. Ruparelia, A. Chatterjee, S. Duttagupta, S. Mukherji, *Acta Biomater.* 3 (2008) 707–716.

[272] G. Rao, K. Brastad, Q. Zhang, R. Robinson, Z. He, Y. Li, *Front. Environ. Sci. Eng. China* 10 (2016) 11–18.

[273] A.M. Eremenko, I.S. Petrik, N.P. Smirnova, A.V. Rudenko, Y.S. Marikvas, *Nanoscale Res. Lett.* 11 (2016) 28–38.

[274] J. Heffelfinger, J. Kool, S. Fridkin, V. Fraser, J. Hegeman, J. Carpenter, C. Whitney, *Infect. Control Hosp. Epidemiol.* 24 (2003) 569–575.

[275] J. Stout, V. Lu, *Infect. Control Hosp. Epidemiol.* 24 (2003) 563–568.

[276] H. Amir, M. Mucha, Xu Jie, *Adv. Mat. Res.* 31 (2014) 131–135.

[277] M. Paszkiewicz, A. Golabiewska, L. Rajkshi, E. Kowal, A. Sajdak, A. Zaleska-Medynska, J. Namomater, *(2016) ID 2187940.*

[278] M. Miranda-Rios, V. Luna Pabello, M. Orta de Velazquez, J. Barrera-Godinez, *Water SA* 37 (2011) 213–220.

[279] J. Hsieh, T. Yeh, C. Li, C. Chiu, C. Huang, *Vacuum* 87 (2013) 160–163.

[280] Ing. Baas, Berson UV-Technik, Amsterdam, NL, 2000.

[281] W. Harm, *Biological Effects of Ultraviolet Radiation*, Cambridge Univ. Press, Cambridge CB21RP, UK, 1980.

[282] A.J. Thornton, *J. Vacuum Sci. Technol. A* 1 (1974) 666–670.

[283] E. Belin-Ferré, *Surface Properties and Engineering of Complex Intermetallic v.3*, World Scientific, Singapore, Hackensack, N. J. USA, 2010.

[284] P. Docampo, S. Guldin, U. Steiner, H. Snaith, *J. Phys. Chem. Lett.* 4 (2013) 698–703.

[285] L. A., T.V. O'Halloran, *Science* 300 (2003) 931–936.

[286] E. Warren, C. Payne, *Cellular binding of nanoparticles disrupts the membrane potential*, *RSC Adv.* 5 (2015) 13660–13666.

[287] N. Kopidakis, R. Neale, K. Zhu, J. van de Lagemaat, J. Frank, A. J. Spatial Appl. Phys. Lett. 87 (2007) 202106.

[288] D. Adam, L. Brus, C. Chidsey, S. Creager, C. Creutz, Ch. Kagan, P.V. Kamat, M. Lieberman, S. Lindsay, M. Marcus, R. Metzger, M. Beyerle, J. Miller, M. Newton, D. Rolison, O. Sankey, K. Schance, J. Yardley, X. Zhu, *J. Phys. Chem. B* 107 (2003) 6668–6697.

[289] J. Pierson, D. Horwat, *Appl. Surf. Sci.* 53 (2007) 7522–7526.

[290] D. Munoz-Rojas, J. Fraxedas, P. Gomez-Romero, P. Casano, *J. Solid State Chem.* 178 (2005) 295–305.

[291] D. Munoz-Rojas, G. Subias, J. Fraxedas, P. Gomez-Romero, N. Casano-Pastor, *J. Phys. Chem. B* 109 (2005) 6193–6203.

[292] S. Rtimi, V. Nadtochenko, I. Khmel, J. Kiwi, *Chem. Comm.* 53 (2017) 9093–9096.

[293] S. Rtimi, V. Nadtochenko, I. Khmel, M. Bensimon, J. Kiwi, *Mater. Today Chem.* 6 (2017) 62–74.

[294] A. Pugsley, C. Schnaitmann, *J. Bacteriol.* 133 (1978) 1181–1189.

[295] X. Li, H. Nikaido, K. Williams, J. Bacteriol. 179 (1997) 6127–6133.

[296] T. Bechert, P. Steinrucke, J. Gugenbichler, *Nat. Med.* 6 (2000) 1053–1056.

[297] B. Allegranzi, S. Bagheri Nejad, C. Combesure, W. Graafmans, H. Attar, L. Donaldson, D. Pittet, *Lancet* 377 (2011) 228–241.

[298] T. Matsunaga, R. Tomoda, T. Nakajima, N. Nakamura, T. Komine, *Appl. Environ. Microbiol.* 54 (1998) 1330–1333.

[299] J.A. Rengifo-Herrera, A. Sienkiewicz, L. Forró, J. Kiwi, J.E. Moser, C. Pulgarin, *J. Phys. Chem. C* 114 (2010) 2717–2723.

[300] D. Naumann, C. Schultz, B. Sabich, M. Kasrowsky, J. Labishinski, *J. Molec. Struct.* 214 (1989) 213–246.

[301] D. Naumann, *Appl. Spectrosc. Revs.* 36 (2001) 239–298.

[302] C. Selle, W. Pohle, J. Fritsche, *J. Molec. Structure* 481 (1999) 402–405.

[303] P. Ganguly, C. Byrne, A. Breen, S.C. Pillai, *Appl. Catal. B* 225 (2018) 51–75.

[304] R. Wang, X. Kong, W. Zhang, W. Zhu, L. Huang, J. Wang, X. Zhang, X. Liu, Na Hu, Y. Suo, J. Wang, *Appl. Catal. B* 225 (2018) 228–237.

[305] X. Li, S. Fang, L. Ge, Ch. Han, P. Qiu, W. Liu, *Appl. Catal. B* 225 (2018) 62–69.

[306] S. Azzizi, R. Mohamad, R. Rahim, A. Maghadam, M. Moniri, A. Ariff, W. Zaad, *Appl. Surf. Sci.* 384 (2016) 517–524.

[307] S. Tallosy, L. Janovak, E. Nagy, A. Deak, A. Juhasz, E. Csapo, N. Buzas, I. Dekany, *Appl. Surf. Sci.* 371 (2016) 139–150.

[308] D. Wojcieszak, M. Mazur, D. Kaczmarek, B. Szponar, M. Grobelny, M. Kalisz, A. Pelczarska, I. Szczyciel, A. Poniedzialek, M. Osekowska, *Appl. Surf. Sci.* 380 (2016) 159–164.

[309] R. Michal, E. Dworniczek, M. Caplovicova, O. Montfort, P. Lianos, L. Caplovic, G. Plesh, *Appl. Surf. Sci.* 371 (2016) 538–546.



Dr. Sami Rtimi is a photo-chemist with a strong background in surfaces engineering and microbiology. He was awarded a Ph.D. in Chemistry and Chemical Engineering from Swiss Federal Institute of Technology (EPFL, Switzerland) and a Doctorate in Biological Sciences from the University of Carthage (Tunisia). His expertise relates to the design, synthesis, evaluation and surface property characterization of antibacterial films for medical device applications. His current research addresses coupling nanostructures for a targeted biological response at the solid-air and solid-water interfaces showing potential practical applications. He published several papers in high impact journals in the field, numerous book chapters, patents and presented in several national and international conferences. He is editor in some journals (Euro-Mediterranean Journal for Environmental Integration, Earth Systems and Environment...), edited some special issues (Applied Catalysis B: Environmental, MDPI-Coatings, Colloids and Surfaces B: Biointerfaces) and books (Nanomaterials Based Coatings: Fundamentals and Applications, Elsevier 2018). He is member of many national (Swiss Chemical Society) and international societies/associations (ACS, RSC, EPS, IAAM). He is Advisory Panel for Elsevier since 2014.



Dr. Dionysios (Dion) D. Dionysiou is currently a Professor of Environmental Engineering and Science Program at the University of Cincinnati. He teaches courses and performs research in the areas of drinking water quality and treatment, advanced oxidation technologies and nanotechnologies, and physical-chemical processes for water quality control. He is currently one of the editors of Chemical Engineering Journal, Editor-in-Chief of the Journal of Advanced Oxidation Technologies, Editor-in-Chief of the Journal of Environmental Engineering (ASCE), and member of the Editorial Boards of several other journals. Dr. Dionysiou is the author or co-author of 360 refereed journal publications, 86 conference proceedings, 32 book chapter publications, 26 editorials, and 600 presentations. He has edited/co-edited 6 books on water quality, water reuse, ferrate/ferrite technologies, and photocatalysis. He is currently co-editing a book on harmful algal blooms. Dr. Dionysiou's work received over 20,000 citations with an H factor of 74.



Dr. Suresh C. Pillai obtained his PhD in the area of Nanotechnology from Trinity College Dublin and then performed a postdoctoral research at California Institute of Technology (Caltech), USA. Upon completion of this appointment he returned to Trinity College Dublin as a Research Fellow before joining CREST-DIT as a Senior Research Scientist in April 2004. He has also completed an executive MBA from Dublin City University, in 2009. Suresh joined in IT Sligo as a Senior Lecturer in Environmental Nanotechnology in October 2013. He is an elected fellow of the UK's Royal Microscopical Society (FRMS) and the Institute of Materials, Minerals and Mining (FIMMM). Suresh was responsible for acquiring more than €4 million direct R&D funding. His research work was featured in various international media such as BBC, RTE-1 TV, Ocean FM radio, Al Jazeera TV and in a number of national and international print media (Times UK, The Guardian, Irish Times etc). He has published several scientific articles in leading peer reviewed journals and has presented in several international conferences. He has delivered over fifty international invited talks including several key-note and plenary talks. He was also the recipient of the 'Hothouse Commercialisation Award 2009' from the Minister of Science, Technology and Innovation and the recipient of the 'Enterprise Ireland Research Commercialization Award 2009'. He is an editor for the journal Environmental Science and Pollution Research (ESPR, Springer) and Editorial Board Member for the Chemical Engineering Journal and Applied Catalysis B (Elsevier).



Dr. John Kiwi: John Kiwi was born in 1940 in Santiago, Chile. He received his PhD from the Oregon State University, Corvallis, OR, USA in the special field of Radiation and Photochemistry in 1971. He joined Notre Dame Radiation Laboratory (Notre Dame, Indiana) as research associate. As guest scientist, he worked in the Hahn-Meitner-Institute for Nuclear Chemistry (Berlin, Germany). In 1982, he moved to join the group of Prof. George Porter (Nobel Prize 1967) at the Royal Institution in London, UK. His work focused on light enhanced heterogeneous catalysis. In 1987, he was invited as a guest scientist at the Department of Chemistry at Hebrew University. In 1992, he was appointed as Private-Dozent (Lecturer) at the Department of Chemistry at the Swiss Federal Institute of Technology (EPFL, Switzerland) and assigned to lead the course of Physical Chemistry of the Environment. During his career, he has published more than 300 papers (H index 66). He has carried out pioneering work in redox catalysis since early 1980s, in the area of heterogeneous catalysis for environmental remediation addressing conventional colloidal, electrochemical and plasma-assisted preparation of catalysts/photocatalysts.